UNIVERSITY OF MESSINA

DEPARTMENT OF ENGINEERING

DOCTORAL PROGRAM IN

"CHEMISTRY AND ENGINEERING OF MATERIALS AND CONSTRUCTIONS"

DEVELOPMENT OF CATALYTIC ELECTRODES AND CELL DESIGN FOR SOLAR FUEL GENERATION

Doctoral Dissertation of:

Francesco Tavella

Supervisor:

Prof. Claudio Ampelli

The Chair of the Doctoral Program:

Prof. Giovanni Neri

2017/2018 – XXXI Cycle

UNIVERSITÀ DEGLI STUDI DI MESSINA

DIPARTIMENTO DI INGEGNERIA

CORSO DI DOTTORATO IN:

"CHIMICA E INGEGNERIA DEI MATERIALI E DELLE COSTRUZIONI"

SVILUPPO DI MATERIALI ELETTRODICI PER LA PRODUZIONE DI COMBUSTIBILI SOLARI

Tesi di dottorato di:

Francesco Tavella

Tutor:

Prof. Claudio Ampelli

Coordinatore del corso di dottorato:

Prof. Giovanni Neri

2017/2018 – XXXI Ciclo

Contents

Abstract (English)

The possibility of exploiting solar energy for the direct production of fuels and chemicals (e.g. hydrogen, hydrocarbons, alcohols) represents a future challenge to move towards a new green economy, recently defined as “solar-driven chemistry”.

In this view, this PhD thesis focuses on the development of a new approach to convert solar energy, through the synthesis of innovative photoactive materials/electrodes for the production of solar fuels. By assembling these photo-electrodes in a photo-electrochemical (PEC) cell, designed on purpose to mimic what nature does with the leaves, solar energy can be captured and used to produce hydrogen from water (by water photo-electrolysis) or to generate value-added carbon products (by reducing atmospheric CO_2) in a one-step process, like an “artificial leaf”. Thus, the main objective of the present PhD work was to develop photocatalytic thin films able to work as photoanodes in efficient PEC devices, especially for the production of hydrogen.

The PhD activities were carried out at the laboratory CASPE/INSTM (Laboratory of Catalysis for Sustainable Production and Energy) of the University of Messina. During the three years of activity, all the aspects concerning the performances of the photocatalysts and the related PEC electrodes and cell, have been carefully evaluated.

Initially, the research activity focused on the preparation of titania (TiO_2) nanotubes synthesized by controlled anodic oxidation technique. The peculiarity of this method is the possibility to “tailor” the morphology and the nanostructure of the catalyst by modulating some parameters during the synthesis (such as the electrolyte composition, the pH, the applied voltage, the anodization time). In general, the use of titanium dioxide as a photocatalyst, despite many advantages (low cost, non-toxicity, resistance to photo-corrosion, high quantum yield), has two main drawbacks: i) the low absorption of light in the visible region, due to the high band gap (in the range of 3.0-3.2 eV) and ii) the fast charge recombination, which usually occurs at the grain boundaries of the particles. The latter can be mitigated by the realization of nanostructures such as nanotubes or nanorods, which may improve the vectorial transport of electrons to the collector layer.

Different characterization techniques (SEM-EDX, TEM, XRD, UV-vis Diffuse Reflectance Spectroscopy) were used to investigate the properties of the as-prepared TiO_2 nanotube arrays, as well as to evaluate their electrochemical behaviour (Cyclic voltammetry, Chrono-amperometry). Part of the characterization by electron microscopy was carried out in collaboration with the Department of Chemical Sciences of the University of Padua. The main aim was to obtain a correlation between synthesis parameters, nanostructure properties and photo-catalytic performances.

Moreover, particular attention was given to the evaluation of the efficiency of the PEC cell. To pursue this aim, titania nanotubes of different lengths (from 0.5 to 6 μm) were synthesized by varying the anodization time from 30 min to 5 h. A monochromator and a spectroradiometer were used to evaluate the light irradiance at different wavelengths directly inside the PEC device. These measurements allowed for the calculation of different kinds of efficiencies: i) the photoconversion efficiency, also called solar-to-hydrogen efficiency (STH), which takes into account the amount of energy supplied in terms of light and the products obtained (i.e. hydrogen); ii) the Faradaic efficiency (η), which relates the photo-generated current to the produced hydrogen; iii) the quantum efficiency, expressed as IPCE (incident photon to current efficiency) and APCE (absorbed photon to current efficiency). The most important results (reported in detail in Chapter 3) showed that, for use in a PEC cell, the 45-min-anodized nanotube arrays (tube length of about 1 μm) provided the best performance, with a H_2 production of 22.4 μmol h^{-1} cm^{-2} and a STH efficiency as high as 2.5%. These values are among the best ever reported insofar as undoped TiO_2 photoanodes are used and in absence of external bias or sacrificial agents. The final part of Chapter 3 was dedicated to the preparation of 3D-type meso/macro porous structured photoanodes based on Ti mesh, working as a hierarchical structure (consisting of Ti mesh macropores and TiO_2 nanotube mesopores) to improve the mass and charge transport within the PEC cell.

In order to improve the light absorption in the visible region, it is necessary to dope the nanostructured TiO_2 materials with heteroatoms or decorate their surface with metal nanoparticles. In this direction, nanoparticles of gold (Au) were deposited on the surface of TiO_2 nanotubes by optimizing three different techniques (wet impregnation, photo-reduction and electrodeposition) and their performances were studied by using a gas photo-reactor (GP)

and a photo-electrochemical (PEC) cell, both homemade. Furthermore, with the aim of exploiting earth-abundant and low-cost materials, photocatalysts based on Cu-doped TiO_2 nanotubes were also synthesized and successfully tested in the PEC cell for H_2 production in water-photo-electrolysis and ethanol photo-reforming. This part of the work was carried out in collaboration with the Institute of Chemistry in Araraquara (Brazil). The CuO nanoparticles were deposited by adopting two different techniques, dip-coating and electrodeposition. The results (reported in detail in Chapter 4) showed that the presence of small metal (Au and Cu) nanoparticles strongly increased H_2 production rate in a gas photo-reactor, with a maximum of about 190 μmol in 5 h of light irradiation obtained for Au-doped TiO_2 nanotubes prepared by electrodeposition. However, in the PEC cell (with oxidation/reduction half reactions separated in two different chambers of the cell) it was observed that the presence of metal nanoparticles on TiO_2 surface at the photo-anode can create a counter-circuited current, diminishing the H_2 production at the cathode side. However, this phenomenon was successfully minimized by preparing very small CuO nanoparticles (lower than 2 nm) decorating the internal walls of the TiO_2 nanotubes by controlled dip-coating technique.

Finally, nanostructured tantalum oxynitride (Ta-oxy-N) electrodes were synthesized through controlled anodic oxidation technique, by adapting the synthesis conditions previously optimized for TiO_2. The advantages of these tantalum-based materials refer to their lower band-gap (1.9-2.5 eV) with respect to titania (3.0-3.2 eV), thus improving light absorption in the visible region. After the anodization, a high temperature nitridation process (600-900 °C) was needed to replace partially oxygen with nitrogen in the Ta_2O_5 lattice. The results (reported in detail in Chapter 5) allowed to obtain a clear correlation between the parameters using during the synthesis (i.e. applied voltage, anodization time) and the Ta-oxy-N nanostructures (nanotube diameter and length, wall thickness and grade of voids). The best photocurrent response was obtained for the Ta-oxy-N sample anodized at 40 V for 1 min and then thermally treated with ammonia at 800°C. However, further investigation is needed to improve the mechanical resistance of these photo-catalysts.

Abstract (Italian)

La possibilità di sfruttare l'energia solare per la produzione diretta di combustibili e prodotti chimici (quali idrogeno, idrocarburi ed alcoli) rappresenta la sfida del prossimo futuro per muoversi verso una nuova economia verde, recentemente definita come "solar-driven chemistry".

In quest'ottica, la tesi di dottorato si concentra sullo sviluppo di un nuovo approccio per convertire l'energia solare, attraverso la sintesi di materiali ed elettrodi innovativi fotoattivi per la produzione di combustibili solari. Assemblando questi foto-elettrodi in una cella fotoelettrochimica (PEC), progettata apposta per imitare ciò che la natura fa con le foglie, l'energia solare può essere catturata e utilizzata per produrre idrogeno dall'acqua (mediante foto-elettrolisi) o per generare composti a base di carbonio ad alto valore aggiunto (attraverso la riduzione della CO_2 atmosferica) in un processo a singolo stadio del tutto simile ad una "foglia artificiale". Pertanto, l'obiettivo principale del presente lavoro di dottorato è stato quello di sviluppare film sottili fotocatalitici in grado di funzionare come fotoanodi in dispositivi PEC, ed in particolare per la produzione di idrogeno.

Le attività di dottorato sono state svolte presso il laboratorio CASPE/INSTM (Laboratory of Catalysis for Sustainable Production and Energy) dell'Università di Messina. Durante i tre anni di attività, sono stati attentamente valutati tutti gli aspetti riguardanti le prestazioni dei fotocatalizzatori, dei relativi elettrodi nonché delle celle PEC.

Inizialmente, l'attività di ricerca si è concentrata sulla preparazione di nanotubi di titanio (TiO_2) sintetizzati mediante la tecnica dell'ossidazione anodica controllata. La particolarità di questo metodo risiede nella possibilità di "personalizzare" la morfologia e la nanostruttura del catalizzatore modulando alcuni parametri durante la sintesi (come la composizione dell'elettrolita, il pH, la tensione applicata, il tempo di anodizzazione). In generale, l'uso del biossido di titanio come fotocatalizzatore, nonostante i suoi numerosi vantaggi (basso costo, non tossicità, resistenza alla foto-corrosione, elevata resa quantica) presenta due principali inconvenienti: i) il basso assorbimento di luce nella regione visibile, a causa dell'elevato band-gap (compreso tra 3.0 e 3.2 eV) e ii) l'elevata ricombinazione di carica, che di solito si verifica ai bordi dei grani delle particelle. Quest'ultima può essere mitigata con la realizzazione di

nanostrutture come nanotubi o nanorod, che possono migliorare il trasporto vettoriale degli elettroni verso lo strato collettore di Ti.

Diverse tecniche di caratterizzazione (SEM-EDX, TEM, XRD, Spettroscopia a Riflettanza Diffusa UV-visibile) sono state utilizzate per studiare le proprietà dei nanotubi di TiO_2 sintetizzati, mentre per valutare il loro comportamento elettrochimico sono state effettuate delle misurazioni di voltammetria ciclica e crono-amperometria. Parte della caratterizzazione mediante microscopia elettronica è stata effettuata in collaborazione con il Dipartimento di Scienze Chimiche dell'Università di Padova. L'obiettivo principale è stato quello di ottenere una correlazione tra parametri di sintesi, proprietà della nanostruttura e prestazioni fotocatalitiche.

Inoltre, è stata prestata particolare attenzione alla valutazione dell'efficienza della cella PEC. Per raggiungere questo scopo, sono stati sintetizzati nanotubi di titania di diverse lunghezze (da 0,5 a 6 μm) variando il tempo di anodizzazione da 30 minuti a 5 ore. Un monocromatore e uno spettroradiometro sono stati usati per valutare l'irradianza della luce a diverse lunghezze d'onda direttamente all'interno del dispositivo PEC. Queste misurazioni hanno consentito il calcolo di diversi tipi di efficienza: i) l'efficienza di fotoconversione, detta anche efficienza solare a idrogeno (STH), che tiene conto della quantità di energia fornita in termini di luce e prodotti ottenuti (cioè idrogeno); ii) l'efficienza Faradica (η), che collega la corrente generata direttamente all'idrogeno prodotto; iii) l'efficienza quantica, espressa come IPCE (incident photon to current efficiency) e APCE (absorbed photon to current efficiency). I risultati più importanti (riportati in dettaglio nel Capitolo 3) hanno mostrato che, per l'utilizzo in una cella PEC, i nanotubi di TiO_2 preparati con un tempo di anodizzazione di 45 min (lunghezza del tubo di circa 1 μm) forniscono le migliori prestazioni, con una produzione di H_2 di 22,4 μmol h^{-1} cm^{-2} e un'efficienza STH del 2,5%. Questi valori sono tra i migliori mai riportati per una cella PEC in cui viene utilizzato TiO_2 non drogato ed in assenza di potenziale esterno e/o agenti sacrificali. La parte finale del capitolo 3 è stata dedicata alla preparazione di fotoanodi meso/macro strutturati (3D-type) basati su reti di Ti, che funzionano come una struttura gerarchica (costituita dai macropori della rete di Ti e dai mesopori dei nanotubi di TiO_2) per migliorare il trasporto di massa all'interno della cella PEC.

Per migliorare l'assorbimento della luce nella regione visibile, è necessario drogare i materiali nanostrutturati di TiO_2 con eteroatomi oppure decorare la loro superficie con nanoparticelle metalliche. Con questo intento, sulla superficie dei nanotubi di TiO_2 sono state depositate nanoparticelle d'oro (Au) ottimizzando tre diverse tecniche di deposizione (impregnazione ad umido, foto-riduzione ed elettrodeposizione) e le loro prestazioni sono state studiate utilizzando un reattore in fase gas (GP) e una cella fotoelettrochimica (PEC). Inoltre, allo scopo di limitare al massimo l'utilizzo di metalli nobili, sono stati realizzati dei fotocatalizzatori basati su nanotubi di TiO_2 drogati con Cu, testati poi con successo nella cella PEC per la produzione di H_2 nei processi di foto-elettrolisi dell'acqua e foto-reforming dell'etanolo. Questa parte del lavoro è stata svolta in collaborazione con l'Istituto di Chimica di Araraquara (Brasile). Le nanoparticelle di CuO sono state depositate adottando due diverse tecniche, il dip-coating e l'elettrodeposizione. I risultati (riportati in dettaglio nel capitolo 4) hanno dimostrato come la presenza di nanoparticelle di metallo (Au e Cu) aumenti notevolmente la velocità di produzione di H_2 nel foto-reattore in fase gas, con un massimo di circa 190 µmol in 5 ore di irradiazione per i campioni di TiO_2 drogati con Au preparati per elettrodeposizione. Tuttavia, nella cella PEC (in cui le semi-reazioni di ossidazione e riduzione avvengono in due ambienti separati) è stato osservato che la presenza di nanoparticelle metalliche sulla superficie di TiO_2 diminuisce la produzione di idrogeno al catodo, poiché le particelle metalliche agiscono da centri di riduzione direttamente nel comparto anodico con conseguente corto-circuito della corrente elettrica. Tuttavia, si è cercato di risolvere tale problematica preparando mediante la tecnica del dip-coating delle nanoparticelle di CuO molto piccole (inferiori a 2 nm) localizzate preferenzialmente all'interno dei nanotubi di TiO_2.

Infine, sono stati sintetizzati degli elettrodi nanostrutturati a base di ossido di tantalio (Ta-oxy-N) mediante la tecnica di ossidazione anodica controllata, adattando le condizioni di sintesi precedentemente ottimizzate per il TiO_2. I vantaggi di questi materiali a base di tantalio sono legati al loro band-gap (1,9-2,5 eV) inferiore rispetto alla titania (3,0-3,2 eV), migliorando così l'assorbimento della luce nella regione visibile. Dopo l'anodizzazione, è stato necessario un trattamento con ammoniaca ad alta temperatura (600-900 °C) per sostituire parzialmente l'ossigeno con l'azoto nel reticolo del Ta_2O_5. I risultati (riportati in dettaglio nel capitolo 5) hanno permesso di ricavare una chiara correlazione tra i parametri utilizzati durante la sintesi

(cioè voltaggio applicato e tempo di anodizzazione) e le nanostruttura di Ta-oxy-N (diametro e lunghezza dei nanotubi, spessore della parete e grado di vuoto). La risposta migliore in termini di fotocorrente è stata ottenuta per il campione di Ta-oxy-N anodizzato a 40 V per 1 minuto e successivamente trattato termicamente con ammoniaca a 800 °C. Tuttavia, sono necessarie ulteriori indagini per migliorare la resistenza meccanica di questi catalizzatori.

1 Introduction

1.1 Energy consumption overview

In the last decade, the global primary energy consumption has grown at an average rate of 1.7% per year, despite the greatest world economic crisis since World War II. Particularly, primary energy consumption grew strongly in 2017 (by 2.2%), up from 1.2% last year and it is the fastest growth since 2013. All fuels, except coal and hydroelectricity, grew at above-average rates. Natural gas accounted for the largest increment in energy consumption at 83 million tonnes of oil equivalent (Mtoe), followed by renewable energy (69 Mtoe), which grew fast driven by robust growth in both wind and solar power, and finally oil (65 Mtoe) [1]. Oil and coal continues to represent the first energy source (Figure. 1.1), the largest majority of which (ca. 80%) is used to power the world transportation system, the remainder being used for heat and electricity, petrochemicals, asphalt and lubricants, in order of decreasing importance [1-2]. The most relevant change in the world energy landscape is the rise of renewable energies, primarily in the electricity sector. In 2014, for the first time, global carbon emissions associated with energy production remained stable despite continued economic growth. This can be attributable to the increasing penetration of renewable enhanced energy efficiency, particularly in the affluent world. The key player in this changing scenario is China, which now produces as much electricity from water, wind, and sunlight, as all France and Germany's power plants combined [3]. The almost 7-fold drop of the photo-voltaic (PV) module price in the last decade has been the consequence of the 10-fold increase of the Chinese production; this has made PV a truly game changer in the global energy market. The number of countries where PV electricity is competitive with conventional technologies (e.g., coal or nuclear) is constantly increasing and its contribute of electricity production in some industrialized countries has become remarkable. In 2014, Italy produced almost 8% of its consumption by PV, now the largest share in the world [4]. All the renewable energy sectors continue to grow, the estimated renewable share of final energy consumption is about 19.3%, modern technologies and traditional biomass being at 10.2 and 9.1% respectively. By far, the most important renewable sector is electricity production, with 22.8% of the overall world's generation. At the end of

2016, hydroelectric global capacity exceeded 1 TW, wind was 370 GW, and PV almost 180 GW; they covered 19.3, 3.1 and 0.9 %, respectively, of the world electricity demand. The above selected data suggest that the energy transition from fossil fuels to renewables is already ongoing [5].

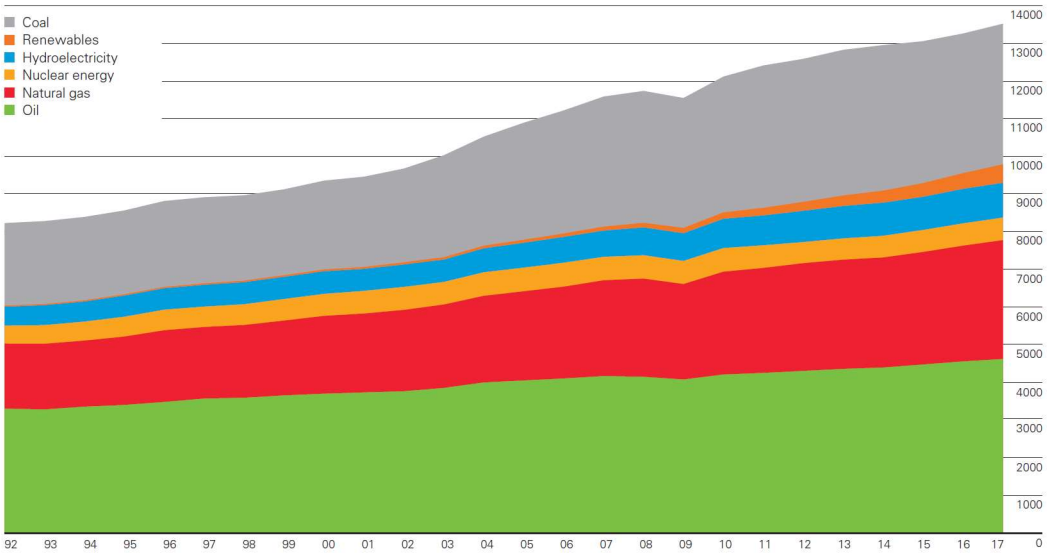

Figure 1.1: World energy consumption overview [BP Statistical Review of World Energy 2018].

1.2 Sunlight

Energy represents the most important resource for humanity and sunlight is our primary energy source. Sunlight is abundant (90 PW received on the earth's surface), inexhaustible (the sun will last for more than 4 billion years), and fairly well distributed over the planet [6]. A very small fraction of solar energy, about 0.1% is converted and stored in terrestrial biomass by natural photosynthesis [7].

Solar energy, is not useful unless it is converted into heat, electricity, and fuels the final usable energy forms for mankind. Conversion of solar energy into heat is clear, but conversion of solar energy into electricity and fuels, the noblest energy forms, poses several problems [8].

First of all, conversion of sunlight into electricity and fuels can only be done by processes that limit the conversion efficiency. Since the solar spectrum cannot be modified, materials

capable of exploiting sunlight and converting efficiently photons in energy should be developed.

Taking into account the average spectral distribution of solar energy, the most favourable threshold is about 885 nm (1.4 eV), which in principle allows 33% energy conversion efficiency [9]. The materials suitable to be used for solar energy conversion should be: 1) cheap; 2) earth abundant, 3) low costly 4) with low environmental impact and 5) stable under prolonged exposure to sunlight irradiation. Solar energy unfortunately suffers by intermittency and intensity fluctuations due the atmospheric conditions and day/night cycles. For these reasons, the use of solar energy into electricity requires storage components to be integrated in the entire system. It is necessary to choose the best storage option to be compatible with the amount of energy stored [8].

Sunlight is dilute: the average solar power lighting the earth's surface annually is about 170 W m^{-2}. Only a small part of this power can be converted into fuel or electricity. Solar renewable energies have average annual power densities ranging between 5–20 W m^{-2} (photovoltaic panels) and <1 W m^{-2} (biomass). Power densities of final energy uses in modern societies range between 10 and 70 W m^{-2} for houses and low-energy intensity manufacturing buildings. Supermarkets and office buildings use 20–100 W m^{-2}, energy intensive industrial activities such as steel mills and refineries require 300–900 W/m^2, whereas high-rise buildings may need up to a few thousands W m^{-2} [10]. By considering these values, it is certainly possible to power a house with the amount of sunlight intercepted by its roof, but this will never be possible for an oil refinery or a skyscraper.

1.3 Energy Return of Investment (EROI)

EROI (energy return on investment) is an important parameter to quantify energy costs. This index takes in account the quantity of gained energy divided by the energy required to get that energy (Equation 1.1) [11].

$$\text{EROI= energy gained/energy required to get that energy} = E_{out}/E_{in} \quad (1.1)$$

If the EROI is equal to or less than one, the energy is dissipated and its value as a primary energy source becomes not convenient. The calculation of EROI is extremely complex, because it involves the aggregation of different energy investments, which so far has made it difficult to formulate a universally accepted calculation methodology, but it is a useful parameter to compare the same energy sources [11].

In the case of oil, the EROI can be estimated from the ratio between the number of barrels extracted divided by the number of barrels consumed to carry out the extraction process. The EROI declined over time, as the availability of primary energy sources decreases with the depletion of the reservoir.

On the contrary, in the case of renewable energy the EROI increases over time due to technological improvements. For solar energy, EROI refers to the energy produced and invested in the conversion device (photovoltaic modules) [12]. The EROI, as defined by equation (1) is a good parameter for estimating the "energy balance point" of a fuel, for example, if there is a net gain or energy loss at the farm gate to produce ethanol from corn.

The energy of human labour as well as the quality of energy obtained with reference to its specific use and the energy needed to compensate for environmental impacts should be included for a more precise assessment of an energy source [13]. As discussed above, the average EROI of fossil fuels is decreasing due to the depletion of the deposits. For example, the EROI for oil in the United States declined from about 20 in 1970 to about 11 in 2013. In the same year, the EROI of oil production from ultra-deep areas was less than 10, while the EROI for the shale oil was estimated around 1.5 [14].

A concept related to EROI is that of “net energy”, defined as the difference between the energy acquired from a given source (gross energy, E_{out}) and the energy used to obtain and supply that energy (E_{in}), measured during the entire life cycle (Equation 1.2). Equation 1.1 allows us to express the net energy as a function of EROI (Equation. 1.3).

$$\text{net energy} = Eout - Ein \tag{1.2}$$

$$\text{net energy} = Eout\,(1-1/EROI) \tag{1.3}$$

From Equation (3) it can be seen that the relationship between net delivered energy and decreasing EROI is not linear. The net delivered energy, in the other hand, decrease as EROI

decreases. For example, 1 L of a fuel with an EROI of 100 delivers 99% of that fuel to society, whereas 1 L of a fuel with an EROI of 2 delivers only 50% [15].

EROI should be one of the most important factors in determining the quality of life of any government. If the EROI declines, the net energy provided to society declines and, at some point, the amount of net energy will be insufficient to meet the existing demand. The EROI that provides just enough net energy to support all current energy needs represents the minimum EROI for a sustainable society, a value that is different for different societies [13].

1.4 Solar Fuels

The possibility to produce fuels or chemicals from water and CO_2 by using solar energy directly (by using a PEC device) or indirectly (with the electrical energy produced from photovoltaic) represents the challenge of the new century [16].

Production of solar fuels includes in his concept all the renewable energy sources (RE), and thus is not limited to the direct use of solar radiation. In the last decades, most studies have focused on the production of H_2 by water splitting, but a growing interest concerns the conversion of CO_2. RE suffers the problem related to fluctuations in the production and long-range transport of electrical energy, while the production of solar fuels, allowing the storage and distribution of RE, may be the key element to switch from a centralized energy production model to a new energy model based on distributed energy production and storage [17].

In nature, the classic example of solar fuels production is given by chlorophyll photosynthesis, which converts light into chemical energy that can later be released as "fuel for life activities". The time taken by plants to produce fuel is not sufficient to satisfy the energetic demand of human activities, so the need arises to develop artificial systems (artificial leaves, (see paragraph 1.7) that imitate the process of photosynthesis but at the same time satisfy the chemical industry's requirements. An artificial leaf must guarantee a continuous production (under sunlight) and possess a solid and resistant structure. In the next paragraphs both natural and artificial photosynthesis will be described.

1.5 Natural Photosynthesis

The photosynthesis is the process responsible for life on earth, using sunlight to convert CO_2 and H_2O into carbohydrates (sugar). The process of photosynthesis is initiated by the capture of sunlight by a network of light-absorbing molecules (chromophores), which are also responsible for the subsequent funnelling of the excitation energy to the reaction centres. Through evolution, genetic drift, and speciation, photosynthetic organisms have discovered many solutions for light harvesting. There are a large variety of different types of light-harvesting complexes found in nature [18]. Different light-harvesting complexes have evolved to allow efficient absorption of the wavelengths of the solar spectrum that are available to photosynthetic species in any particular ecological sector. Higher plants, that are exposed to the full solar spectrum available at the surface of the earth, possess chlorophyll as the main light-harvesting pigment. The structures of the different types of light-harvesting pigment protein complexes reflect the necessary structural requirements to collect the different types of wavelength. These polypeptides collocate perfectly the pigments with respect to the distances between them and the relative orientation of the transitions dipole moments of the pigments' excited states that are involved in the energy transfer reactions [19]. The three stages of photosynthesis take place in the presence of light: (1) light harvesting from sunlight; (2) use of that energy for the production of ATP and reducing power, reduced ferredoxin, and NADPH; and (3) capture and conversion of CO_2 into carbohydrates and other cell constituents [20]. During the third stage, namely, the carbon reactions, long incorrectly designated as the "light independent reactions", the energy-rich products of the light reactions are used to reduce CO_2. The heart of the photosynthetic process is the splitting of water by sunlight into oxygen and hydrogen. The oxygen is released into the atmosphere where it is available for living beings to breathe and for burning fuels. The hydrogen is combined with carbon dioxide to make sugars and other organic molecules of various types. When fuels burn (fossil, biomass and other biofuels) the hydrogen stored in these organic molecules combines with oxygen, completing a cycle started millions of years ago. From the energetic point of view, the synthesis of organic molecules represents a way of storing hydrogen and therefore storing solar energy in the form of chemical bonds (figure. 1.2) [21].

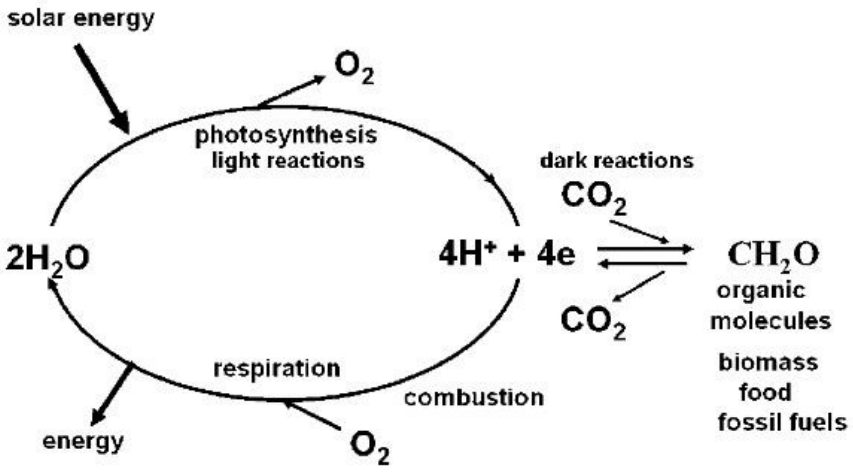

Figure 1.2: Simplified photosynthesis cycle reproduced with permission from ref. [21].

Figure 1.3 shows a simplified Z-scheme of the light reactions of photosynthesis [22]. For every electron extracted from water and transferred to CO_2, the energy of two photons of light is required. One is absorbed by Photosystem II (PSII), which generates a strong oxidising species (P680+), able to drive the water splitting reaction and a reduction of pheophytin (Pheo) and then plastoquinol (Q) to plastoquinol (QH2). The other, Photosystem I (PSI), generates a strong reducing species, NADPH, which donates reducing equivalents to CO_2 to produce sugars and other organic molecules, and a weak oxidant P700+. Electron and proton flow from QH2 to P700+ is aided by the cytochrome b6f (Cyt b6f) complex and plastocyanin (PC) and results in the release of energy to convert ADP to ATP. The ATP produced is required, along with NADPH, to convert CO_2 to sugars. Since the production of O_2 requires the splitting of two water molecules, the overall process involves the removal of two electrons per water and therefore four photons per PSII and PSI reaction centre. The reduction of oxidised nicotinamide adenine dinucleotide phosphate (NADP+) by PSI is facilitated by membrane bound iron sulphur proteins (Fx, FA and FB) and soluble ferredoxin (FD).

Quantum yield efficiency of the plants is very low (below 1%) and only some microalgae achieve slightly better efficiencies [23]. Improving light harvesting and conversion processes, and modifying the process to produce directly the target solar fuels, are the two main aspects to move to the realization of the artificial leaves, but which need to be sufficient simple and robust to be competitive with plants.

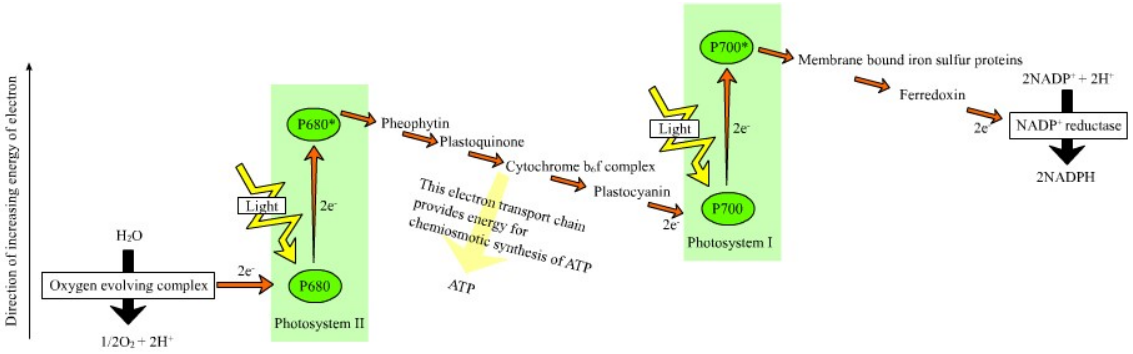

Figure 1.3: Simplified Z-scheme of the light reaction of photosynthesis.

1.6 Artificial Photosynthesis

The most important photochemical processes are the splitting of water to oxygen and hydrogen. Photosynthesis produces the energy that sustains life on our planet by using solar light to rearrange the bonds of water to oxygen and hydrogen; the hydrogen is fixed by its combination with carbon dioxide to produce carbohydrate. Analysis of the energetics of the solar fuels conversion process shows that it is water splitting and not carbohydrate production that is at the heart of solar energy storage [21]. The possibility to achieve the production of fuels by artificial photochemical reactions were first predicted by the Italian chemist Giacomo Ciamician over one century ago [24]. The studies on artificial photosynthesis are currently concentrated on using sunlight to reduce carbon dioxide in aqueous solution to carbon monoxide, ethanol, or methane (equation 1.4) [25] or to split water into molecular hydrogen and molecular oxygen (equation 1.5). Since carbon dioxide reduction is more difficult than water splitting from a kinetic point of view and can also be performed by a thermal reaction with molecular hydrogen to yield methanol [26], the attention of most scientists is focused on the water splitting (WS) reaction (equation 1.5):

$$CO_2 + 2\,H_2O + 8\,h\nu \rightarrow CH_4 + 2\,O_2 \quad \Delta G^0 = 8.30\ eV \tag{1.4}$$

$$2\,H_2O + 4\,h\nu \rightarrow 2\,H_2 + O_2 2 \quad \Delta G^0 = 4.92\ eV \tag{1.5}$$

From the thermodynamic point of view, the most convenient water-splitting process concerns the evolution of molecular oxygen and molecular hydrogen from liquid water

(Equation 1.6), the low-energy thermodynamic barrier (1.23 eV) of which allows, in principle, conversion of about 30% of the solar energy. Water splitting entails two multi-electron-transfer reactions (Equations 1.7 and 1.8).

$$2\ H_2O \rightarrow 2H_2 + O_2 \qquad \Delta G^0 = 1.23\ eV \tag{1.6}$$

$$2\ H_2O + 2e^- \rightarrow H_2 + 2\ OH^- \qquad E^0\ (pH\ 7) = -0.41\ V\ vs\ NHE \tag{1.7}$$

$$2\ H_2O \rightarrow O_2 + 4H^+ + 4e^- \qquad E^0\ (pH\ 7) = +0.82\ V\ vs\ NHE \tag{1.8}$$

Given that in a photochemical process each photon can transfer only one electron, [27] in a water-splitting system two catalysts must be present: one to collect electrons for the production of molecular hydrogen, the other one to collect holes (positive charges) for the generation of molecular oxygen [28]. The design of efficient, cost-effective artificial systems requires to maintain the main elements in the leaf-like hierarchical structures of natural leaves, but developing new functional elements inspired from the key steps of natural photosynthesis. An artificial leaf should be composed of the following main elements:

a) an *anode,* exposed to sunlight carrying a photocatalyst able to oxidize water, and supported on a conductive substrate which allows the fast collection of the electrons, but at the same time is permeable to protons, in order to transport the electrons and protons to the cathode side. An alternative approach is to prepare 2D photonic materials adsorbing in the visible and use sensitizers for a two-photon transfer process of energy to the semiconductor

b) a *membrane* enabling fast transport of protons (possibly also electrons, but which preferably have to be transported externally through a wire or through physically separated elements of the membrane to avoid their recombination). Possibilities are carbon nanotubes or TiO_2 connecting the two electrodes and ion-exchange resins, like Nafion® or other proton-conducting polymeric membranes. The membrane should be tailored to provide the minimum transfer resistance to protons and have also a minimum thickness (in principle some microns), but also at the same time block oxygen permeation to preserve hydrogen synthesis activity at the cathode. The membrane should be also in good contact with the anode and cathode sites and it is necessary to minimize the resistances at the interface [29].

c) a *cathode*, formed by a conductive substrate (in contact with the membrane and permeable to protons) containing active centres for proton and electron recombination to H_2. Whit a different approach, a specific cathode can possess centres able to convert catalytically the CO_2 to solar fuels [30-31]. Developing an artificial leaf that collects energy in the same way as a natural one, is potentially the solution solving the problems of sustainability of energy. To avoid intermittency of solar energy, it is necessary to design systems which directly capture CO_2 and convert it into liquid solar fuels which can be easy stored. H_2 production can be seen as a necessary, but intermediate step, due to the storage difficulties of this gas. However, to be advantageous over natural leaves, it is necessary that artificial leaves have a higher solar-to-chemical conversion efficiency, provide directly the fuels which can be then used in power-generating devices, and finally be robust and of easy construction [22].

1.7 The Artificial Leaf

As discussed above, the natural leaf converts the energy of sunlight into chemical energy and splits water via the photosynthetic process to produce molecular oxygen and hydrogen, which is in a form of separated protons and electrons.

To overcome the issues of natural photosynthesis, the realization of an artificial leaf requires:

- the use of earth abundant materials,
- a good production rate,
- a good efficiency and robustness of the materials under prolonged UV-visible light.

Focusing on these statements, Nocera et al. reported the concept of “artificial leaf” by realizing a triple junction, amorphous silicon photovoltaic with hydrogen- and oxygen-evolving catalysts made from a ternary alloy (NiMoZn) and a cobalt phosphate cluster (Co-OEC) [32]. The first attempt made by Nocera involved the realization of a single junction Si cell (npp^+), a metal contact deposited in the n side and a ITO layer on the p side to protect the silicon from the electrolyte corrosion. The Co-OEC (oxygen evolution catalyst) was electrodeposited on ITO barrier to improve oxygen evolution (figure 1.4a).

Figure 1.4b show the schematic composition of the triple-junction artificial leaf made by Nocera et al.: Co-OEC and NiMoZn are interfaced with a triple junction amorphous Si (3jn-a-Si) solar cell. The 3jn-a-Si produced 8 mA cm^2 of current at 1.8 V at an overall efficiency of 6.2%. Like the single junction cell, the p-side of the cell was protected with an ITO layer. The NiMoZn was used ad HEC (hydrogen evolution catalyst) and electrodeposited onto the stainless steel support of the 3jn-a-Si cell. The NiMoZn HEC alloy may be deposited directly onto Si, to act as protection layer. When the wireless CoPi|3jn-a-Si|NiMoZn wafer was immersed in an open container of electrolyte and illuminated with sunlight, O_2 bubbles evolved from the anode at the front face and bubbles of H_2 evolved from the cathode at the back of the wireless cell, providing an efficiency of 2.5%.

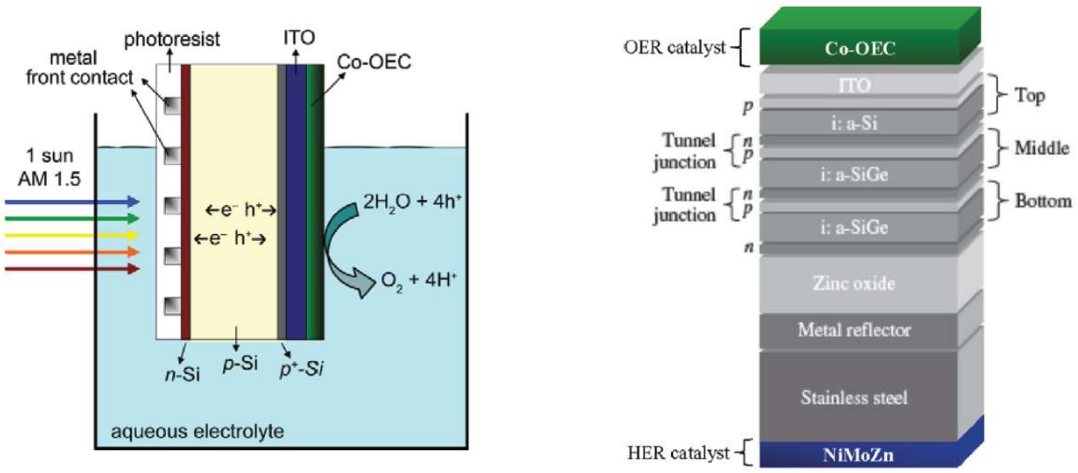

A ***B***

Figure 1.4: a) Schematic of a Co-OEC functionalized npp⁺-silicon single- junctionPECcel and ***b)*** scheme of triple junction-a-Si solar cell made by Nocera. Reproduced with permission from ref. [32].

The cell exposed by Nocera has started numerous research activities in the field of photo-electrochemical production of fuels. The different types of photo-electrochemical cell (PEC) will be discussed in the next chapter.

1.8 References

[1] *BP Statistical Review of World Energy 2018*, https://www.bp.com/, accessed 15 September (2018)

[2] P.N.R. Vennestrøm, C.M. Osmundsen, C.H. Christensen, E. Taarning, *Beyond Petrochemicals: The Renewable Chemicals Industry*, Angew. Chem. Int. Ed., 50, 10502–10509 (2011)

[3] J. A. Mathews, Greening of Capitalism, *How Asia Is Driving the Next Great Transformation*, Stanford University Press, Stanford (USA) (2015)

[4] *http://www.enea.it/it/Ricerca_sviluppo/lenergia/fonti-rinnovabili*, accessed 15 September (2018)

[5] *REN 21—Renewable Energy Policy Network for the 21st Century, Annual report 2017*, http://www.ren21.net/, accessed 15 September (2018)

[6] D. Abbott, *Keeping the Energy Debate Clean: How Do We Supply the World's Energy Needs?* Proc. IEEE, 98, 42−66 (2010)

[7] R.J. Cogdella, A.T. Gardinera, N. Yukihirab, H. Hashimotob, *Solar fuels and inspiration from photosynthesis*, J. of Photochem. and Photobiol. A: Chem., 353, 645–653 (2018)

[8] N. Armaroli, V. Balzani, *Energy for a Sustainable World—From the Oil Age to a Sun Powered Future*, Wiley-VCH, Weinheim (Germany), (2011)

[9] G. Porter, *Criteria for Solar Energy Conversion, in Light, Chemical Change and Life*, A Source Book in Photochemistry, Open University Press, Milton Keynes (UK), 338–345 (1982)

[10] V. Smil, *Energy Transitions: History, Requirements, Prospects*, Praeger/ABC-CLIO, Santa Barbara, CA (USA), (2010)

[11] D.J. Murphy, C.A.S. Hall, *Year in review—EROI or energy return on (energy) invested*, Ann. N. Y. Acad. Sci., 1185, 102–118, (2010)

[12] F. Ferronia, A. Guekosb, R.J. Hopkirkc, *Further considerations to: Energy Return on Energy Invested (ERoEI) for photovoltaic solar systems in regions of moderate insolation,* Energy Policy 107, 498–505 (2017)

[13] J.G. Lambert, C.A.S. Hall, S. Balogh, A. Gupta, M. Arnold, *Energy, EROI and quality of life*, Energy Policy 64 153-167(2014)

[14] N. Armaroli, V. Balzani, *Solar Electricity and Solar Fuels: Status and Perspectives in the Context of the Energy Transition,* Chem. an Eur. Jour., 22, 32–57 (2016)

[15] DJ Murphy, *The implications of the declining energy return on investment of oil production*, Phil. Trans. R. Soc. A 372 20120320 (2014)

[16] M. Beller, G. Centi, L. Sun, *Chemistry Future: Priorities and Opportunities from the Sustainability Perspective*, ChemSusChem, 10, 6–13 (2017)

[17] P. Lanzafame, S. Abate, C. Ampelli, C. Genovese, R. Passalacqua, G. Centi, S. Perathoner, *Beyond Solar Fuels: Renewable Energy-Driven Chemistry*, ChemSusChem, 10, 1–12 (2017)

[18] T. Mirkovic, E.E. Ostroumov, J.M. Anna, R. van Grondelle, Govindjee, G.D. Scholes, *Light absorption and energy transfer in the antenna complexes of photosynthetic organisms*, Chem. Rev. 117, 249–293 (2017)

[19] R.J. Cogdell, A. Gall, J. Kohler, *The architecture and function of the light-harvesting apparatus of purple bacteria: from single molecules to in vivo membranes*, Q. Rev. Biophys. 39, 227–324 (2006)

[20] Govindjee; R. Govindjee, *Primary Events in Photosynthesis*, Sci. Am., 231 ,68–82 (1974)

[21] J. Barber, *Photosynthetic Energy Conversion: Natural and Artificial*, Chem. Soc. Rev., 38, 185–196 (2009)

[22] S. Bensaid G. Centi E. Garrone S. Perathoner G. Saracco *Towards Artificial Leaves for Solar Hydrogen and Fuels from Carbon Dioxide,* ChemSusChem 5-3 500-521 (2012)

[23] T.H.P. Brotosudarmo, M.N.U. Prihastyanti, A.T. Gardiner, A.M. Carey, R.J. Cogdell, *The Light Reactions of Photosynthesis as a Paradigm for Solar Fuel Production,* Energy Procedia 47 283–289 (2014)

[24] G. Ciamician, *The Photochemistry of the Future*, Science, 36, 385–394 (1912)

[25] C.D. Windle, R.N. Perutz, *Advances in molecular photocatalytic and electrocatalytic CO reduction*, Coord. Chem. Rev., 256, 2562–2570 (2012)

[26] G.A. Olah, *Towards Oil Independence Through Renewable Methanol Chemistry*, Angew Chem. Int. Ed., 52, 104–107 (2013)

[27] V. Balzani, P. Ceroni, G. Bergamini, *Light: A Very Peculiar Reactant and Product*, Angew. Chem. Int. Ed, 54, 11320–11337, (2015)

[28] A. Sartorel, M. Bonchio, S. Campagna, F. Scandola, *Tetrametallic molecular catalysts for photochemical water oxidation,* Chem. Soc. Rev., 42, 2262–2280 (2013)

[29] S. Bensaid, G. Saracco, *Advanced membrane science and technology for sustainable energy and environmental applications*, Series in Energy No. 25, Woodhead Pub. Lmd, Cambridge, UK, pp. 610-644 (2011)

[30] G. Centi, S. Perathoner, R. Passalacqua, C. Ampelli, *Carbon-Neutral Fuels and Energy Carriers*, CRC Press (Taylor & Francis Group), Boca Raton, FL (US), pp. 291–323 (2011)

[31] G. Centi, R. Passalacqua, S. Perathoner, D. S. Su, G. Weinberg, R. Schloegl, *Oxide thin films based on ordered arrays of 1D nanostructure. A possible approach toward bridging material gap in catalysis,* Phys. Chem. Chem. Phys, 9, 4930-4938 (2007)

[32] D.G. Nocera, *The Artificial Leaf*, 45, 5, 767–776 Acc. Chem. Res. (2012)

2 Materials & Reactors

2.1 Titanium Dioxide (TiO_2): overview

During the last decades, scientific studies on photocatalysis have been grown at enormous rate, since the discover of photocatalytic water splitting on a semiconductor by Fujishima and Honda [1].

Titanium dioxide (TiO_2), which is one of the most basic materials in our daily life, has been widely studied and numerous scientific papers can be found in literature [2]. Fujishima et al. firstly demonstrated the possibility to conduct solar photo-electrolysis by using n-type TiO_2 semiconductor electrode, which was connected through an electrical load to a platinum black counter electrode and exposed to near-UV light (Figure 2.1) [2].

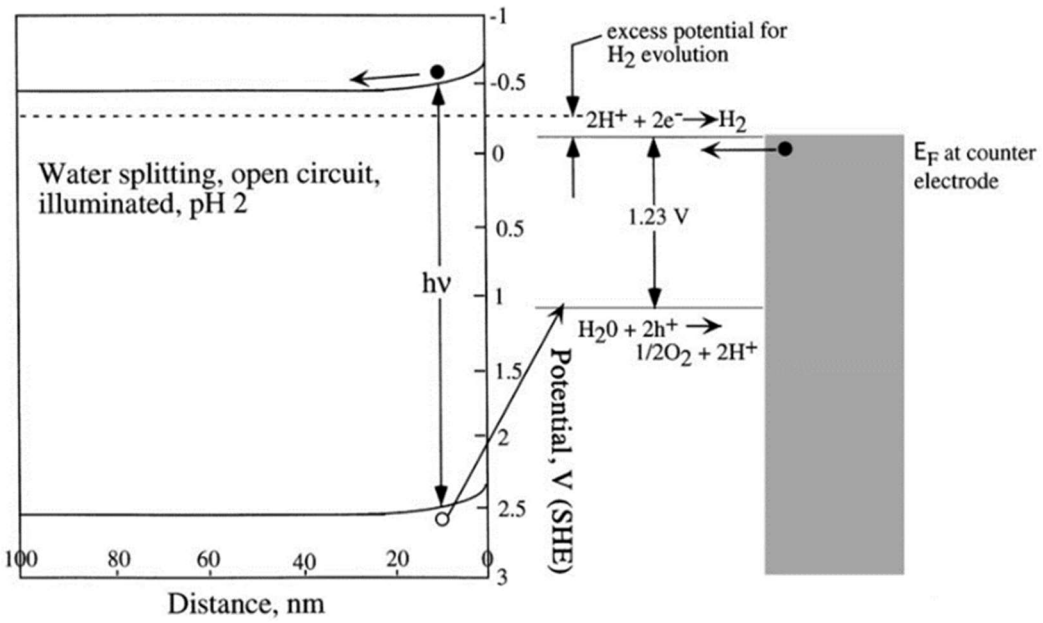

Figure 2.1: Schematic representation of photoelectrochemical water electrolysis using an illuminated oxide semiconductor electrode. Reproduced with permission from ref. [3].

When light of wavelengths in the UV region (shorter than ~415 nm) hit the surface of the TiO_2 electrode, photocurrent flowed through the external circuit from the platinum counter electrode to the TiO_2 electrode. The oxidation reaction (oxygen evolution) occurred at the TiO_2 electrode and the reduction reaction (hydrogen evolution) at the Pt electrode. Fujishima et al.

[3] demonstrated that water can be decomposed into oxygen and hydrogen, without the application of an external voltage under UV-visible light, according to the following scheme:

$$TiO_2 + 2hv \rightarrow 2e^- + 2H^+ \quad (2.1)$$

at the TiO_2 electrode

$$H_2O + 2h^+ \rightarrow (1/2)O_2 + 2H^+ \quad (2.2)$$

at the Pt electrode

$$2H^+ + 2e^- \rightarrow H_2 \quad (2.3)$$

the overall reaction is

$$H_2O + 2hv \rightarrow (1/2)O_2 + H_2 \quad (2.4)$$

Thermodynamic equilibration takes place at the interface of the semiconductor electrode, when this is in contact with an electrolyte solution. This may result in the formation of a space-charge layer within a thin surface region of the semiconductor. In the cases of n- and p-type semiconductors, the electronic energy bands are generally bent upwards or downwards, respectively. When the electrode receives photons with energies greater than that of the material's band gap (BG), electron-hole pairs are generated and separated in the space charge layer. For an n-type semiconductor, the electric field existing across the space charge layer drives the photo-generated holes towards the interfacial region and the electrons towards the interior the electrical connection to the external circuit, while for a p-type semiconductor the reverse process takes place. [4-5] If the conduction band energy (CBE) is higher than the hydrogen evolution potential, photo-generated electrons can flow through the electrical wire to the counter electrode and reduce protons. Hydrogen gas evolution can be observed in the cathode side without an applied potential.

Figure 2.2 shows the band gap energy of the mostly studied semiconductors for water splitting. It is desirable that the band gap of the semiconductor is near that for optimum utilization of solar energy. When the semiconductor electrodes are used as photoanodes or photocathodes for water electrolysis, the bandgap should be at least 1.23 eV (under standard conditions), particularly considering the existence of overpotential and polarization losses due to, for example, oxygen evolution [6].

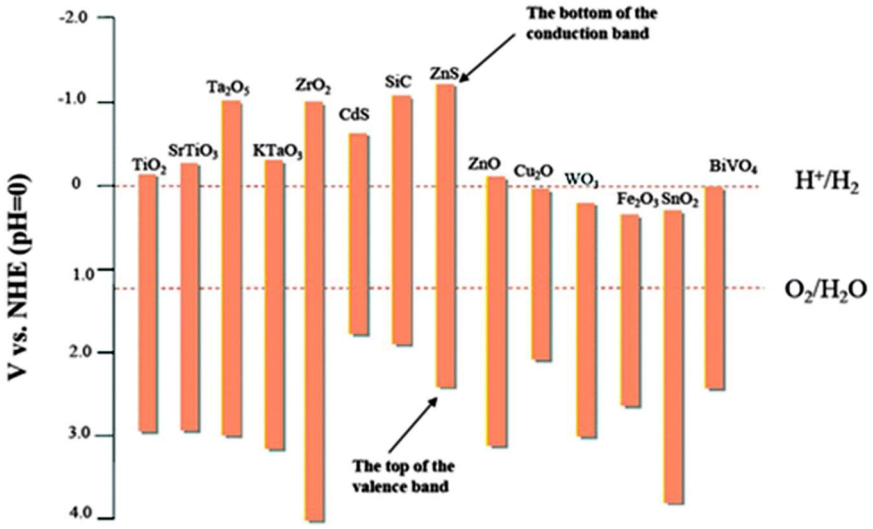

Figure 2.2: Bandgap of the most common studied semiconductor. Reproduced with permission from ref. [6].

Even if TiO_2 has been the most studied semiconductor for water splitting, it mainly shows two problems: 1) the wide energy band gap (3.0-3.2 eV) allowing it to capture light mainly in the UV region; 2) the high charge recombination rate, not allowing to convert efficiently solar energy into chemicals (i.e. H_2). Both these issues will be discussed in the next chapters through the analysis of the experimental results.

2.2 Titanium Dioxide: anatase, rutile and brookite

In nature, there are three well-known crystal structure of TiO_2: tetragonal rutile, tetragonal anatase, and orthorhombic brookite, as shown in figure 2.4. All of them consist of TiO_6 octahedrals, but differ in the distortion of the octahedron units and in the manners of sharing edges and corners. Anatase crystalline is a distorted octahedral coordination, in which every titanium atom is surrounded by six oxygen atoms in an elongated octahedral geometry, adopting axial symmetry. In rutile, additional in-plane (equatorial) and out-of-plane (axial) bond length and bond angle distortions exist, while in brookite, stronger distortions lead to a local symmetry loss and formation of symmetric TiO_6 units. The difference in crystal structure affecting their charge transfer characteristic and band energy levels [7]. For PEC applications rutile and anatase phase are the most studied because the rutile is the most thermodynamically stable form while anatase, whit higher charge mobility results more active for PEC application [8].

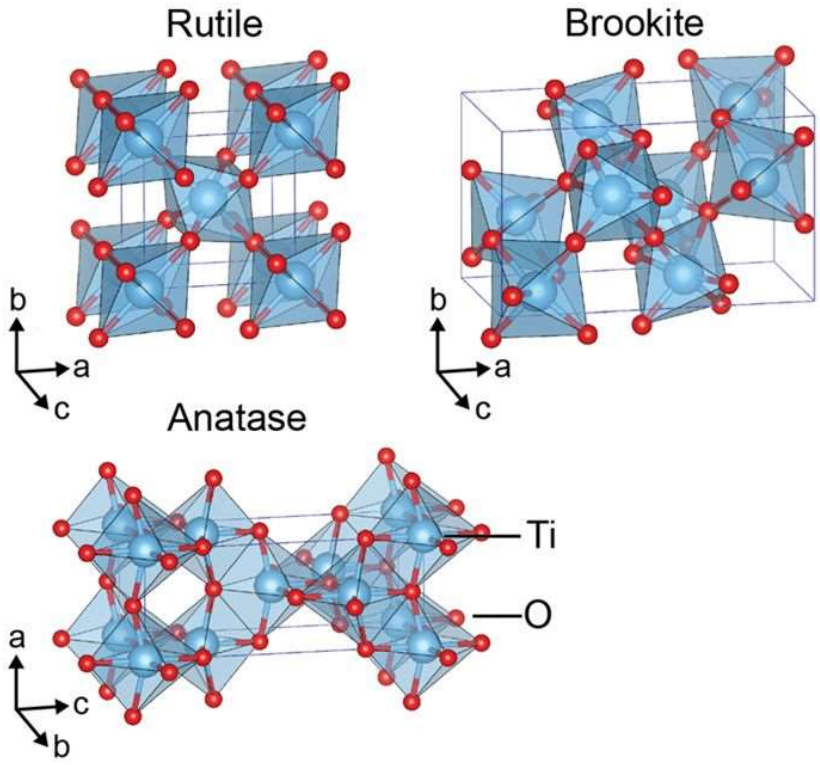

Figure 2.4: Crystal structures of TiO_2 reproduced with permission from ref. [7].

2.3 Titanium dioxide: structure engineering

TiO_2 photocatalysts can be prepared in many different shapes, both at micro and nano-scales, by using advanced technological synthetic procedures. This has opened the route to many possibilities for materials engineering, which can produce the TiO_2 materials in the appropriate nanostructure and morphology in order to obtain the best performances depending on their application.

In general, there are many factors that can significantly influence photocatalytic performances (size, specific surface area, pore volume, pore structure, crystalline phase and exposed surface facets). One of the main aims in photocatalysis is to find the proper synthesis conditions in order to "tailor" the structure of the semiconductor (TiO_2 in this case) and finally relate these conditions to the photocatalytic activity.

According to their structure dimensionality and geometry, TiO_2 materials can be divided in different categories, starting to classic spheres that are considered as zero dimensional (0D), and moving to one dimensional rods and tubes (1D), two dimensional sheets (2D) and interconnected three dimensional architectures (3D) (see Figure 2.3) [9].

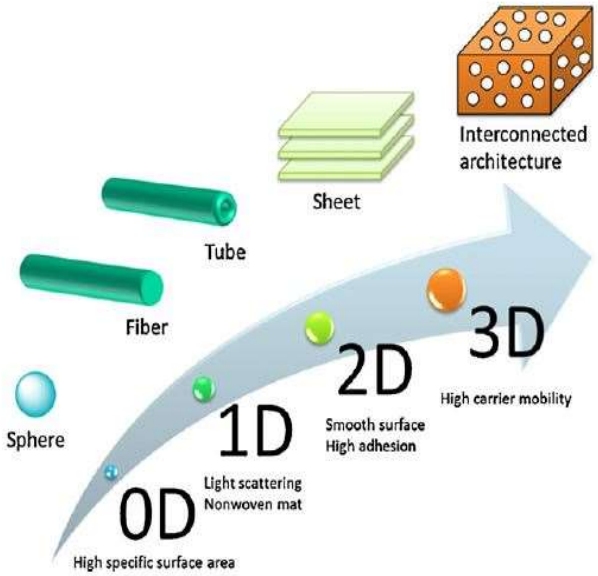

Figure 2.3: Schematic illustration of structural dimensionality of materials with expected properties, reproduced with permission from ref. [9].

2.3.1 Zero dimensional (0D): spheres

Nano- or micro-structured TiO_2 spheres are the most widely studied and used in TiO_2-photocatalysis. TiO_2 spheres usually possess a high specific surface area and a high pore volume and pore size, with these properties increasing the size of the accessible surface area and the rate of mass transfer for organic pollutant adsorption [10]. TiO_2 nanoparticles are the common element to realize nano films in dye-sensitized solar cells; Grätzel and co-workers have made great contribution to dye-sensitized TiO_2 solar cells by studying the effects of nanoparticle size, morphologies and film thickness [11]. These porous structures increase the light-harvesting capabilities of TiO_2 because they enhance light use by allowing the light to access the interior of the particle [12-13]. TiO_2 spheres are typically prepared from a titanium alkoxide such as titanium tetraisopropoxide or titanium tetrabutoxide, in the presence of a polymer to provide a porous structure and with or without the addition of an acid to accelerate the reaction [14]. Depending on the annealing temperature, TiO_2 spheres can have different structures. Annealing at high temperatures usually decreases the specific surface area of the TiO_2 spheres, which exhibit superior photocatalytic activities. For example, Zheng et al. prepared TiO_2 spheres that were annealed at 400 °C, showing for this temperature the highest photocatalytic

activity in the decomposition of organic molecules, because of their high specific surface area and highly crystalline form [15]. Size control of the particle is another key element to enhance the photocatalytic activity [16].

2.3.2 One dimensional (1D): fibers & tubes

TiO_2 materials with one-dimensional structures includes fibers and tubes, possess higher surface-to-volume ratio enabling a strong reduction of the hole–electron recombination rate and a high interfacial charge carrier transfer rate. With these unique properties, 1D TiO_2 materials represent the perfect choice for photocatalytic reactions [17]. The one-dimensional architecture allows to obtain self-standing membranes; nonwoven mats can be obtained only from this kind of architecture, which opens to a wide range of applications. TiO_2 fibers have already been used in an extensive range of applications, including photocatalysis, gas sensing [18], dye-sensitized solar cells (DSSCs) [19] and batteries [20]. The common synthesis to prepare TiO_2 fibers are the electrospinning of a mixture of titanium alkoxide and a polymer, with a necessary calcination step to remove the residual polymer and crystallize the TiO_2 (see Figure 2.5) [21].

By changing the synthesis parameters (such as the ratio polymer/titanium alcoxide, the power of the electric field, and the feeding rate of the precursor in the electrospinning process), the average diameter of the TiO_2 fibers can be controlled. TiO_2 fibers generally prepared by electrospun generally possess a large surface area-to-volume ratios and provide efficient photocatalytic performances [22].

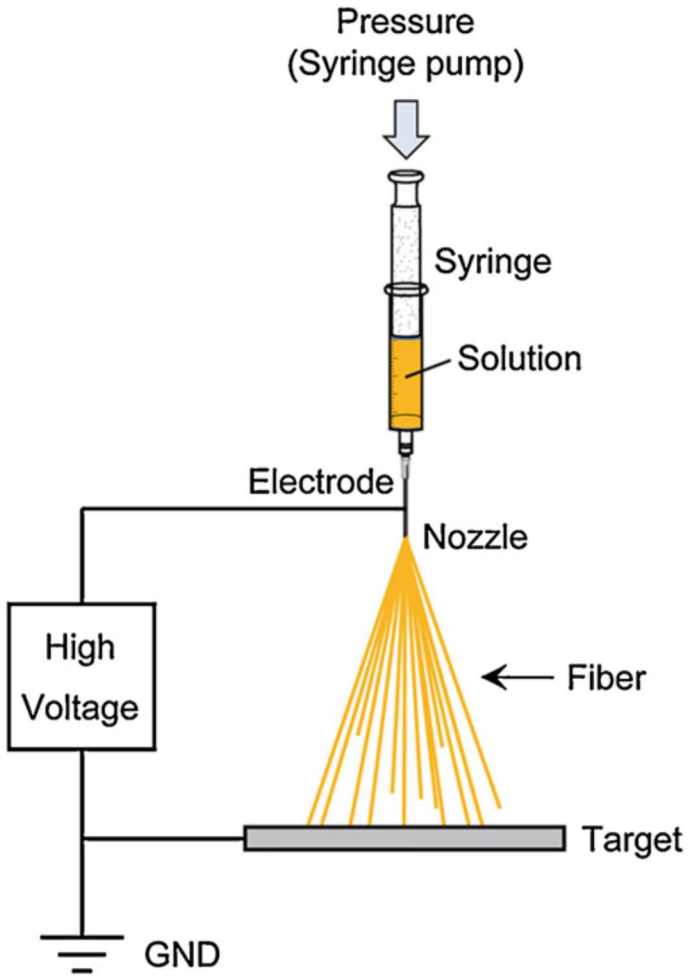

Figure 2.5: Schematic illustration of the setup for electrospinning. Reproduced with permission from ref. [9].

Nanotubes are of great interest due to their high surface-to-volume ratios and size dependent properties: Compared to nanowires, TiO_2 nanotubes have much been investigated and various techniques have been developed for their synthesis. Titania nanotubes and nanotube arrays have been produced by a variety of methods including deposition into a nanoporous alumina template [23], sol–gel [24-25], and hydrothermal processes [26]. However, among these nanotube fabrication routes, anodization technique is the most powerful tool for the fabrication of highly ordered TiO_2 nanotube arrays [27-28].

Anodization is typically conducted in an electrolyte containing a hydrogen fluoride (HF)-based aqueous solution, using a two-electrode electrochemical cell with a platinum as counter electrode (cathode) at a constant potential. Figure 2.6 reports a schematic diagram of the electrochemical apparatus needed to carry out the anodization process. At the end of the anodization process, TiO_2 nanotube arrays are formed on the foil surface and have straight channels against the Ti foil (which acts as electron collector layer in PEC systems). Fabrication

of titania nanotube arrays via anodic oxidation of titanium foil in a fluoride-based solution was first reported in 2001 by Grimes and co-workers [29] followed by further studies focused on precise control and extension of the nanotube morphology: [30], length and pore size, and wall thickness [31]. Every single parameters of the synthesis determine the morphologies of the tubes. The electrolyte composition and pH determine the rate of nanotube array formation, as well as the rate at which the resultant oxide is dissolved [32]. In all cases, a fluoride ion containing electrolyte is needed for nanotube array formation. Ordered TiO_2 helical nanocoil arrays can also be synthetized using 0.5 wt.% HF electrolyte [33].

Magnetic agitation is necessary during anodization experiments to reduces the thickness of the double layer at the metal/electrolyte interface, and ensures uniform local current density and temperature over the Ti electrode surface.

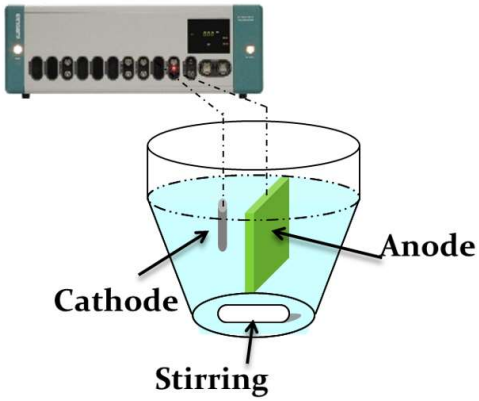

Figure 2.6: Illustrative drawing of a two-electrode electrochemical cell in which the Ti samples are anodized.

The key processes for the anodic formation of titania nanotube are: (1) Oxide growth at the surface of the metal occurs due to interaction of the metal with O_2 or OH^- ions. After the formation of an initial oxide layer, these anions pass through the oxide layer and reach the metal/oxide interface where they react with the metal. (2) Metal ion (Ti^{4+}) migrate from the metal to the metal/oxide interface; Ti^{4+} cations are removed from the metal/oxide interface under application of an electric field, moving towards the oxide/electrolyte interface. (3) Field assisted dissolution of the oxide at the oxide/electrolyte interface. Due to the applied electric field, the Ti–O bond undergoes polarization and is weakened promoting dissolution of the metal cations. Ti^{4+} cations dissolve into the electrolyte, and the free O_2 anions migrate towards

the metal/oxide interface - see process (1) - to interact with the metal. (4) Chemical dissolution of the metal, or oxide, by the acidic electrolyte also takes place during anodization. Chemical dissolution of titania in the HF electrolyte plays a key role in the formation of nanotubes rather than a nanoporous structure. The overall reactions for anodic oxidation of titanium can be represented as:

$$2H_2O \rightarrow O_2 + 4e^- + 4H^+ \quad (2.5)$$

$$Ti + O_2 \rightarrow TiO_2 \quad (2.6)$$

In the initial stages of the anodization process, field-assisted dissolution dominates chemical dissolution due to the relatively large electric field across the thin oxide layer. Small pits formed due to the localized dissolution of the oxide, represented by the following reaction, act as pore forming centers (Figure 2.7 a-b):

$$TiO_2 + 6F^- + 4H^+ \rightarrow TiF_6^{2-} + 2H_2O \quad (2.7)$$

Then, these pits convert into bigger pores and their density increases. After that, the pores spread uniformly over the surface. The pore growth occurs due to the inward movement of the oxide layer at the pore bottom (Figure 2.7 c-d). The Ti^{4+} ions, migrating from the metal to the oxide/electrolyte interface, dissolve in the HF electrolyte. The rate of oxide growth at the metal / oxide interface and the rate of oxide dissolution at the pore-bottom / electrolyte interface ultimately become equal; thereafter the thickness of the barrier layer remains unchanged although it moves further into the metal making the pore deeper (Figure 2.7c).

The anodization potential (as the concentration of electrolytes electrochemical) operates on the etch rate: if the electrochemical etch proceeds faster than the chemical dissolution the thickness of the barrier layer increases, which in turn reduces the electrochemical etching process to the rate determined by chemical dissolution. The chemical dissolution rate is determined by the F^- concentration and solution pH (reaction 2.7) [34].

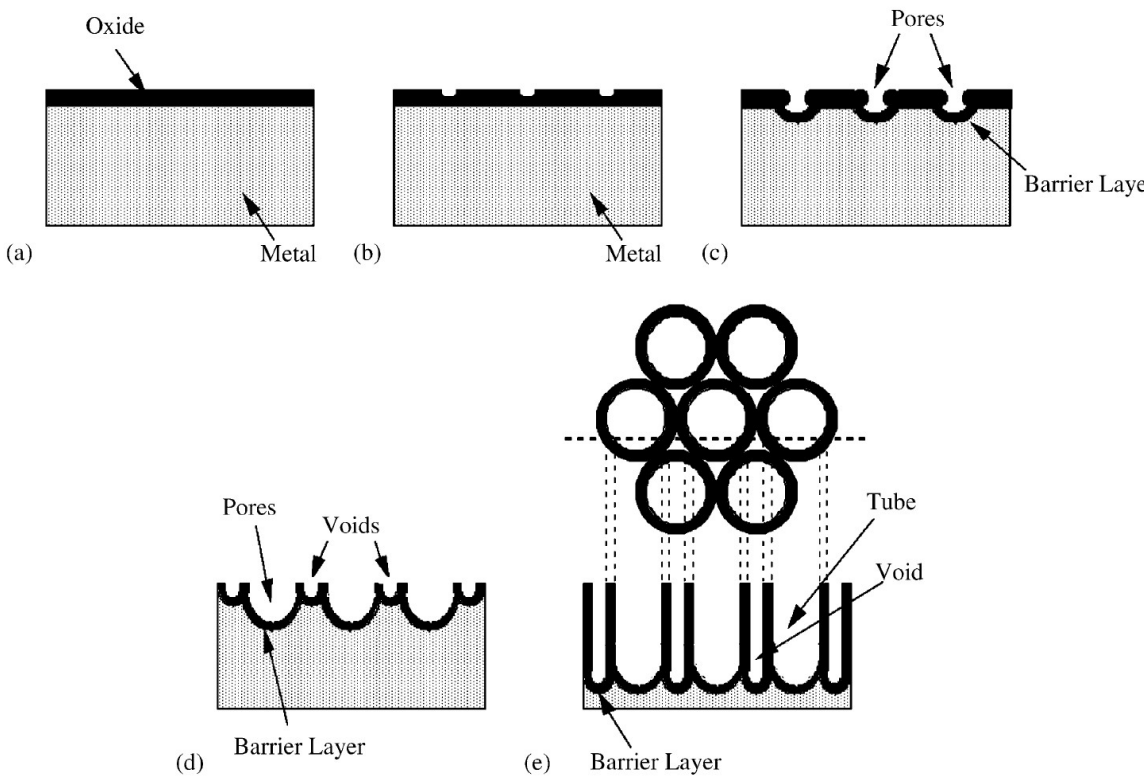

Figure 2.7: Schematic diagram of the evolution of a nanotube array at constant anodization voltage: (a) oxide layer formation, (b) pit formation on the oxide layer, (c) growth of the pit into scallop shaped pores, (d) metallic part between the pores undergoes oxidation and field assisted dissolution, and (e) fully developed nanotube array with a corresponding top view. Reproduced with permission from ref. [34].

Chemical dissolution increases with increasing F^- and H^+ concentrations. Growth of nanotube arrays can be achieved only in a certain F concentration range (from 0.05 to 0.3 mol/L in acidic solution).

2.3.3 Two dimensional (2D): nanosheets

Like the above discussed 1D structures, the 2D structures possess the advantage of a direct electron pathway but they have a higher specific surface area. A nanosheet is a flake-shaped material with a flat surface and high aspect ratio. Nanosheets can be prepared whit very small thickness of 1–10 nm and a lateral size can reach several tens of micrometers. This kind of shape results in low turbidity, excellent adhesion to substrates, and high smoothness, suitable for photocatalytic application. [35] Nanosheets present also superhydrophilicity under UV irradiation, a characteristic needed for self-cleaning coating. [36]. TiO_2 nanosheets are typically

prepared according to an alkaline hydrothermal process using TiO_2 powder as a precursor, followed by either a calcination process or hydro/solvothermal reactions [37].

2.3.4 Three dimensional (3D): interconnected architecture

The three-dimensional hierarchical structures of TiO_2 are important for practical applications because possess an intricate pore structure and large surface to-volume ratios, this provides a significant advantage in diffusion pathways for guest species, such as organic pollutants opening the possibilities to conduct efficient purification, separation, and storage. The interconnected structure is potentially superior not only for carrier mobility, but also from a practical point of view. For example, Konishi et al. prepared macroporous TiO_2 monoliths for use in chromatographic applications (Figure 2.7) [38], while Saravanan et al prepared mesoporous TiO_2 for Li storage [39].

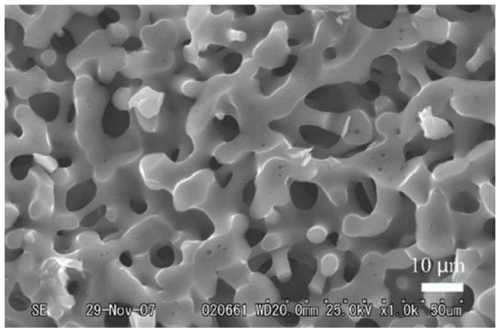

Figure 2.7: SEM image of TiO_2 sponge. Reproduced with permission from ref. [38].

2.4 Titanium dioxide: strategies to improve performances

Various strategies can be adopted for improving the photocatalytic efficiency of TiO_2. They can be summarized as either morphological modifications, such as increasing surface area and porosity, or as chemical modifications, by incorporation of additional components in the TiO_2 structure: noble metal, non-noble metals, nitrogen, sulphur and carbon.

2.4.1 Metal particle deposition

Modifications of TiO_2 with transition metals such as Cr, Co, V and Fe have extended the spectral response of TiO_2 well into the visible region also improving photocatalytic activity [40] [41] However, transition metals may also act as recombination sites for the photo induced charge carriers thus, lowering the quantum efficiency. Transition metals have also been found to cause thermal instability to the anatase phase of TiO_2. Kang argued that despite a decrease in band gap energy has been achieved by many groups through metal doping, photocatalytic activity has not been remarkably enhanced because the metals introduced were not incorporated into the TiO_2 framework. In addition, metals remaining on the TiO_2 surface block reaction sites [42].

TiO_2 has been modified with many transition metals such as Fe, Cu, Co, Ni, Cr, V, Mn, Mo, Nb, W, Ru, Pt and Au [43-44] The incorporation of transition metals in the titania crystal lattice may result in the formation of new energy levels between valence band (VB) and conduction band (CB), inducing a shift of light absorption towards the visible light region. Photocatalytic activity usually depends on the nature and the amount of doping agent. Possible limitations are photocorrosion and promoted charge recombination at metal sites [45]. Deposition of noble metals like Ag, Au and Pd on the surface of TiO_2 enhances the photocatalytic efficiency under visible light by acting as an electron trap, promoting interfacial charge transfer and therefore delaying recombination of the electron–hole pair [46-47-48]. The visible light responsiveness of TiO_2 was accredited to the localized surface plasmon resonance (LSPR) of few metals nanoparticles such as Au, Ag and Cu (Figure 2.8). LSPR is an optical phenomenon that appears when the wavelength of the incident light is higher than the metal NP size.

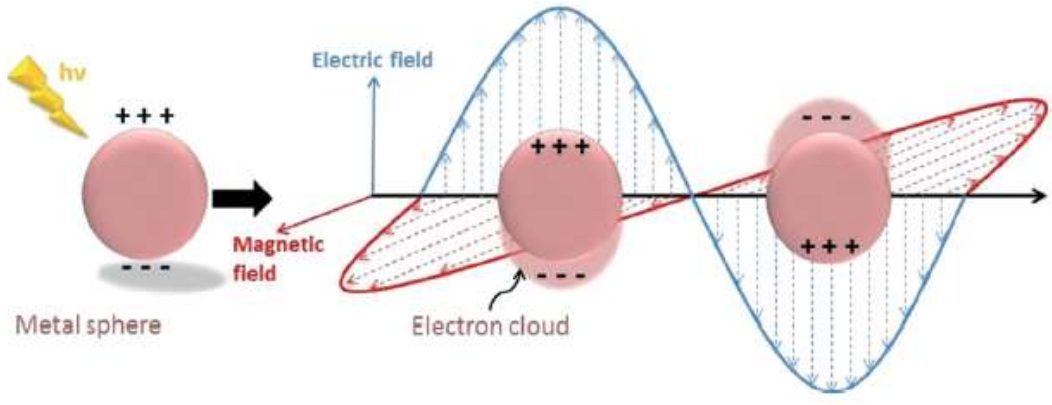

Figure 2.8: Schematic illustration of LSPR reproduced from ref. [49].

2.4.2 Metal free methods

In order to enhance the solar efficiency of TiO_2 under solar irradiation, it is necessary to modify the nanomaterial to improve visible light absorption. Non-metal doping of TiO_2 has shown great promise in achieving visible light absorber photocatalysis, with nitrogen being the most promising dopant because nitrogen can be easily introduced in the TiO_2 structure. [50-51]. Nitrogen has a comparable atomic size with oxygen, small ionization energy and high stability. Asahi and co-workers explored for first time the visible light activity of N-doped TiO_2 produced by sputter deposition of TiO_2 under a N_2/Ar atmosphere, followed by annealing under N_2 [52]. There are many methods to introduce N in TiO_2 materials, either in the bulk or as a surface dopant. For the efficient incorporation of nitrogen into TiO_2, several methods have been adopted: physical techniques such as sputtering [53] and ion implantation [54], gas phase reaction methods [55], atomic layer deposition [56] and pulsed laser deposition [57].

Fluorine doping does not shift the TiO_2 band gap; however, it improves the surface acidity and causes formation of reduced Ti^{3+} ions due to the charge compensation between F^- and Ti^{4+}. Thus, charge separation is promoted and the efficiency of photo-induced processes is improved [58].

Adding carbon, phosphorous and sulphur as dopants improves the light activity of TiO_2. These dopants change the lattice parameters, and the presence of trap states within the conduction and valence bands, gives rise to band gap narrowing. The effect is to improve visible light absorption and increase the lifetime of photo-generated charge carriers. [59] Carbon graphene oxide quantum dots (GOQD) were successfully added in-situ, during the anodization, resulting in C doped TiO_2 with an increased conductivity and photocatalytic activity [60].

Insertion of sulphur into the TiO_2 lattice is more difficult to obtain, due to its larger ionic radius. Insertion of cationic sulphur (S^{6+}) is chemically favourable over the ionic form (S^{2-}) lattice. Visible light-activated sulphur doped TiO_2 films were successfully synthesized using a novel sol–gel method based on the self-assembly technique with a non-ionic surfactant to control nanostructure and H_2SO_4 as an inorganic sulphur source [61]. S-doped TiO_2 obtained with H_2S showed better performances in the methylene blue photodegradation test compared to pure TiO_2 [62].

2.4.3 Dye sensitation

Dye photosensitization has been reported by different groups as one of the most effective ways to extend the photo-response of TiO_2 into the visible region. Indeed, these types of reactions are exploited in the well-known dye sensitized solar cells [63]. The mechanism of the dye sensitized photo-degradation of pollutants is based on the absorption of visible light for exciting an electron from the highest occupied molecular orbital (HOMO) to the lowest unoccupied molecular orbital (LUMO) of a dye. The excited dye molecule subsequently transfers electrons into the conduction band of TiO_2, while the dye itself is converted to its cationic radical. The TiO_2 acts only as a mediator for transferring electrons from the sensitizer to the substrate on the TiO_2 surface. In this process, the LUMO of the dye molecules should be more negative than the conduction band of TiO_2. The injected electrons hop over quickly to the surface of titania where they are scavenged by molecular oxygen to form superoxide radical $O_2^{\bullet-}$ and hydrogen peroxide radical •OOH. These reactive species can also disproportionate to give hydroxyl radical [64]. In addition to the mentioned species, singlet oxygen may also be formed under certain experimental conditions. Oxygen has two singlet excited states above the triplet ground ones. Such relatively long live oxygen species may be produced by quenching of the excited state of the photosensitizer by oxygen. The subsequent radical chain reactions can lead to the degradation of the dye. Knowledge of interfacial electron transfer between semiconductor and molecular adsorbates is of fundamental interest and essential for applications of these materials.

2.5 Tantalum-oxy-nitride (TaO_xN_x)

To overcome the above discussed limitation of TiO_2 photocatalyst, it is possible to explore other semiconductors. TaO_xN_x photocatalysts are very attracting materials due to their band low gap of about 2.1 eV and suitable band positions (see figure. 2.2). Ta_3N_5 can utilize a large portion of the solar spectrum (<600 nm), and it is considered to be one of the most promising photoanodes for solar water splitting, as Ta_3N_5 can reach a theoretical maximum of about 16% light conversion under AM 1.5G irradiation [65]. A common path to synthesize Ta_3N_5 is nitridation of Ta_2O_5 by a high temperature NH_3 treatment. Previous reports on Ta_3N_5 nanorod fabrication use hydrothermal methods with Ta powders [66] or use porous anodic alumina

(PAA) as a template for through mask anodization with a two-step anodization process, to grow the Ta_2O_5 precursors [67].

It is possible to prepare Ta oxide nanotubes by using the above discussed anodization method. Anodization of Ta in pure inorganic acids (sulphuric or phosphoric acid) or organic acids (citric or oxalic acid) is a typical solution used to form ordered, porous oxide films on metals such as Al and it has been found in the past to work better also for field-assisted growth of compact Ta oxide films (Equation 2.8) [68].

$$2Ta + 5H_2O / Ta_2O_5 + 10H^+ + 10e^- \quad (2.8)$$

Porous Ta oxide films are not formed in this case, as Ta_2O_5 has insufficient solubility in these solutions and thus the oxide does not dissolve concurrently with compact oxide film formation. It is widely accepted that competition between oxide growth and dissolution leads to the continuous growth of porous oxide films. The first report of porous Ta_2O_5 film formation [69] involved Ta anodization in 1 M H_2SO_4, but only when an aggressive ion (e.g. F^-) was added in the form of HF (1–3 wt%). Fluoride ions are known to chemically attack Ta oxide, and, during anodization, have been found to provide the required dissolution rate of the oxide film at certain sites (Equation 2.9), thus creating a porous oxide film. The applied electrical field ensures that the compact Ta_2O_5 film continuously reforms (Equation 2.8) at the base of the pores.

$$Ta_2O_5 + 10H^+ + 14F \rightarrow 2[TaF_7]^{2-} + 5H_2O \quad (2.9)$$

Generally, Ta_3N_5 nanotubes (NTs) and nanorods (NRs) show a significantly higher photo response compared to nanoparticles or compact film electrodes. A particularly promising synthesis approach is nanotube formation by self-organizing anodization of tantalum, leading to Ta_2O_5 tubes that then are converted into Ta_3N_5 by ammonolysis. Such tubes are closed at their bottom end, and several reports show that these bottom layers (the interface to the metal underneath) often determine the resistivity of the entire nanostructured electrode [67]. The interface between Ta_3N_5 NTs and the underlying substrate is of crucial importance for an efficient charge transfer in the photo-electrochemical circuit. The formation of subnitrides, and thus the conductivity across this interface, can be drastically affected by the anodization

treatment used to form the precursor oxide tubes. Schmuki and coworkers [70] introduce a two-step anodization method to form the oxide tubes, which—after subsequent high-temperature nitridation (1000 °C)—leads to better-ordered Ta_3N_5 NTs with an increased amount of beneficial subnitride species, which increase the interface conductivity, and a red-shift of the visible-light absorption (figure 2.9).

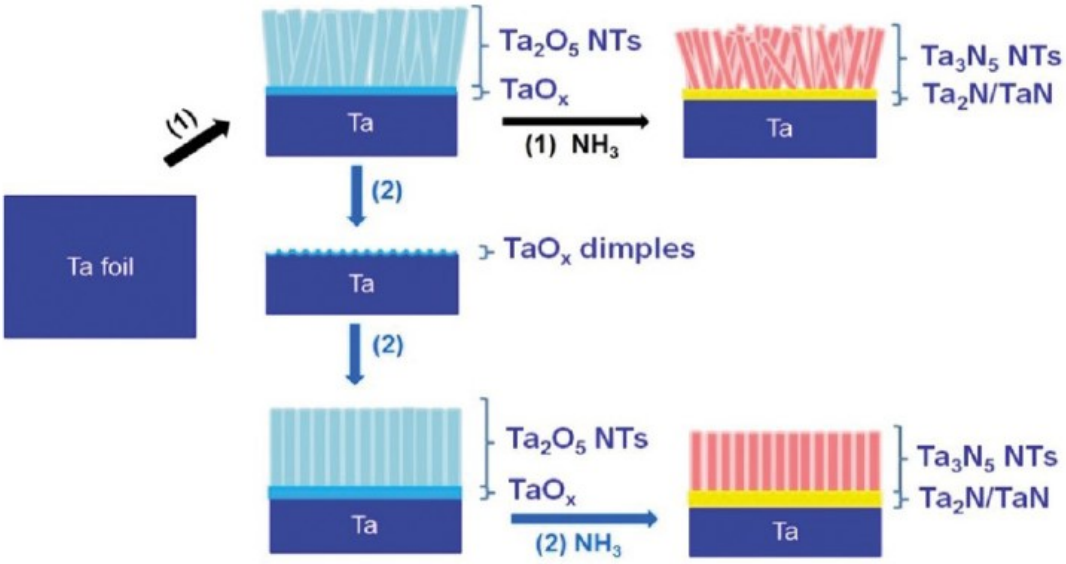

Figure 2.9: Schematic illustration of the synthesis process of Ta_2O_5 and Ta_3N_5 NTs. Reproduce with permission from ref. [70].

Route (1) represents the conventional path to Ta_3N_5 nanotubes. That is, tantalum metal is anodized under self-organizing conditions in a H_2SO_4 + HF electrolyte

This results in Ta_2O_5 nanotubes which can then be converted into Ta_3N_5 by thermal treatment in NH_3 flow. The method introduced here removes the first anodic layer of Ta_2O_5 tubes and re-anodizes the material a second time (this follows an approach originally introduced for porous alumina to obtain a higher degree of order in an aligned porous oxide structure [71]. This second, more ordered nanotubular oxide layer is then converted to Ta_3N_5 NTs [72].

2.6 Reactors

Not only the study and the development of electrode materials is necessary to move forward to a new green economy but also the development of the reactors and cells plays a significant role. The ability to develop both the electrodes and the cells (side by side) leads to better results and performances.

Before starting to develop a new cell for the production of solar fuels, many aspects should be taken in account, deriving mainly from the final use of the cell. These aspects must be included at the initial stage, because they determine the choice of the materials:

- It is necessary to conduct the oxidation and reduction reactions in two separate zones of the cells, to avoid safety problems, reduce costs of separation and limit quenching effects.
- It is preferable to avoid liquid electrolytes for easiest product recovery and protection of the electrodes/cell elements from corrosion.
- It is recommended to have a compact design for easily scale-up.
- The device needs to operate in continuous under UC-visible light, with stable performances above 50–60◦C.

These aspects determine the cell design/engineering and in turn the characteristics necessary in the cell element, such as electrodes and catalytic components [73].

2.6.1 Conventional reactors

The easiest and most studied reactor for photocatalytic reaction is the classic slurry in liquid phase. Today is it possible to find several companies that supply commercial slurry photoreactors in the classic configuration that have a UV lamp immersed in the solution chamber. However, the photoreactor in slurry phase suffers from different issues mainly related to the light scattering phenomena and the difficult product recovering.

2.6.2 Gas phase reactors (GP)

Gas-phase operation may introduce several advantages with respect to conventional photo-reactors working under slurry conditions. Figure 2.10 shows the home made set-up made by

Ampelli et al.; [74] it uses a thin film of the solid catalyst (avoiding the problems related to separation, leaching, etc.) in contact with a gaseous organic stream.

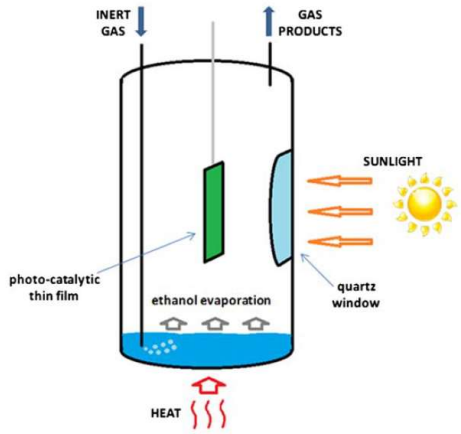

Figure2.10: Simplified scheme of the gas phase photo-reactor used by Ampelli et al. [74].

From the application perspective, it would also be interesting the possibility to perform the photocatalytic dehydrogenation of ethanol to H_2 instead of the ethanol photoreforming. In this way, it is possible to obtain acetaldehyde, which is considered as a valuable chemical product:

$$CH_3CH_2OH \rightarrow CH_3CHO + H_2 \qquad \text{(photo-dehydrogenation)} \qquad (2.10)$$

$$CH_3CH_2OH + 3H_2O \rightarrow 2CO_2 + 6H_2 \qquad \text{(photoreforming)} \qquad (2.11)$$

The potential advantages of operating in gas phase with respect to the traditional slurry photo-chemical reactors are the following: (1) minimization of scattering phenomena, (2) good pattern of irradiation, (3) ability to transfer the power coming from sunlight to a conductive substrate, (4) easier scale-up, (5) elimination of problems associated to metal-leaching and (6) easier product recovery

2.6.3 Photo-electrochemical cell (PEC)

The possibility to perform the photosynthesis in an artificial device (that produces efficiently solar fuels with the desired selective towards high value-added products) requires the

development of advanced systems and technologies. The Photo-electrochemical (PEC) approach represents a new challenge to move to a renewable energy economy [75]. Starting from the same base concept of the natural photosynthesis, already discussed in Chapter 1, H_2 equivalents (H^+/e^-) coming from the electrolysis of water can easily be converted to solar fuels by feeding CO_2 [75].

Also known as artificial leaf, this type of device needs many elements to be competitive. First of all, like every photocatalytic device, the anode must have: i) sites able to capture light in the visible region and generate the charge separation; ii) a membrane that separates the two reaction compartments and ii) a cathode able to reduce the protons into H_2 or solar fuels in the presence of CO_2. The materials that constitute the PEC cell must be: robust and resistant to high temperatures, resistant to corrosion and photocorrosion, low costly and be selective towards the desired reduction products.

Ampelli et al. distinguished two main classes of PEC cells (Figure 2.11) [73]: 1) conventional PEC cells and 2) modified PEC cells. In a "conventional" PEC cell, water is oxidized and reduced in the same liquid electrolyte (Figure 2.11a). The "modified" PEC cell proposed by Nocera et al. [77-78] represents essentially the integration of a single unit of PV with an electrolysis device (Figure 2.11b). The efficiency reported in water photo-electrolysis by Nocera was 6.2%, which significantly decreased when the oxygen evolution catalyst (OEC) and hydrogen evolution catalyst (HEC) were located in different compartments.

Amorphous silicon PV cells suffer from corrosion when immersed in the electrolyte and a protective layer is needed, for example a photo-resistant layer and a film of ITO or TiO_2 on both the n and p sides. Another important aspect of PEC cell is the use of the membrane that is necessary to have separate zones for H_2 and O_2 evolutions. The membrane guarantees the separation of H_2 and O_2 solving important issues related to: (1) safety, avoiding risk of explosion and (2) costs, with an easiest recovery of the products.

The efficiency of PEC cells is based on two aspects: the first regarding the ability to convert sunlight into photocurrent and the other one to convert the charge generated into the final products. Regarding the first aspect (conversion of light into current), two important parameters can be used: 1) quantum efficiency, expressed as IPCE and APCE (incident/absorbed photon to current efficiency) and 2) photoconversion efficiency, also called as solar-to-hydrogen (STH) efficiency, useful for a complete evaluation of the whole process. All these indicators will be discussed and investigated within the next chapters.

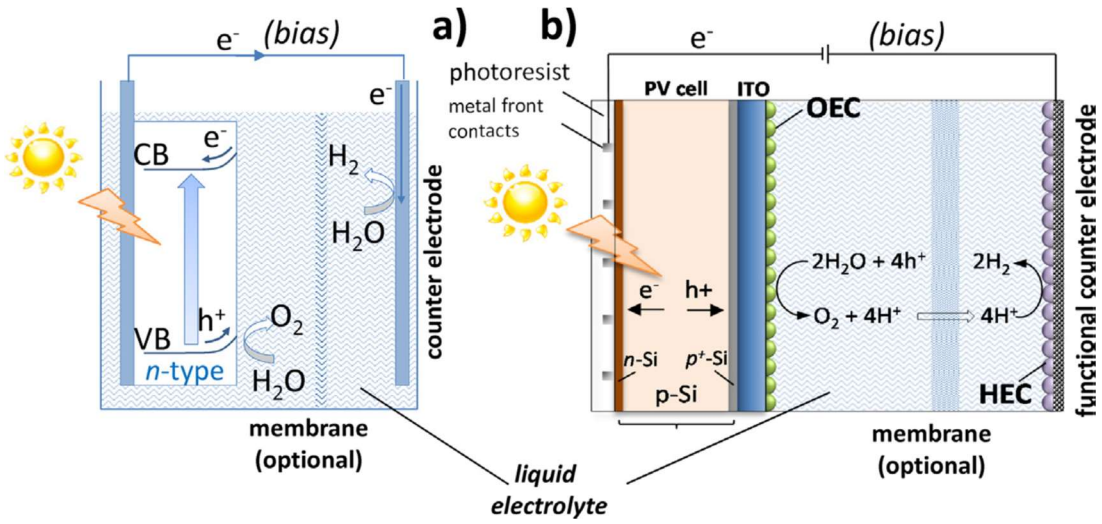

Figure 2.11: (a) Conventional PEC solar cell (n-type oxide semiconductor layer) operating in a liquid electrolyte. (b) PV cell (in the drawing a single junction cell, but can be a multijunction cell) integrated in a conventional PEC cell operating in liquid electrolyte [73].

The types of cell schematically shown in Figure 2.11 are not suitable to operate over room temperature, which can enhance hot electron transfer and significantly increase solar-to-electric power conversion efficiencies. Developing of PEC solar cells operating at higher temperatures, may allow coupling with solar concentrators (under these conditions, temperatures can reach over 100°C), thus reducing further the cost of PEC solar devices and increasing the reaction kinetics.

C. Ampelli et al. [73] introduce the concept of "electrolyte less (EL)" cell. EL defines a cell based on the construction of membrane electrode assembly (MEA) consisting of two nanostructured porous electrodes directly in contact with a membrane that is not immersed in the electrolyte. The electrolyte is formally absent in EL configuration, although a liquid film is necessary to improve ion conductivity and improve surface conductivity. The protons, generated at the photoanode side, diffuse first through the porous anode, then through the membrane and finally recombine with the electrons to generate H_2 or hydrogenate CO_2. Electrons are instead collected at the anode and transported to the conductive cathode through an external wire (see Figure 2.12a) It is possible to realize both n-type and p-type EL PEC cells with this configuration.

The use of EL design for PEC cells opens a wide range of possibilities to develop new nanomaterials, and the present PhD thesis work focuses on the development of innovative materials to be used as photoanodes in a n-type EL PEC cell [79].

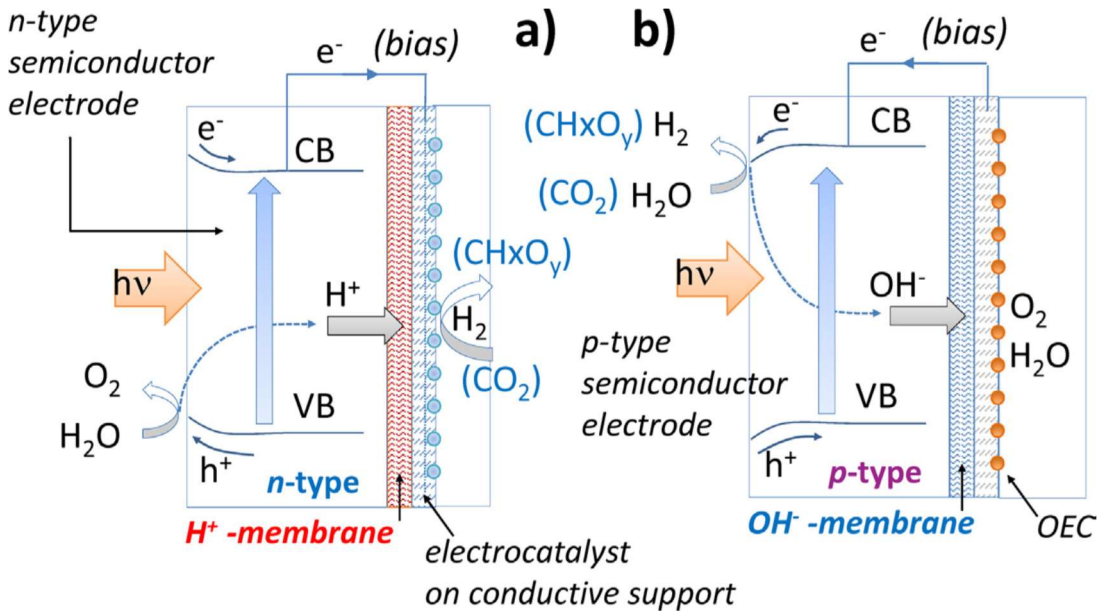

Figure 2.12: Electrolyte-less (EL) design for PEC solar cell based on (a) n-type and (b) p-type oxide semiconductor layer as the photoactive element. Reproduced with permission from [73].

2.7 References

[1] Fujishima, K. Honda, *Electrochemical Photolysis of Water at a Semiconductor Electrode*, Nature 238, 37–38 (1972)

[2] Fujishima, T.N. Rao, D.A. Tryk, *Titanium dioxide photocatalysis*, Jour. of Photochem. and Photobio. C: Photochem. Rev. 1, 1–21 (2000)

[3] Fujishima, D.A. Tryk, K. Honda, *Photoelectrochemical Conversion*, Functionality of Molecular Systems, Vol. 2, Springer, Tokyo, 196–224 (1999)

[4] W. Jaegermann, *The semiconductor/electrolyte interface: a surface science approach, in: R.E*. White, B.E. Conway, J. O'M. Bockris (Eds.), Modern Aspects of Electrochemistry, 30, Plenum Press, New York, pp. 1–185 (1996)

[5] L.M. Peter*, Photoelectrochemical kinetics at semiconductor electrodes*, in: R.G. Compton, G. Hancock (Eds.), Applications of Kinetic Modeling, 37, Elsevier, Amsterdam, 223–279 (1999)

[6] L. Yang, H. Zhou, T. Fan D. Zhanga, *Semiconductor photocatalysts for water oxidation: current status and challenges* Chem. Phys,16, 6810-6826 (2014)

[7] J.E.S. Haggerty, L.T. Schelhas, D.A. Kitchaev, J.S. Mangum, L.M. Garten, W. Sun, K.H. Stone, J.D. Perkins, M.F. Toney, G. Ceder, D.S. Ginley, B.P. Gorman, J. Tate, *High-fraction brookite films from amorphous precursors* Scient. Rep. 7, 15232 (2017)

[8] Luttrell T, Halpegamage S, Tao J, Kramer A, Sutter E, Batzill M, *Why is anatase a better photocatalyst than rutile? Model studies on epitaxial TiO_2 films*, Scient. Rep., 4, 40-43 (2014)

[9] K. Nakata, A. Fujishima, *TiO_2 photocatalysis: Design and applications*, J. of Photochem. and Photobio. C: Photochem. Rev. 13, 169– 189 (2012)

[10] Y. Kondo, H. Yoshikawa, K. Awaga, M. Murayama, T. Mori, K. Sunada, S. Bandow, S. Iijima, *Preparation, photocatalytic activities, and dye-sensitized solar-cell performance of submicron-scale TiO_2 hollow spheres*, Langmuir 24 547–550 (2008)

[11] B. O'Regan, M, Grätzel, *A low-cost, high-efficiency solar cell based on dye-sensitized colloidal TiO_2 films,* Nature, 253, 737-740 (1991)

[12] F. Habelhames, L. Lamiri, W. Zerguine, B. Nessark, *Improvement of photoelectrochemical and optical characteristics of meh-ppv using titanium dioxide nanoparticles*, Mater. Sci. Semicond. Process, 16, 727-731 (2013)

[13] H. Li, Z. Bian, J. Zhu, D. Zhang, G. Li, Y. Huo, H. Li, Y. Lu, *Mesoporous titania spheres with tunable chamber stucture and enhanced photocatalytic activity*, J. Am. Chem. Soc. 129 8406–8407 (2007).

[14] B. Liu, K. Nakata, M. Sakai, H. Saito, T. Ochiai, T. Murakami, K. Takagi, A. Fujishima, *Mesoporous TiO_2 core shell spheres composed of nanocrystals with exposed high-energy facets: facile synthesis and formation mechanism,* Langmuir 27 8500–8508 (2011)

[15] Z. Zheng, B. Huang, X. Qin, X. Zhang, Y. Dai, *Strategic synthesis of hierarchical TiO_2 microspheres with enhanced photocatalytic activity,* Chem. Eur. J. 16 11266–11270 (2010)

[16] C. Aprile, A. Corma, H. Garcia, *Enhancement of the photocatalytic activity of TiO_2 through spatial structuring and particle size control: From subnanometric to submillimetric length scale,* Phys. Chem. Chem. Phys. 10, 769-783 (2008)

[17] I.-D. Kim, A. Rothschild, B.H. Lee, D.Y. Kim, S.M. Jo, H.L. Tuller, *Ultrasensitive chemiresistors based on electrospun TiO_2 nanofibers*, Nano Letters 6 2009–2013 (2006)

[18] J. Moon, J.-A. Park, S.-J. Lee, T. Zyung, I.-D. Kim, *Pd-doped TiO_2 nanofiber networks for gas sensor applications,* Sens. Actuat. B: Chem. 149 301–305 (2010)

[19] P Roy, D Kim, K Lee, E Spiecker, P Schmuki, *TiO_2 nanotubes and their application in dye-sensitized solar cells,* Nanoscale. Jan;2(1):45-59 (2010)

[20] S.H. Nam, H.-S. Shim, Y.-S. Kim, M.A. Dar, J.G. Kim, W.B. Kim, *Ag or Au nanoparticle-embedded one-dimensional composite TiO_2 nanofibers prepared via electrospinning for use in lithium-ion batteries,* ACS Appl. Mater. Interfaces 2 2046–2052 (2010)

[21] D. Li, Y. Xia, *Fabrication of titania nanofibers by electrospinning,* Nano Lett. 3 555–560 (2003)

[22] A.K. Alves, F.A. Berutti, F.J. Clemens, T. Graule, C.P. Bergmann, *Photocatalytic activity of titania fibers obtained by electrospinning,* Mater. Res. Bull. 44 312–317 (2009)

[23] A. Michailowski, D. AlMawlwai, G.S. Cheng, M. Moskovits, *Highly regular anatase nanotubule arrays fabricated in porous anodic templates* Chem. Phys. Lett. 349 (2001)

[24] T. S. Kang, A. P. Smith, B. E. Taylor, M. F. Durstock, *Fabrication of Highly-Ordered TiO_2 Nanotube Arrays and Their Use in Dye-Sensitized Solar Cells* Nano Lett., 9, 601–606, (2009)

[25] S. Lee, I. S. Cho, J. H. Lee, D. H. Kim, D. W. Kim, J. Y. Kim, H. Shin, J. K. Lee, H. S. Jung, N. G. Park, K. Kim, M.J. Ko, K.S, *Hong Two-Step Sol–Gel Method-Based TiO_2 Nanoparticles with Uniform Morphology and Size for Efficient Photo-Energy Conversion Devices*, Chem. Mater., 22, 1958–1965, (2010)

[26] S. Suzuki, Y. Yoshikawa, *Synthesis and Thermal Analyses of TiO_2-Derived Nanotubes Prepared by the Hydrothermal Method,* J. Mater. Res., 19 (4), 982–985, (2004)

[27] Gong D, Grimes CA, Varghese OK, Hu W, Singh RS, Chen Z, *Titanium oxide nanotube arrays prepared by anodic oxidation*, J Mater Res 16, 3331-4 (2011)

[28] P Roy, S Berger, P. Schmuki, *TiO_2 nanotubes: Synthesis and applications*, Angew. Chem. Int. Ed., 50, 2904-39 (2011)

[29] D. Gong, C.A. Grimes, O.K. Varghese, W. Hu, R.S. Singh, Z. Chen, E.C. Dickey, J. *Titanium oxide nanotube arrays prepared by anodic oxidation*, Mater. Res. 16 3331 (2001)

[30] G.K. Mor, O.K. Varghese, M. Paulose, N. Mukherjee, C.A. Grimes, J. *Mater. Res. Photoelectrochemical properties of titania nanotubes* 18 2588 (2004)

[31] G.K. Mor, K. Shankar, M. Paulose, O.K. Varghese, C.A. Grimes, *Enhanced photocleavage of water using titania nanotube arrays* Nano Lett. 5, 191 (2005)

[32] Q. Cai, M. Paulose, O. Varghese, C. Grimes, *The Effect of Electrolyte Composition on the Fabrication of Self-Organized Titanium Oxide Nanotube Arrays by Anodic Oxidation*, J. of Mat. Res., 20, 1, (2005)

[33] C. Ampelli, R. Passalacqua, S. Perathoner, G. Centi, D.S. Su, G. Weinberg, *Synthesis of TiO_2 Thin Films: Relationship between Preparation Conditions and Nanostructure,* Top. in Cat., 50, 133-144 (2008)

[34] G. K. Mor, O. K. Varghese, M. Paulose, K. Shankar, C. A. Grimes, *A review on highly ordered, vertically oriented TiO_2 nanotube arrays: Fabrication, material properties, and solar energy applications*, Sol. Ener. Mat. & Sol. Cells 90 2011–2075, (2006)

[35] L. Liu, Z. Ji, W. Zou, X. Gu, Y. Deng, F. Gao, C. Tang, L. Dong, *in Situ Loading Transition Metal Oxide Clusters on TiO_2 Nanosheets As Co-catalysts for Exceptional High Photoactivity* ACS Catal., 3, 2052–2061 (2013)

[36] T. Shichi, K.-i. Katsumata, *Development of photocatalytic self-cleaning glasses utilizing metal oxide nanosheets*, Hyomen Gijutsu 61 30–35 (2010)

[37] T. Shibata, N. Sakai, K. Fukuda, Y. Ebina, T. Sasaki, *Photocatalytic properties of titania nanostructured films fabricated from titania nanosheets*, 9, 2413–2420 (2007)

[38] J. Konishi, K. Fujita, K. Nakanishi, K. Hirao, K. Morisato, S. Miyazaki, M. Ohira, *Sol–gel synthesis of macro–mesoporous titania monoliths and their applications to chromatographic separation media for organophosphate compounds*, J. Chromatogr. A 1216, 7375–7383 (2009)

[39] K. Saravanan, K. Ananthanarayanan, P. Balaya, *Mesoporous TiO_2 with highpacking density for superior lithium storage*, Energy Environ. Sci., 3, 939-48, (2010)

[40] N. Murakami, T. Chiyoya, T. Tsubota, T. Ohno, *Switching redox site of photocatalytic reaction on titanium(IV) oxide particles modified with transition-metal ion controlled by irradiation wavelength,* App. Cat. A 348 (2008)

[41] J. Zhu, F. Chen, J. Zhang, H. Chen, M. Anpo, *Fe3+-TiO2 photocatalysts prepared by combining sol–gel method with hydrothermal treatment and their characterization*, J. of Photochem. and Photobio., A 180, 196–204 (2006)

[42] M. Kang, *The superhydrophilicity of Al–TiO2 nanometer sized material synthesized using a solvothermal method* Mat. Lett. 59, 3122–3127 (2005)

[43] K. Demeestre, J. Dewulf, T. Ohno, P.H. Salgado, H.V. Langenhove, *Visible light mediated photocatalytic degradation of gaseous trichloroethylene and dimethyl sulfide on modified titanium dioxide* App. Cat. B: Environmental 61, 140–149 (2005)

[44] K. Iketani, R.-D. Sun, M. Toki, K. Hirota, O. Yamaguchi, *Sol–gel-derived VχTi1−χO2 films and their photocatalytic activities under visible light irradiation* Mat. Sci. and Engin. B, 108, 187–193 (2004)

[45] K. Demeestre, J. Dewulf, T. Ohno, P.H. Salgado, H.V. Langenhove, *Visible light mediated photocatalytic degradation of gaseous trichloroethylene and dimethyl sulfide on modified titanium dioxide* App. Cat. B: Environmental 61, 140–149, (2004)

[46] F. Tavella, C. Ampelli, L. Frusteri, F. Frusteri, , S. Perathoner, , G. Centi, *Development of photoanodes for photoelectrocatalytic solar cells based on copper-based nanoparticles on titania thin films of vertically aligned nanotubes* Cat. Tod., 304, 190-198 (2018)

[47] C. Ampelli, F. Tavella, C. Genovese, S. Perathoner, M. Favaro, G. Centi, *Analysis of the factors controlling performances of Au-modified TiO_2 nanotube array based photoanode in photo-electrocatalytic (PECa) cells*, J. of Ener. Chem., 26, 284-294 (2017)

[48] X. You, F. Chen, J. Zhang, M. Anpo, *A novel deposition precipitation method for preparation of Ag-loaded titanium dioxide* Catal. Lett. 102, 247–250 (2005)

[49] S. Peiris, J. McMurtrie, H.Y. Zhu, *Metal nanoparticle photocatalysts: emerging processes for green organic synthesis* Catal. Sci. Technol., 6, 320–338 (2016)

[50] A. Fujishima, X. Zhang, D.A. Tryk, *TiO_2 photocatalysis and related surface phenomena* Surf. Sci. Rep. 63 515–582 (2008)

[51] A. Fujishima, X. Zhang, D.A. Tryk, *TiO_2 photocatalysis and related surface phenomena* Surf. Sci. Rep. 63, 515–582 (2008)

[52] R. Asahi, T. Morikawa, T. Ohwaki, K. Aoki, Y. Taga, *Visible-light photocatalysis in nitrogen-doped titanium oxides* Science 293, 269–271 (2001)

[53] S.-Z. Chen, P.-Y. Zhang, D.-M. Zhuang, W.-P. Zhu, *Investigation of nitrogen doped TiO_2 photocatalytic films prepared by reactive magnetron sputtering*, Catal. Comm., 5, 11, 677-680 (2004)

[54] M. & M. Batzill, E. & D., Ulrike, *Surface studies of nitrogen implanted TiO_2* Chem. Phys. 339, 36-43 (2007)

[55] C. Sarantopoulos, A.N. Gleizes, F. Maury, *Chemical vapor deposition and characterization of nitrogen doped TiO_2 thin films on glass substrates* Thin Solid Films 518, 1299–1303 (2009)

[56] Y. Zhang, M. Creatore, Q.-B. Ma, A. El Boukili, L. Gao, M. A. Verheijen, M.W.G.M. (Tiny) Verhoeven, E. J.M. Hensen, *Nitrogen-doping of bulk and nanotubular TiO_2 photocatalysts by plasma-assisted atomic layer deposition*, App. Surf. Sci., 330, 476-486, (2015)

[57] Y. Zhang, M. Creatore, Q.-B. Ma, A. El Boukili, L. Gao, M. A. Verheijen, M.W.G.M. (Tiny) Verhoeven, E. J.M. Hensen, *Nitrogen-doping of bulk and nanotubular TiO_2 photocatalysts by plasma-assisted atomic layer deposition*, App. Surf. Sci., 330, 476-486, (2015)

[58] A.M. Czoska, S. Livraghi, M. Chiesa, E. Giamello, S. Agnoli, G. Granozzi, E. Finazzi, C. Di Valentin, G. Pacchioni, *The Nature of Defects in Fluorine-Doped TiO_2* J. of Phys. Chem. C 112, 8951–8956 (2008)

[59] B. Malini, G. Allen Gnana Raj, *C, N and S- doped TiO_2-Characterization and Photocatalytic performance for dye degradation under day light*, J. of Envir. Chem. Engineer., (2018)

[60] M. Favaro, S. Leonardi, C. Valero-Vidal, S. Nappini, M. Hanzlik, S. Agnoli, J. Kunze-Liebhäuser, G. Granozzi, *In-Situ Carbon Doping of TiO_2 Nanotubes Via Anodization in Graphene Oxide Quantum Dot Containing Electrolyte and Carburization to TiO x C y Nanotubes* Adv. Mater. Interfaces, 2, 1400462 (2015)

[61] C. Han, M. Pelaez, V. Likodimos, A.G. Kontos, P. Falaras, K. O'Shea, D.D. Dionysiou, *Innovative visible light-activated sulfur doped TiO_2 films for water treatment* App. Cat. B: Envir. 107, 77–87 (2011)

[62] S. Cravanzola, F. Cesano, F. Gaziano, D. Scarano, *Sulfur-Doped TiO_2: Structure and Surface Properties* Catalysts, 7(7), 214 (2017)

[63] B. O'Regan, M. Gratzel, *A low-cost, high-efficiency solar cell based on dye-sensitized colloidal TiO_2 films* Nature 353 737–739 (1991)

[64] D. Chatterjee, S. Dasgupta, N.N. Rao, *Visible light assisted photodegradation of halocarbons on the dye modified TiO_2 surface using visible light,* Sol. Ener. Mater. and Sol. Cells 90, 1013 (2006)

[65] W. J. Chun, A. Ishikawa, H. Fujisawa, T. Takata, J. N. Kondo, M. Hara, M. Kawai, Y. Matsumoto and K. Domen, *Conduction and Valence Band Positions of Ta_2O_5, TaON, and Ta_3N_5 by UPS and Electrochemical Methods* J. Phys. Chem. B, 107, 1798 (2003)

[66] J. Y. Duan, W. D. Shi, L. L. Xu, G. Y. Mou, Q. L. Xin and J. G. Guan, *Single crystalline tantalum oxychloride microcubes: controllable synthesis, formation mechanism and enhanced photocatalytic hydrogen production activity* Chem. Commun., 48, 7301 (2012)

[67] Y. B. Li, T. Takata, D. Cha, K. Takanabe, T. Minegishi, J. Kubota and K. Domen, *Vertically aligned Ta_3N_5 nanorod arrays for solar-driven photoelectrochemical water splitting* Adv. Mater., 25, 125 (2013)

[68] C. Chaneliere, J. L. Autran, R. A. B. Devine and B. Balland, *Conduction mechanisms in $Ta_2O_5/SiO_2$and Ta_2O_5/Si_3N_4 stacked structures on Si* Mater. Sci. Eng., R, 22, 269–322 (1998)

[69] I. Sieber, B. Kannan and P. Schmuki, *Self-Assembled Porous Tantalum Oxide Prepared in H_2SO_4 /HF Electrolytes* Solid-State Lett., 8(3), 10–12 (2005)

[70] L. Wang, N. T. Nguyen, X. Zhou, I. Hwang, M. S. Killian, P. Schmuki; *Enhanced Charge Transport in Tantalum Nitride Nanotube Photoanodes for Solar Water Splitting* ChemSusChem, 8, 2615–2620 (2015)

[71] L. Wang, F. Dionigi, N. T. Nguyen, R. Kirchgeorg, M. Gliech, S. Grigorescu, P. Strasser, P. Schmuki, *Tantalum Nitride Nanorod Arrays: Introducing Ni–Fe Layered Double Hydroxides as a Cocatalyst Strongly Stabilizing Photoanodes in Water Splitting* Chem. Mater., 27, 2360–2366 (2015)

[72] S. Grigorescu, S. So, J. E. Yoo, A. Mazare, R. Hahn, P. Schmuki, *Open top anodic Ta_3N_5 nanotubes for higher solar water splitting efficiency,* Electrochimica Acta, 182, (2015)

[73] C. Ampelli, R. Passalacqua, S. Perathoner, G. Centi *Electrolyte-less design of PEC cells for solar fuels: Prospects and open issues in the development of cells and related catalytic electrodes* Cat. Tod. 259, 246–258 (2016)

[74] C. Ampelli, C. Genovese, R. Passalacqua, S. Perathoner, G. *Centi. A gas-phase reactor powered by solar energy and ethanol for H_2 production,* App. Ther. Engineer., 70, 2, 1270-1275 (2014)

[75] S. Bensaid, G. Centi, E. Garrone, S. Perathoner, G. Saracco, *Towards artificial leaves for solar hydrogen and fuels from carbon dioxide* ChemSusChem, 5, 500 (2012)

[76] S. Perathoner, G. Centi, *CO_2 Recycling: A Key Strategy to Introduce Green Energy in the Chemical Production Chain* ChemSusChem 7, 1274 (2014)

[77] S.Y. Reece, J.A. Hamel, K. Sung, T.D. Jarvi, A.J. Esswein, J.J.H. Pijpers, D.G. Nocera, *Wireless Solar Water Splitting Using Silicon-Based Semiconductors and Earth-Abundant Catalysts* Science 334, 645 (2011)

[78] D.G. Nocera, *The artificial leaf* Acc. Chem. Res. 45, 767 (2012)

[79] C. Ampelli, F. Tavella, S. Perathoner, G. Centi *Engineering of photoanodes based on ordered TiO_2-nanotube arrays in solar photo-electrocatalytic (PECa) cells*, Chem. Engineer. J. 320, 352–362 (2017)

3 TiO_2 nanotube arrays in water photo-electrolysis

3.1 State of the art

The efficient utilization of solar energy is one of the major goals of modern science and engineering, with reference to the issues of global warming and fossil fuel depletion. In this context, the photo-electrochemical (PEC) approach is an attractive technology to produce solar hydrogen from water and sunlight.

Since the discovery of photocatalytic water splitting on TiO_2 by Fujishima and Honda in 1972 [1], the development of semiconductor photo-catalysts has grown for a wide range of environmental and energy applications. However, TiO_2 is still the most studied material for its well-known characteristics, as widely discussed in Chapter 2. Many review articles have reported recent advances on TiO_2 photo-catalysts, [2-3] and specifically on the possibility to create a nano-architecture in TiO_2 (such as nanotubes, nanorods, nanopillars, nanocoils), which improves their photo-catalytic proprieties by limiting charge recombination. Grimes and co-workers [4] first reported the formation of uniform titania nanotube arrays via anodic oxidation of titanium in a hydrofluoric (HF) electrolyte; since then many researchers have investigated in detail the formation of TiO_2 nanotubes, focusing on the relationship between synthetic parameters and structural properties [5-7].

3.2 The scope of the chapter

This thesis work focuses on the synthesis of highly ordered titania nanotube arrays to be used as photoanodes in the photo-electrochemical production of H_2. Particularly, the main purpose of this chapter is to describe the experimental synthesis of TiO_2 nanotube arrays grown on a Ti foil, as well as their full characterization and testing in a home-made photo-catalytic reactor designed on purpose to separate photoanode and electrocathode [8-10].

A great attention has been given to the study of the influence of the thickness of these TiO_2 nanotube arrays, as the fabrication of thin layers may contribute to limit charge recombination phenomena. The thickness of TiO_2 nanotube arrays on Ti foil represents the length of the nanotubes, which can be modulated by adjusting some synthesis parameters, especially the time of anodization.

Specifically, TiO_2 nanotube (TNT) thin films were fabricated by controlled anodic oxidation of Ti foils at different anodization times (from 30 min to 5 h), to generate different thicknesses of photo-active layers, and then tested in a compact photo-electrocatalytic (PECa) device for H_2 generation by water photo-electrolysis (as described in the experimental section). The vertically aligned TNT films differ only for the film thickness, but they show: 1) similar nanotube diameter, 2) uniform thickness and clean top surface and 3) same crystallinity degree in anatase phase [11].

In order to understand better the performances of the whole set-up (TNTs + PECa), different kinds of efficiency have been calculated: 1) the photoconversion efficiency, also called solar-to-hydrogen efficiency (STH), which takes into account the amount of energy supplied in terms of light and the products obtained (i.e. hydrogen); 2) Faradaic efficiency, which relates the photo-generated current to the produced hydrogen; 3) the quantum efficiency, expressed as IPCE (incident photon to current efficiency) and APCE (absorbed photon to current efficiency).

At the end of the chapter, a brief paragraph illustrates the results obtained through a collaboration with the university of Lyon in the preparation of 3D architecture TiO_2 nanotubes on Ti grid [12]. In these latter samples, the main aim was to create a hierarchical structure (i.e. macropores of the Ti mesh and mesopores of TiO_2 nanotube arrays) to improve the mass and charge transport within the electrochemical cell.

3.3 Experimental

3.3.1 Synthesis by controlled anodic oxidation

The nano-structured TiO_2 (TNT) thin films were prepared by anodic oxidation technique. The method, as described in Chapter 2, consists of the controlled oxidation of a Ti layer under the application of a constant voltage in a F-based electrolyte [13]. The substrate was a metallic titanium disk (35 mm diameter Alfa Aesar) with a thickness of 0.025 mm and a purity of 99.96%. Before performing the anodization, the titanium discs were ultrasonically cleaned with isopropyl alcohol for 30 min at a temperature of 50 °C and subsequently dried in air. The Ti discs were put in a home-made sample holder (Figure 3.1a) and immersed in the reaction bath consisted of a solution of ethylene glycol with H_2O (2 wt%) and NaF (0.3 wt%). The set voltage

was gradually reached by a programmed ramp at 3 V min^{-1} using an Agilent E3612A DC Power Supply and then kept constant for the whole anodization. This procedure was optimized to obtain a robust TNT layer. The thickness and morphology of TNTs are strongly dependent on the sweep rate of the first stage of the treatment, and normally the oxide is the thickest for optimized sweep rates [14]. Figure 3.1b shows the entire set-up for anodization experiments consisting of a power supply, a sample holder and a Teflon cell.

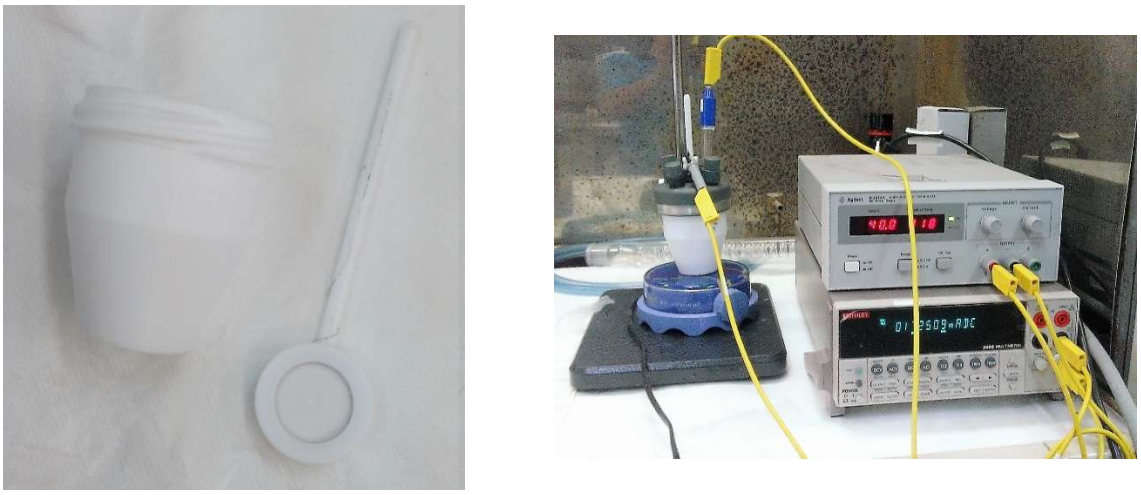

a ***b***

Figure 3.1: a) home-made support for holding Ti disk b) the entire set-up used for anodization of Ti with the electrochemical cell connected to the power supply and amperometer for data recording.

After the preparation, the nanostructured amorphous substrates were annealed at 450 °C in air for 3 h in order to induce crystallization into the anatase phase. The non-oxidized Ti layer, remaining after the anodization, will act as an electron-collective layer once assembled in the PEC cell. Table 3.1 shows the list of the different samples prepared: anodization time was increased from 30 min to 5 h:

Sample name	Anodization time	Voltage	Ramp
MR30	30 min	50	3V/min
MR45	45 min	50	3V/min
MR1	1 h	50	3V/min
MR3	3 h	50	3V/min
MR5	5 h	50	3V/min

Table 3.1: List of anodized Ti for different times.

3.3.2 Characterization

Scanning Electron Microscopy (Phenom ProX Desktop) was used for structural and morphological characterization of the TNT materials, operating at an accelerating voltage of 5 kV. The nanotube diameter and length were directly measured from SEM images.

After a strong sonication treatment to detach the oxide from the Ti layer, the TNTs were analysed by N_2 adsorption/desorption (Brunauer-Emmett-Teller - BET) at 77 K using an ASAS 2020 Micromeritics system. To degas the samples, a pre-treatment was performed at 10 Pa and 150 °C for 2 h.

Ultraviolet-visible diffuse reflectance measurements were performed by a Jasco V570 spectrometer equipped with an integrating sphere for solid samples, using $BaSO_4$ as the reference and in air.

A home-made set-up (Figure 3.2) was used for chrono-amperometry measurements. The device consists of a three electrode photo-electrochemical cell, with a Pt wire as the counter-electrode and a saturated KCl-Ag/AgCl as the reference electrode. All the tests were performed at room temperature in 1 M KOH solution at 0.1 V using a 2049 AMEL potentiostat-galvanostat.

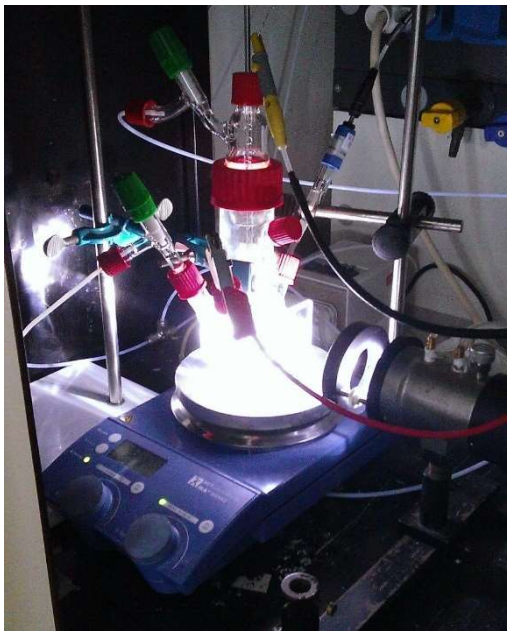

Figure 3.2: Experimental apparatus for chrono-amperometric measurements.

The phase composition and the degree of crystallinity were analysed by X-ray diffraction (XRD) analysis with an ADP 2000 diffractometer using a Cu-Ka radiation. Data was collected at

a scanning rate of 0.025 s in a 2 h range from 15° to 90°. Diffraction peak identification was made on the basis of the JCPDS database of reference compounds.

3.3.3 Testing

Figure 3.3 shows the block diagram of experimental set-up used for water splitting tests.

A light source (Xe-arc lamp Lot Oriel, 300 W) irradiates the photo-device (PECa). The lamp is equipped with a set of lenses for light collection and focusing, a water filter to eliminate the infrared radiation and a set of filters to select the desired wavelength region for evaluating the photo-response in ultraviolet or visible regions (figure 3.4). The current measurements were performed by a potentiostat/galvanostat (AMEL 2049), while the gas products were quantified by a chromatograph (Agilent 7890a).

The homemade PECa device is made of Plexiglas and equipped with a quartz window. It has a two-electrode configuration with two separate compartments for the reduction/oxidation half-reactions. 1 M NaOH aqueous solution was used as electrolyte in the anodic compartment, while 0.5 M H_2SO_4 aqueous solution was used in the cathodic side.

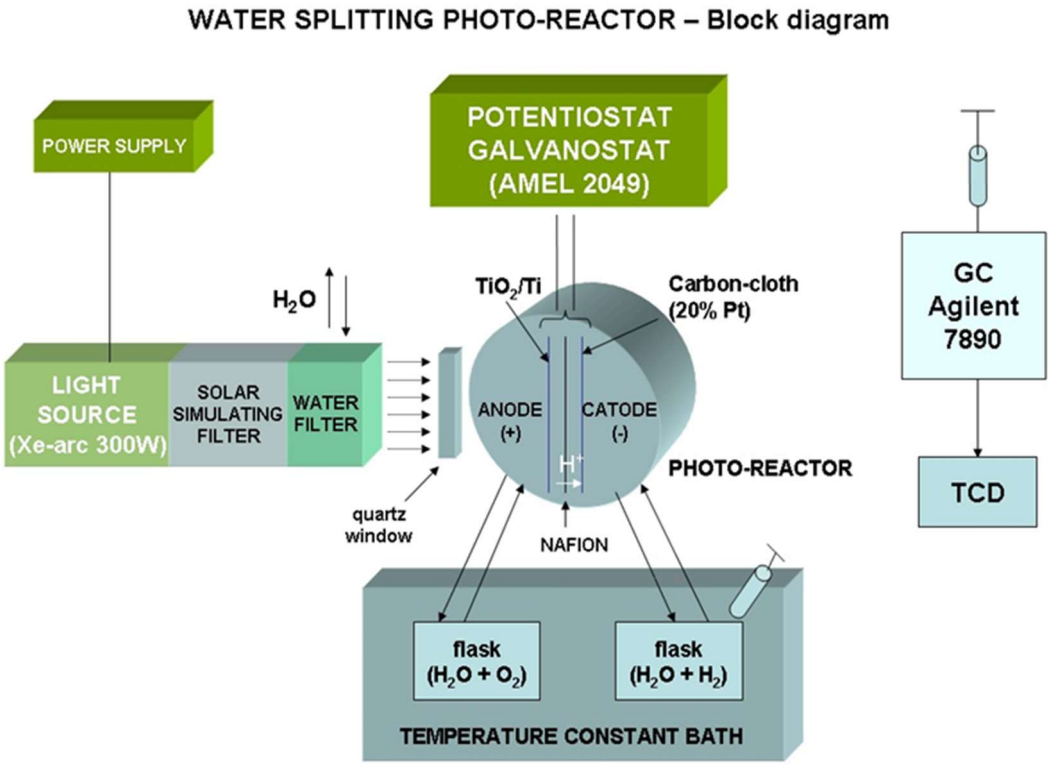

Figure3.3: Water splitting apparatus block diagram. Reproduced with permission from ref. [15].

Filters for full spectrum solar simulator	
LSZ185	Air mass 0 (outer space)
LSZ389	Air mass 1.5 global, (direct and diffuse) through atmosphere, 48°
Filters for UV solar simulator	
LSZ176	Atmospheric edge filter, 290 - 4400 nm
LSZ177	VIS-IR blocking filter, 290 - 400 nm, 650 - 800 nm
LSZ178	UVC blocking filter, 280 - 4400 nm
LSZ179	UVB/C blocking filter, 320 - 480 nm, 700 - 4400 nm

Figure3.4: List of light-cutting filters provided from Lot Oriel.

The core of the device is a MEA (membrane electrode assembly) consisting of three layers assembled together by hot-pressing technique. The anode (the catalyst based on titanium nanotubes) is the photo-active material responsible for light capture and for the generation of the electron-hole pair. The non-anodized Ti layer plays a very important role as it is responsible for the capture of the electrons that are generated on the surface of the tubes, strongly limiting their charge recombination with holes.

In the cathode (i.e. a commercial carbon gas diffusion layer –GDL- with a loading of 0.5 mg cm^{-2} of platinum, GDE S10BC SIGRACET®), the protons arriving from the anode can recombine with the electrons coming from an external contact (Pt wire) to produce hydrogen. A Pt ring is also used to improve the conductivity of the carbon GDL.

In the middle between anode and cathode layers, a Nafion membrane was used as a selective medium allowing only for the protons to reach the cathode.

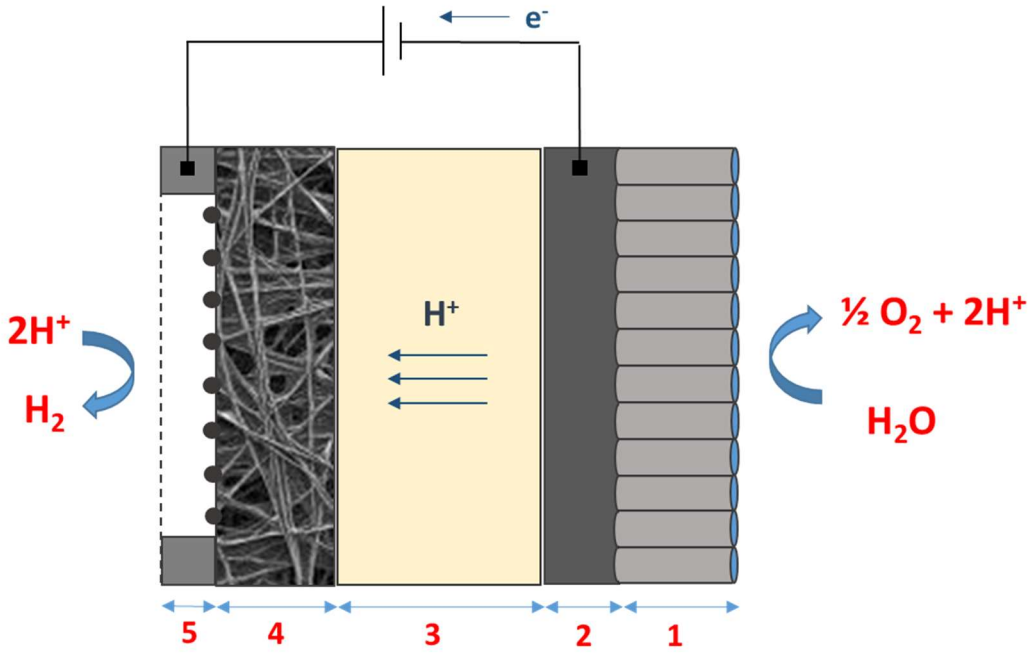

Figure 3.5: scheme of the membrane electrode assembly (MEA). Adapted from ref. [11].

Figure 3.5 shows the schematic cross section of the PECa cell. In brief, the working principle is the following: light irradiation actives the TiO_2 nanotube arrays (1) with the generation of an electron-hole pair; the holes oxidize the water to O_2; while the electrons are collected from the metallic Ti layer (2) and flow to the external circuit; the protons migrate through the Nafion membrane (3), reach the cathode (4) and recombine with the electrons (onto Pt active sites) coming from the external circuit to produce H_2. To allow the migrations of protons through the compact Ti layer, some small holes (with a diameter of about 0.1 mm) were created into TNTs/Ti disk after the anodization.

3.3.4 Efficiency

Literature reports several approaches to calculate the overall photo-conversion efficiency [16]. The main parameter that considers the entire process is the solar-to-hydrogen (STH) efficiency. The STH efficiency is given by the ratio between the hydrogen (or oxygen) produced and the energy supplied (total light irradiance P_{tot}). For the experimental tests performed in the PECa cell over the TNT electrodes, the STH efficiency was calculated by the formula:

$$STH \frac{R_{H2} * \Delta G^0}{Ptot * A} \quad (3.1)$$

where R_{H2} is the rate of hydrogen production (mol s^{-1}), ΔG^0 is the standard Gibbs energy at standard conditions (2.372 10 J mol^{-1}), P_{tot} is the light irradiance (W cm^2) and A is the irradiated area of the photocatalyst (cm^2). If an external bias is applied between the two electrodes, the photo-conversion efficiency can also be indicated as applied bias photon-to-current efficiency (ABPE) and it can be calculated by using the following equation:

$$ABPE\ \frac{R_{H2} * (\Delta G^0 - V_{bias}\, nF\,)}{Ptot * A} \tag{3.2}$$

where V_{bias} is the applied voltage, n is the number of moles of electrons used for generating 1 mol of H_2, and F is the Faradaic constant (96,485 C mol^{-1}). If V_{bias} is 0, Eq. (3.2) equals Eq. (3.1) and ABPE coincides with STH efficiency.

Another useful parameter is the Faradaic efficiency (η) that is the ratio between the real and theoretical H_2 (or O_2) produced (eq. 3.3 and 3.4):

$$\eta(\%) = \frac{H_2^{meas}}{H_2^{theor}} \tag{3.3}$$

$$H_2^{theor} = \frac{I * t}{nF} \tag{3.4}$$

The theoretical H_2 production is defined by the photocurrent I generated during the time t divided by the number n of electrons involved in water splitting, and F is the Faradaic constant.

To calculate the efficiency values of TNTs, it is necessary to measure the light irradiance (i.e. the amount of light reaching the photo-active materials) and quantify the percentage of absorbed light with respect to the incident light. To obtain this information, it was necessary to remove the layers of nanotubes of different thickness from the respective Ti metal supports. With a short anodization (about 15 minutes) and a subsequent sonication treatment of a few seconds, it was possible to separate the titanium oxide nanotube membrane from the metal remained not-oxidized after the anodization. The layers thus obtained were subsequently placed in a support specifically designed to fit with the PEC cell. In order to measure the light irradiance, an optical fiber was placed behind the TNT layer and connected to a

spectroradiometer (Lot Oriel, model ILT950), while a monochromator (MSH-150, Lot Oriel) was used to select the individual wavelength coming from the lamp, with a wavelength reproducibility of ±0.05 nm. By setting the slit width at 2 mm, a bandwidth of 5.4 nm was obtained. Figure 3.6 shows the set-up used for the determination of light irradiance. It should be noted that these measurements were carried out under conditions very close to those used for the experimental photo-catalytic tests for H_2 production.

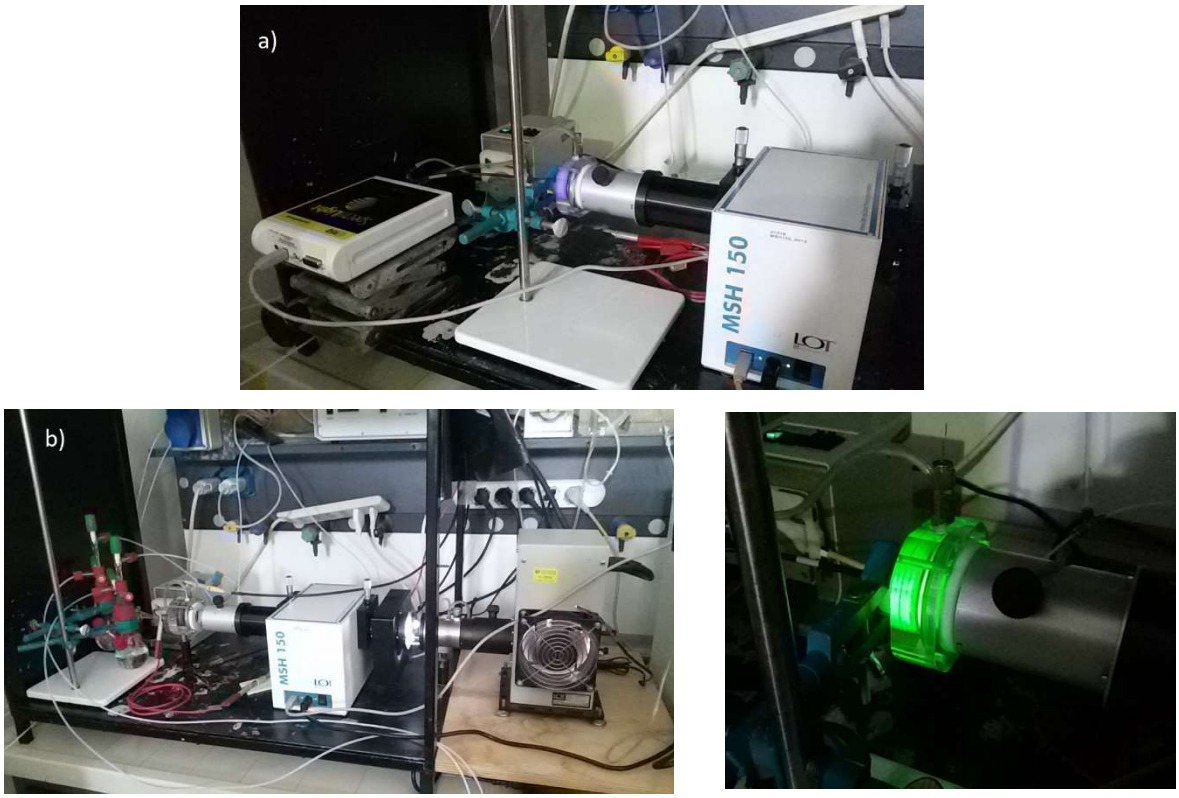

Figure 3.6: a) Spectroradiometer measurements b) Current density measurements under single wavelength.

3.4 Result and discussion

3.4.1 Characteristic of titania nanotubes array (TNT)

Anodization technique allows the modulation of the nano-architecture of the TNT layer; changing every single parameter results in a change in the morphology of the tubes. This chapter focuses on the study of the length of the nanotubes, which depends mainly on the anodization time. In the adopted experimental conditions, the length of the TiO_2 nanotube was

investigated up to 5 h anodization time. For longer times, an equilibrium between the dissolution of the oxide (from the top of the nanotubes) and further growth of the tubes (from the bottom of the nanotubes near the metallic Ti layer) was reached, and the length remained quite constant.

The nanotube formation process begins with the initial rapid increase of the current, due to the initial ramp voltage, reaching a maximum value of 4.7 mA cm^{-2} at 11 min (see Figure 3.7). Referring to the above discussed mechanism of TNT formation (Chapter 2), in this step the barrier oxide layer formation and the subsequently pore nucleation occur. As the oxide has a higher electrical resistance with respect to the starting metallic layer, the growth of the nanotubes results in a decrease of the anodization current (see the graph after 11 min).

Figure 3.8a shows the top view SEM images of TNTs produced at 50 V in 5 h. After the preparation, the surface of the photoactive layer was covered by amorphous oxide, which greatly limits the photo-response. The debris can be removed by a short etching (30 s) with concentrated HCl (37%) in an ultrasonic bath (Elmasonic S30H, 80 W). Figure 3.8b shows the clean TNT surface after the sonication treatment, which is of fundamental importance to enhance light harvesting and photocatalytic activity.

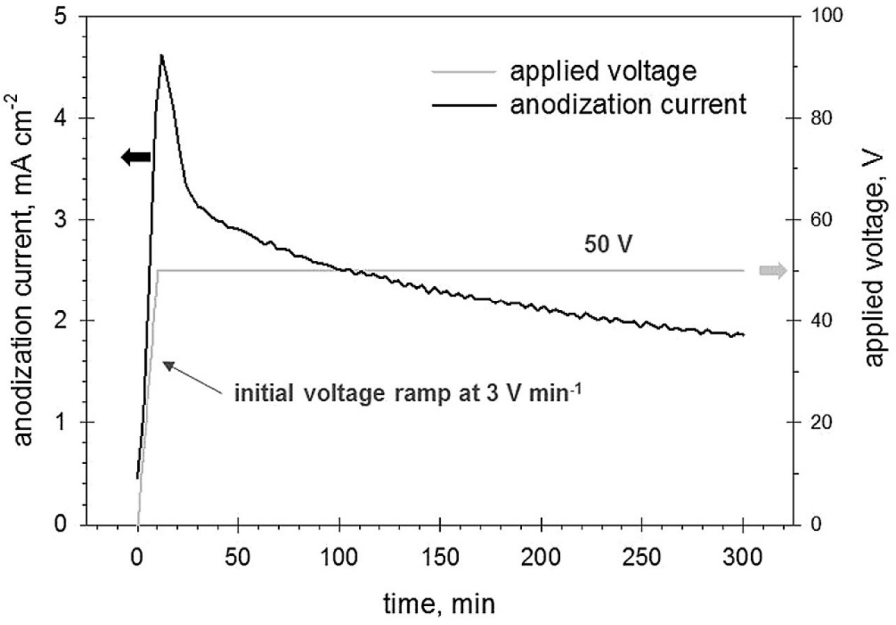

Figure 3.7: Anodization current and applied voltage as a function of time obtained during the synthesis of TNTs at 50 V in 5 h.

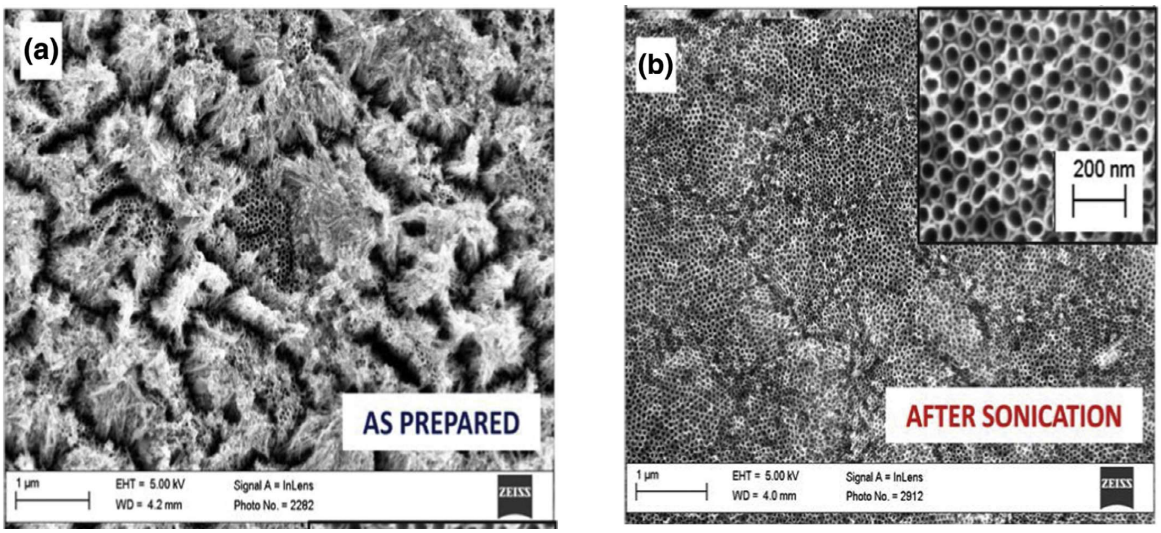

Figure 3.8: SEM top images of (a) the as-prepared TiO_2 nanotube arrays anodized at 50 V and (b) the same nanotubes after sonication treatment. The inset shows a magnification of the cleaned top surface.

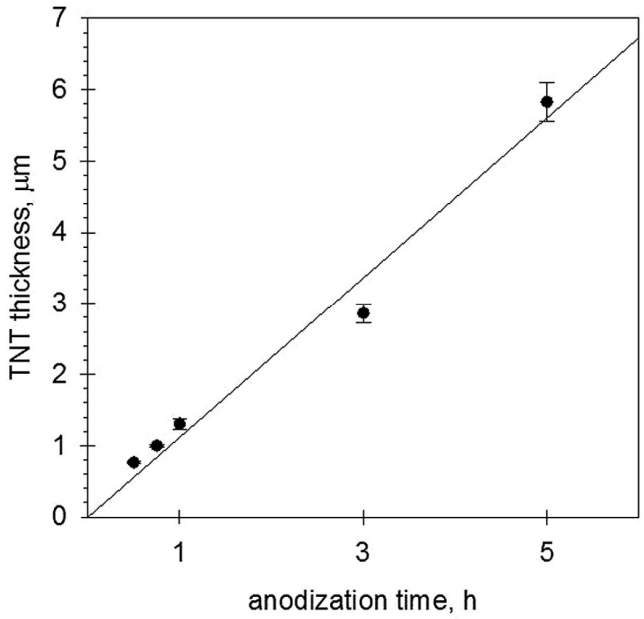

Figure 3.9: TNTs thickness vs. anodization time for TNTs samples anodized for different times.

The relationship between TNT thickness and anodization time is quite linear (Figure 3.9). The nanotubes presented a mean diameter of 54 nm and a thickness of the walls of about 8–9 nm (Figures 3.10e-f). Only the sample anodized for 30 min showed a tube length of about 0.8 µm, but the nanotubes were not properly developed due to the low anodization time. SEM images (Figure 3.10) show an increase of the nanotube length from about 1 µm for the sample anodized for 45 min to about 6 µm for the sample anodized for 5 h.

The error bars in figure 3.9 indicate the standard deviation values, estimated by determining the thickness (by SEM) at different points (>10) of the samples.

Moreover, the TNTs anodized for 5 h were completely removed from the Ti layer by strong sonication and analysed by BET to evaluate the surface area, which resulted to be slightly higher than the common standard TiO_2 Degussa P25 (68 vs. 48 $m^2 g^{-1}$).

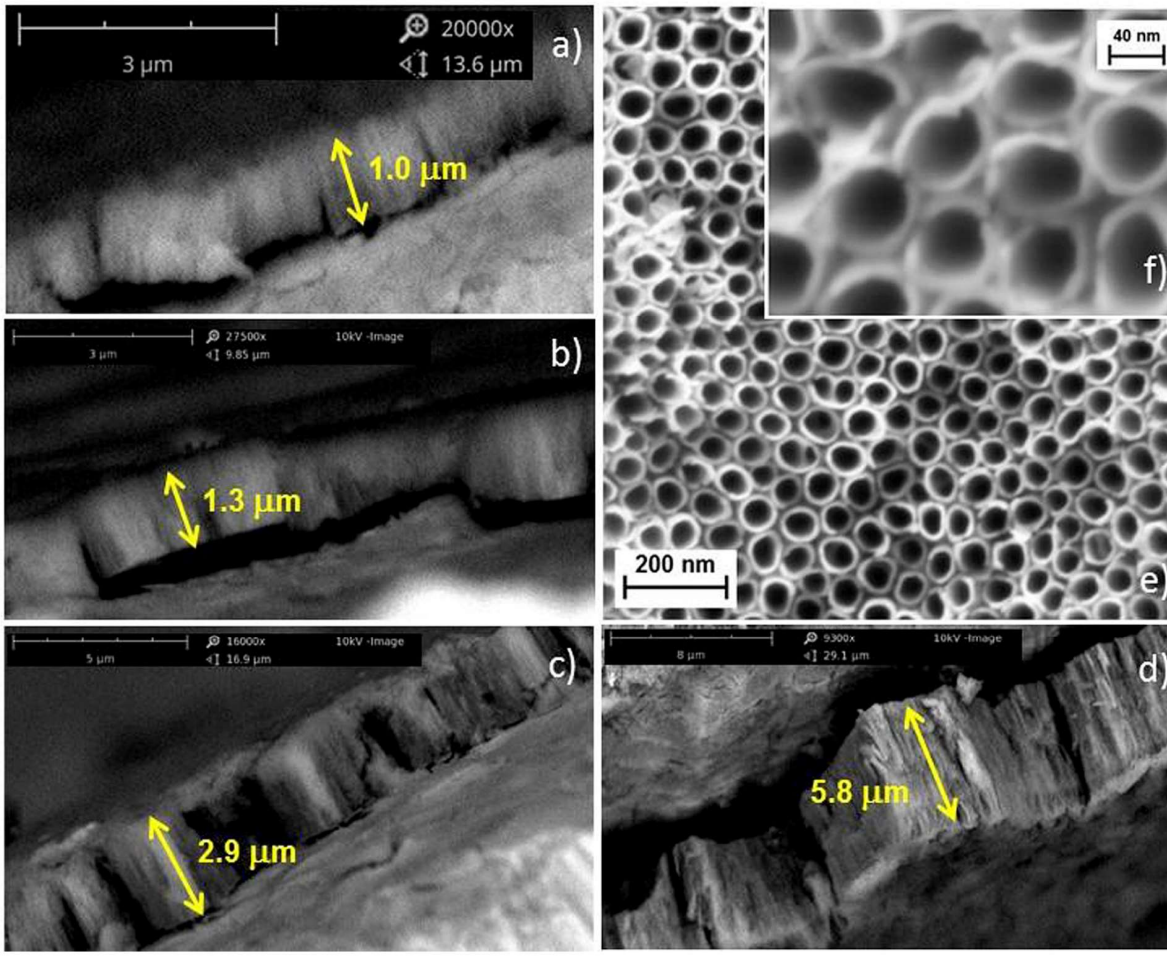

Figure 3.10: SEM images of the cross-section of TNTs/Ti samples produced at 50 V in a) 45 min, b) 1 h, c) 3 h and d) 5 h; e) top view of TNTs produced in 5 h; f) magnification of image in e).

After the anodization, the TNTs are in amorphous form but they become crystalline after the thermal annealing. Crystalline structure was investigated by XRD (Figure 3.11). Anatase structure of titania is present for all the samples, and no rutile phase or other titania phases were detected. To better evidence the peaks related to anatase (A) TiO_2 from those related to the Ti substrate, the Ti XRD pattern has also been reported. The higher the anodization time, the more the intensity of anatase phase is, as expected from the increase of the film thickness,

but there is no change in the half-width broadening of the diffraction peaks, indicating that there is no change in the crystallinity characteristics of the titania film by increasing the film thickness. It is to notice that the attenuation length of the x-rays in the TNT structure (considering a void percentage of 50% with respect to anatase bulk TiO_2) can be estimated as about 1600 µm for a probe of 30 kV. This penetration length is considerably higher than the highest thickness of our TNTs samples (5.8 µm for TNTs anodized in 5 h).

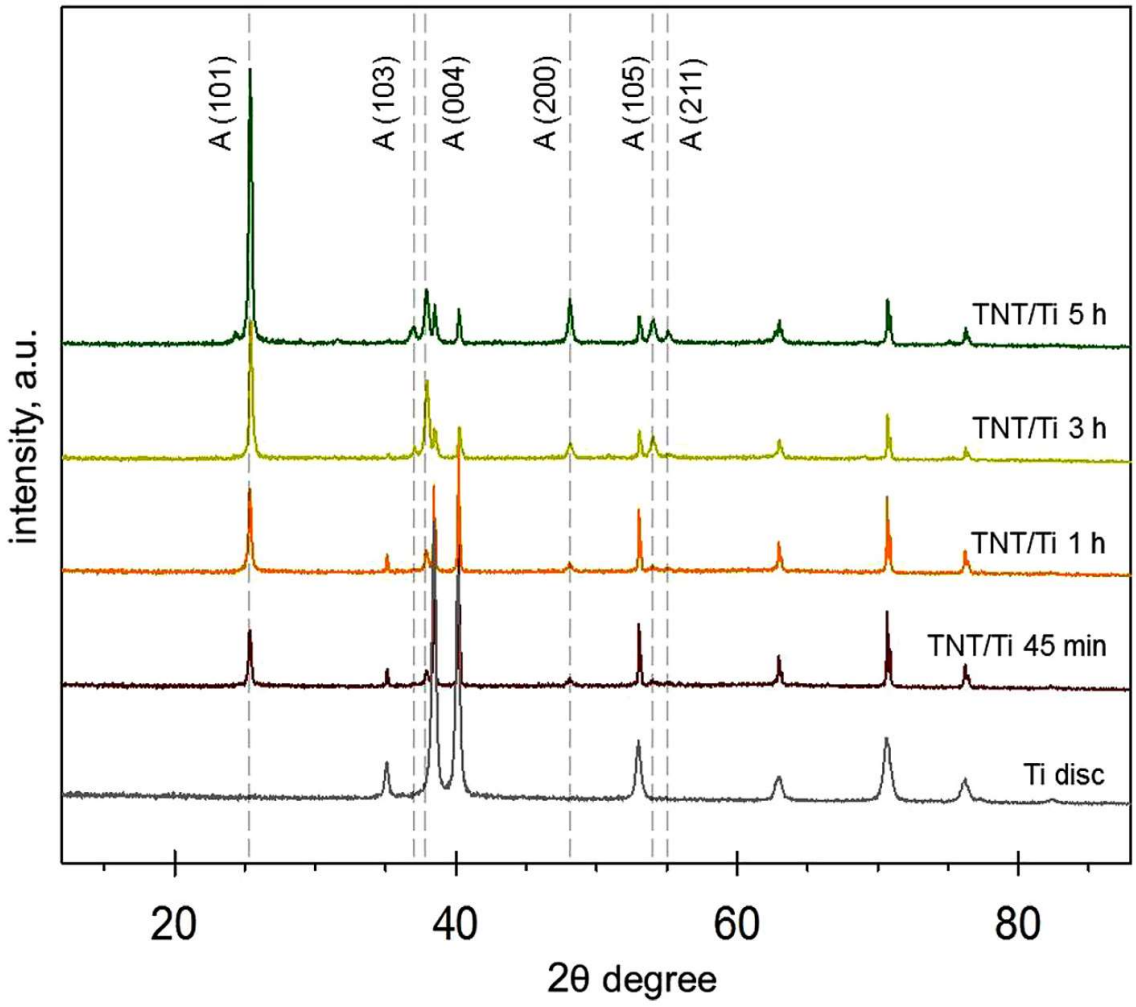

Figure 3.11: XRD patterns of i) TNTs/Ti samples (prepared at different anodization times) and ii) pure Ti disc (99.96%).

3.4.2 Light absorbance characteristics

The spectroradiometer was used to determine the light collection characteristics of the TNTs. The optical fiber was placed inside the PECa cell, instead of the photoactive material, to reproduce the reaction conditions as best as possible. The measured irradiation was 135 mW

cm^{-2}, which represents the incident light energy that reaches the TNT-based electrode when irradiated by the Xe lamp. As already described above (paragraph 3.3.4), by means of a double anodization it was possible to detach the TNT layer from the metal support, and then the resulting membrane was placed inside the PECa cell, in front of the probe, in order to evaluate the actual light transmittance of the individual layers.

All the samples show the almost completely absorbance in the UV part of the irradiated light, because the transmittance was less than 1.5% until 360 nm (Figure 12a). For wavelengths less than 300 nm, all the curves increase, especially from 280 to 250 nm, while a difference was observed in the visible part (>350 nm), where the fraction of light passing through the titania film decreased by increasing the time of anodization (and the film thickness). For example, the 1.3 µm TNTs film (obtained in 1 h) was able to absorb fully the light up with wavelength below 350 nm (UV component and where the titania band gap is located), but only about 70% of the incident light (on average) for wavelength >350 nm (visible light). Table 3.2 reports the total amount of energy absorbed P_{tot} (not transmitted) by the different photoactive layers, expressed in irradiance units (W cm^{-2}), evidencing the increase of total light absorption with the TNT thickness. P_{tot} values were then used to calculate the STH efficiency, as reported below. Figure 3.12a also indicates that an absorption in the visible region exists, although weaker than that in the UV region, while in principle TiO_2 anatase should not have absorption in the visible region. For this reason, the samples were also characterized by UV-visible diffuse reflectance spectroscopy (Figure 3.12b). The spectrum of the commercial TiO_2 P25 Degussa has also been reported for reference. All the spectra exhibit a strong absorption band centered at about 300–350 nm related to the lowest energy charge transfer $O^{2-} \rightarrow Ti^{4+}$ and associated to the TiO_2 band gap (calculated as 2.9–3.0 eV) [17]. As the band gap of anatase TiO_2 is usually reported as 3.2 eV, these results suggest the presence of oxygen vacancies especially on the surface of TNTs. Except for TiO_2 P25 Degussa, all the spectra also evidence a broad absorption peak centered around 580– 610 nm, with a broad tail on the low energy side extending to the whole visible region. This absorption band is not present in films of TiO_2 prepared by sol-gel or by depositing commercial TiO_2 nanoparticles (such as P25). Photonic crystals are periodic dielectric structures that result in a Photonic Band Gap (PBG), which is the optical analogue to the electronic band gap in semiconductors. It is a range of wavelengths that are prohibited from propagating in the crystal because of the dielectric contrast. The existence and width of the photonic band gap are dependent on the crystal structure, refractive index contrast, and filling fraction of the high

index material. The high index material must also be non-absorbing in the wavelength region of interest. Titania is one of the few high index materials that have low absorption in the visible regime and it is suitable for creating photonic crystal [18]. TNT layers show a periodicity of the crystal structure for wavelengths equal to 550–700 nm. The result is an improvement in terms of visible light harvesting, although it should be noted that this strong visible-light absorption (being related to light diffraction and scattering, rather than absorption with the generation of charge separation) does not produce in principle an improved photocatalytic activity.

As observed in phononic materials such as Au-doped TiO_2 [19], an absorption in the visible region may generate ‘‘hot” electrons with an increase in the photocurrent observed even with light irradiation filtered from the UV component. Although phononic and photonic effects are different, there is some photocurrent generated using only visible-light component in TNT films, likely for an analogous mechanism of generation of ‘‘hot” electrons; however, this effect is different from the enhanced visible absorption due to doping of titania [20].

Sample	Transmitted Irradiance ($W\ cm^{-2}$)	Absorbed Irradiance P_{tot} ($W\ cm^{-2}$)
Incident light	0.1350	0
TNT 45 min	0.0829	0.0521
TNT 1 h	0.0762	0.0588
TNT 3 h	0.0562	0.0788
TNT 5 h	0.0509	0.0841

Table 3.2:

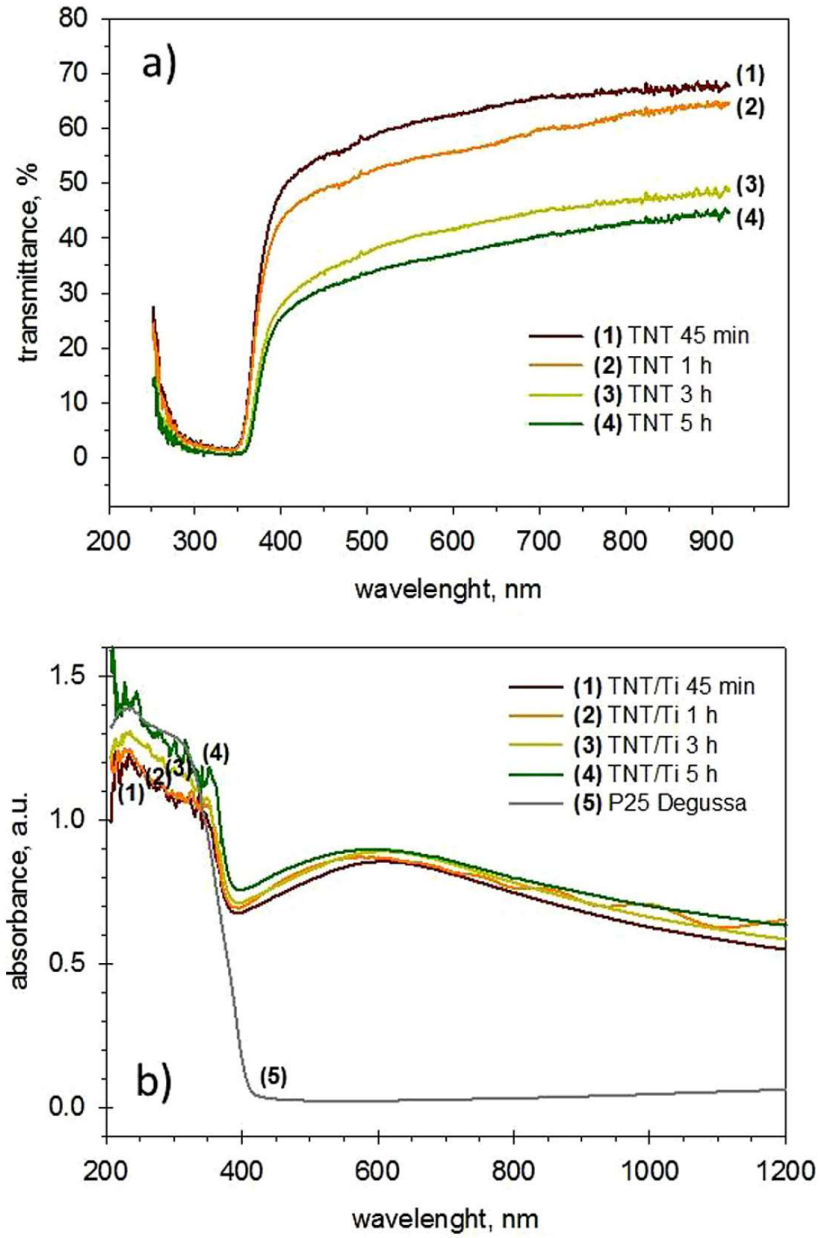

Fig.3.12: a) UV–visible light transmittance (obtained by using a spectroradiometer probe) of TNTs samples and b) UV–visible diffuse reflectance spectra of TNTs/Ti samples (prepared at different anodization times).

3.4.3 Charge separation and electron transport

Chronoamperometry is a valid tool for the evaluation of the performance of TNTs on PECa cell. The measurements were made in KOH (1 M) at 0.1 V (vs. Ag/AgCl) using an electrochemical cell with a three-electrode configuration (Figure 3.13). Current density vs. time profiles referred to the studied TNT samples were obtained both at open spectrum (no light-cutting filter) and

using different filters to select the desired wavelength region (see light-cutting filters reported in Figure 3.5).

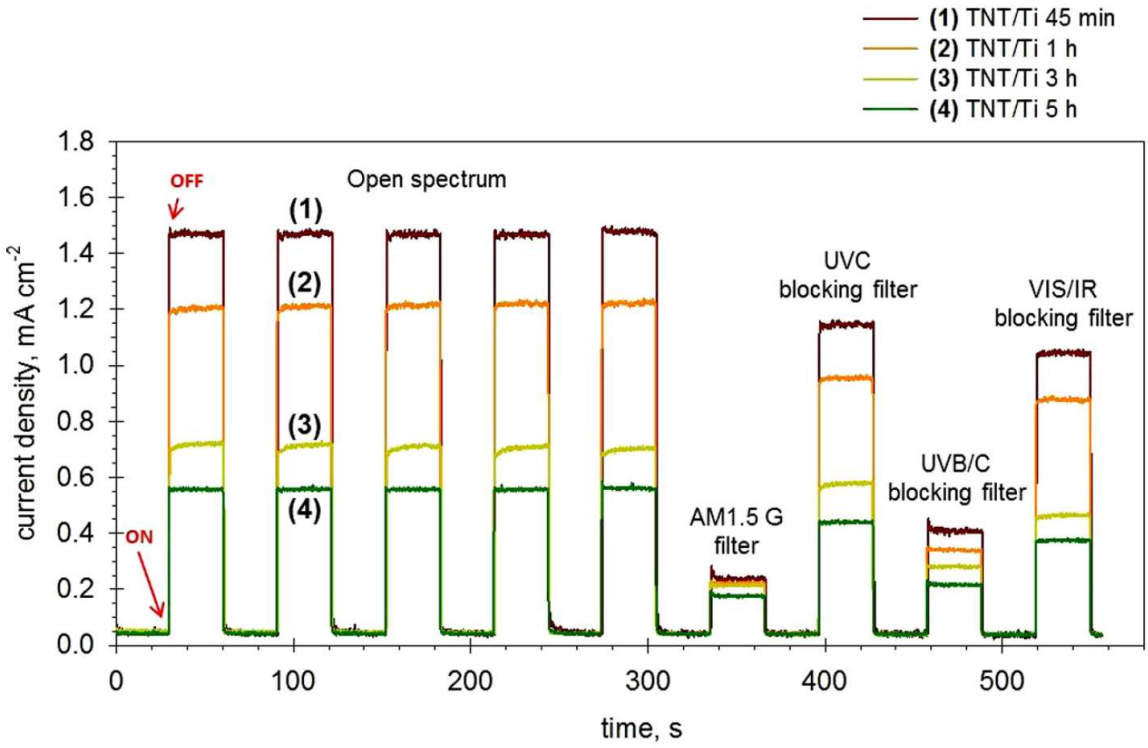

Figure 3.13: Chronoamperometric measurements for TNTs/Ti samples prepared at different anodization times (0.1 V vs. Ag/AgCl, 1 M KOH).

All the samples showed a quick rise in photocurrent and fast recovery to the original value through multiple ON/OFF cycles with a stable and reproducible photocurrent for all the tested TNT samples. The sample with lower film thickness (i.e. anodized for 45 min) provided the highest photocurrent response, while the photocurrent progressively decreased for higher thicknesses. This phenomenon is exactly the opposite of that showed in the transmittance behaviour and, even if a thicker film should absorb more light, the sample anodized for 45 min was already able to absorb all the UV component of light. For the samples anodized for 1, 3 and 5 h, a higher probability of charge recombination exists, because the initial charge separation (created at the top part of the layer) has a longer distance to cover before reaching the collector layer of Ti. This result is in accordance to different proposed mechanisms of charge recombination [21]. The percentage of photocurrent obtained using visible light with respect to the current generated at open spectrum increased for longer tubes: from 16.0% for 45 min TNT sample to 31.3% for 5 h TNT sample in case of using AM 1.5G filter (simulating standard

terrestrial solar irradiance distribution). Due to their specific nanostructure, TNT films are able to show some photo-generated current and photo-electrolysis activity under visible light. Being light absorption in the visible region depending on the film thickness (see Figure 3.12a), there is also a dependence of the photo-generated current on the film thickness.

3.4.4 H_2 production and STH efficiency

The H_2 formation in PECa experiments is reported in figure 3.14. All the samples show an initial induction period of 10–15 min, due to the need to establish the equilibrium in the cell. Later, the H_2 evolution increases linearly with a quite constant production rate. O_2 was detected in the anode side and the H_2:O_2 ratio was the expected for stoichiometric water photo-electrolysis, while no hydrogen evolution was detected in the anode. Following the trend of the photocurrent measurements, the maximum in H_2 productivity was observed for the 45-min-anodized TNT sample, giving about 560 µmol in 5 h of light irradiation, followed by the TNTs with higher layer thickness. However, the sample prepared at 30 min of anodization was out of this trends because, even if it has a lower film thickness (lower with respect to 45 min anodized sample), the absence of the tubular nanostructure results in a higher charge recombination rate, higher than the sample anodized for 5 h. The average H_2 production rates (µmol h^{-1}) are showed in the inset of figure 3.14.

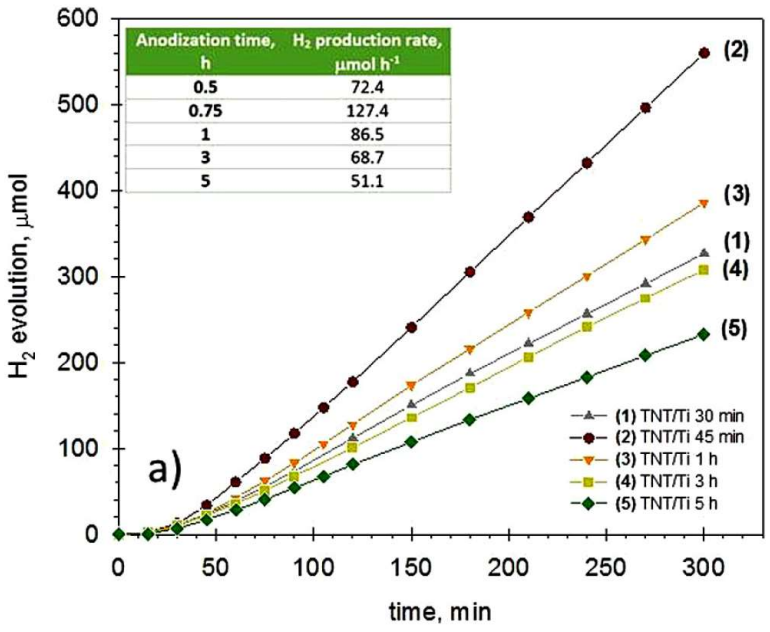

Figure 3.14: Hydrogen evolution vs. time for TNTs/Ti samples prepared at different anodization times. Inset, a table showing the average H_2 production rates.

It is not easy to make a comparison with literature data because of the different types of cells and conditions used (e.g. the electrolyte, the use of a sacrificial agent and/or an external bias between the two electrodes) [22]. Stoll et al. [23] reported recently a H_2 production rate of about 2 nmol s^{-1} (72 µmol h^{-1}) in a PEM-PEC cell based on 0.7 µm-thick TNTs prepared in 1 h anodization time, but with an applied extra bias of 1.23 V. Obviously the data reported in literature for PEC cells without external bias or sacrificial agents are typically lower. Schmuki et al. recently obtained a maximum H_2 generation rate of about 20 µmol h^{-1}, but they used Pt-doped titania nanotubes [24]. Selli and coworkers reported a H_2 production rate of 0.153 mmol h^{-1} using an irradiated area of about 10 cm^2 with no electrical bias or sacrificial agent employed during the tests [25]. They obtained a H_2 production rate per unit area of 15.3 µmol h^{-1} cm^{-2}, but in the experiments obtained during this PhD research activity (see inset of Fig. 3.14), the highest productivity in H_2 formation per unit area was 22.4 µmol h^{-1} cm^{-2}, that is about 1.5 times higher than that obtained from Selli and coworkes's work. It is reasonable to assume that the best performances are to ascribe to the highly compact design of our PECa cell, which allowed to minimize all the issues generally presented in conventional photo-reactors, as described in Chapter 2.

Figure 3.15 shows the production of H_2 and the ABPE efficiency (calculated by equation 3.2) in the case of applied voltage. The best performance in terms of ABPE was obtained at $V_{bias} = 0$ (exactly when ABPE is the same of STH efficiency). When the energy supplied is higher than the output energy obtained as H_2 evolution, ABPE becames negative (+1,5 V).

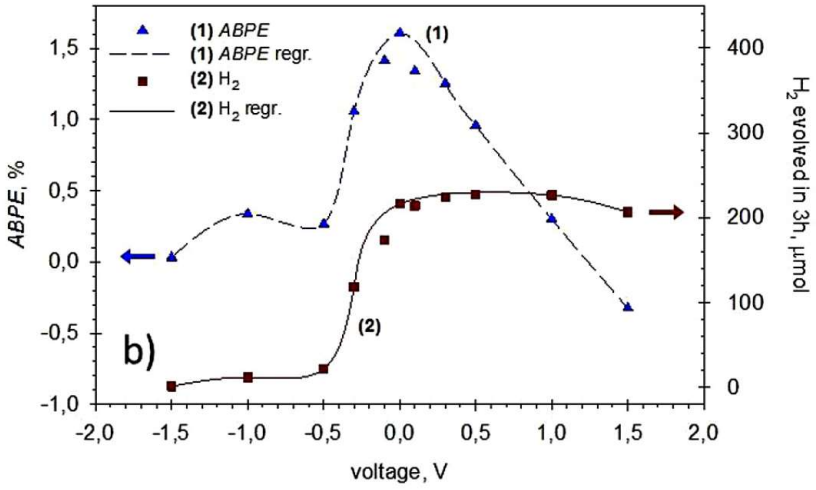

Figure3.15: ABPE and H_2 evolved in 3 h vs. applied voltage.

The onset of H_2 evolution starts at -0.5 V, reaching a maximum in the range 0/+1.0 V and slightly diminishing at +1.5 V. The electron conductivity between the two electrodes is not the rate-limiting step of the PECa process, but the formation/diffusion of protons within the cell might cause the losses of overpotential. The STH efficiency values calculated by equation (3.1) are reported in Table 3.2. The irradiance values (P_{tot}) used for the calculations are those reported in Table 3.1. The higher STH efficiency value was obtained for the 45-min anodized TNTs sample (2.5%). While the trend is inversely proportional to the anodization time due to the decreasing of H_2 production by increasing the tube length.

Sample	STH efficiency (%)
TNT 45 min	2.46
TNT 1 h	1.60
TNT 3 h	1.04
TNT 5 h	0.72

Table 3.2: STH efficiency at V_{bias} = 0 for time-differently anodized TNT samples.

3.4.5 Faradaic efficiency, IPCE and APCE

As discussed in paragraph 3.3.4, a useful parameter for evaluating PECa performance is the Faradaic efficiency. It is a measure of how much electrons are actually converted into chemical energy (hydrogen or oxygen). The η values for the time-differently anodized TNTs samples are reported in Table 3.3. The 45 min and 1 h anodized TNTs samples showed an efficiency higher than 99%, this means that almost all of the photo-generated current was converted into H_2. The Faradaic efficiency diminished by increasing the TNTs thickness, confirming that for higher nanotube length the charge recombination is the main issue.

Sample	Faraidic efficiency (%)
TNT 45 min	99.3
TNT 1 h	99.2
TNT 3 h	85.1
TNT 5 h	75.0

Table 3.3: Faraidic efficiency for TNTs samples anodized from 45 min to 1 h.

The incident photon to current conversion efficiency (IPCE) represents an important parameter to determine PECa performance. IPCE is also called the external quantum efficiency and is a measure of the capacity of converting the incident photons to the photocurrent flowing between the working and counter electrodes. it can be calculated by the following equation:

$$IPCE\ (\%) = 1240\ \frac{I_p(\lambda)}{P_{inc}\ (\lambda)\ \lambda} * 100 \tag{3.5}$$

where Ip (λ) is the photocurrent density (A m^{-2}) and P_{inc} (λ) is the incident power density of light (W m^{-2}) at wavelength λ (nm). The constant ‘‘1240” has the unit W nm A^{-1}. When the IPCE value reachs 100%, all the photons generated creates the electron-hole pairs, but due to the losses corresponding to the reflection of incident photons, the imperfect absorption by the semiconductor and recombination of charge carriers, the IPCE values are less than 100% [26]. The IPCE is usually calculated by measuring the current in the cell under the application of a single wavelength (or a small group of wavelength). The IPCE (%) was calculated for the one-hour-anodized sample and its profile (vs. wavelength) in the range 300–500 nm is showed in Figure 3.16. The solar spectral irradiance (AM 1.5G) has also been reported in the same graph as reference.

The graph in Figure 3.16 reports also the absorbed photon to current efficiency (APCE) calculated for the same sample. APCE is also called the internal quantum efficiency and it is defined as the number of electrons collected per absorbed photon and was calculated by the following equation:

$$APCE\ (\%) = 1240\ \frac{I_p(\lambda)}{P_{abs}\ (\lambda)\ \lambda} * 100 \tag{3.6}$$

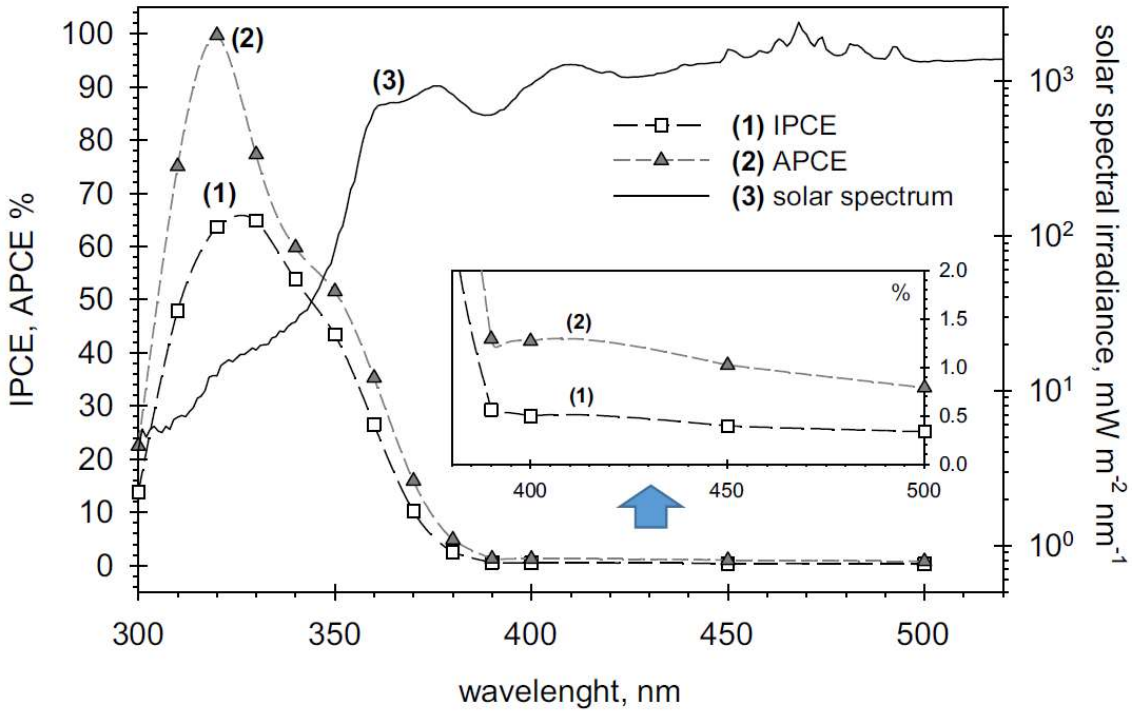

Figure 3.16: ABPE and H_2 evolved in 3 h vs. applied voltage.

The calculation of APCE is the same for that of IPCE except for the irradiance values P (λ) in which for APCE the irradiance value is referred to that absorbed from the TNT layer (P_{abs}). The IPCE shows its maximum value of about 65% at 330 nm, while the value of APCE at the same wavelength is almost 100%. In the visible light region (400–500 nm), IPCE has an average value of 0.3–0.4%.

The APCE calculation does not take into account the losses in the incident photons like reflection, scattering, etc., as it only refers to the absorbed light. Moreover, the APCE shows a small peak in the visible light region centred at 410 nm (see the inset in figure 3.16), with a value of about 1.3%, evidencing the photo-activity of the TNTs layer also in the visible region.

3.5 3D type titania nanotubes on Ti grid

Within a collaboration with the "Institut de Chimie de Lyon" of the CNRS-CPE Lyon, part of the research was dedicated to the synthesis and characterization of 3D type titanium oxide nanotubes. The idea derives from the necessity to make small holes in the Ti substrate to connect the photo-anode to the cathode in a PECa cell, allowing the passage of protons. For

this reason, the grids of Ti were anodized, very similar to the Ti discs, and their light absorbance and mass transfer characteristics were examined.

Specifically, the 3D type TNT electrodes were synthetized by controlled anodic oxidation of a macroporous Ti substrate. The starting metallic substrate (supplied by Alfa Aesar) consists of Ti wires (0.13 mm diameter) regularly woven to form an 80 mesh (i.e. 0.177 mm) gauze with an open geometric area of 36%. Like the Ti discs, the grids were also pre-treated by a strong sonication for 30 min. The setup for anodization is the same used for the discs, but the voltage was varied in the range of 40-70 V and time in the range of 1-7 h. The characterization and testing equipment is the same used for Ti discs.

In the 3D type TNTs, two types of porosity exist: i) a macroporosity, due to the meshes of the Ti gauze (80 mesh, i.e. 0.177 mm) and ii) a mesoporosity due to the TiO_2 nanotubes having an inner diameter in the range 40–120 nm. Figure 3.17a-b shows respectively the Ti grid non anodized and the grid after the anodization process. High magnification in figure 3.17 c-d confirms the presence of the tubular structure.

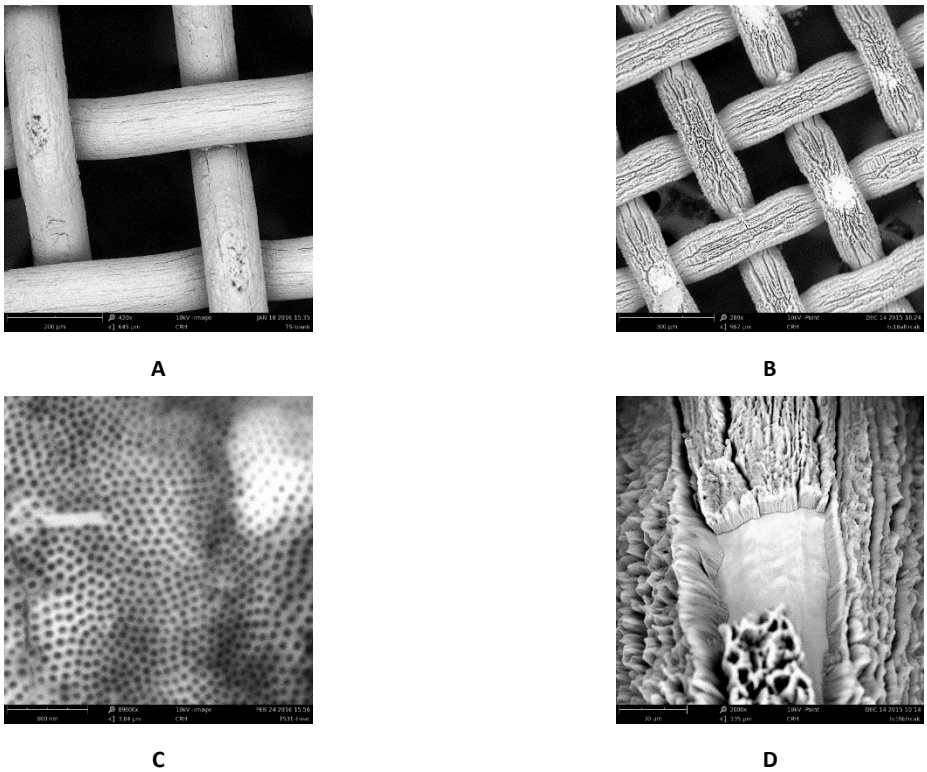

Figure 3.17: SEM images of a) low magnification of Ti grid non anodized b) Ti grid anodized c) high magnification of TNTs on grid and d) TNTs grown on single wire (the broken piece allows to see the tubular structure).

The synthesis parameters influence the morphology of the tubes as in the case of the anodization of the Ti discs. The increase in the length of the tubes is related to the time of anodization, but while for the nanotubes on the disc the anodization time did not influence the internal diameter, for the nanotubes, for the case of the grid an increase of the internal diameter was observed by increasing the anodization time. Figure 3.18 shows the parameters for the sample anodized at 50 V with time ranging from 20 m to 7 h. The percentage of voids was quite constant until 5 h and strongly diminished at 7 h.

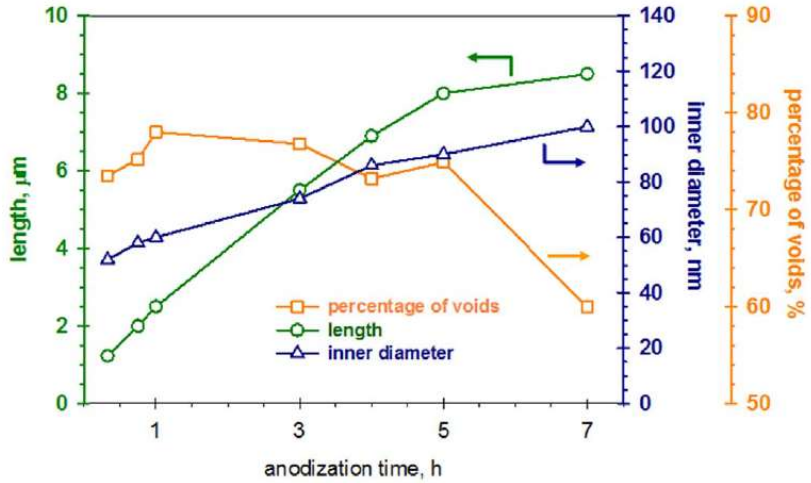

Figure 3.18: Profiles of length, internal diameter and percentage of voids of 50 V-anodized TNTs-Ti mesh versus time of anodization.

The 3D type TNT electrodes were fianlly tested in the PECa cell for H_2 production in the process of water photo-electrolysis. Two main aspects influence the H_2 productivity tests (Figure 3.19): if the increasing length of the nanotubes negatively influences the H_2 production (like in the case of TNTs on discs), on the other side the increasing of diameter also increases the H_2 production, and this resulting in a minimum at 3h of anodization. The value of H_2 production at 7 h of anodization, instead, is out of the above explained trend, because of the percentage of void that strongly diminished for higher time of anodization (as showed in Figure 3.18). This results to a higher number of contacts among the tubes that increase the charge recombination effect, limiting the entire photo-electrolysis process.

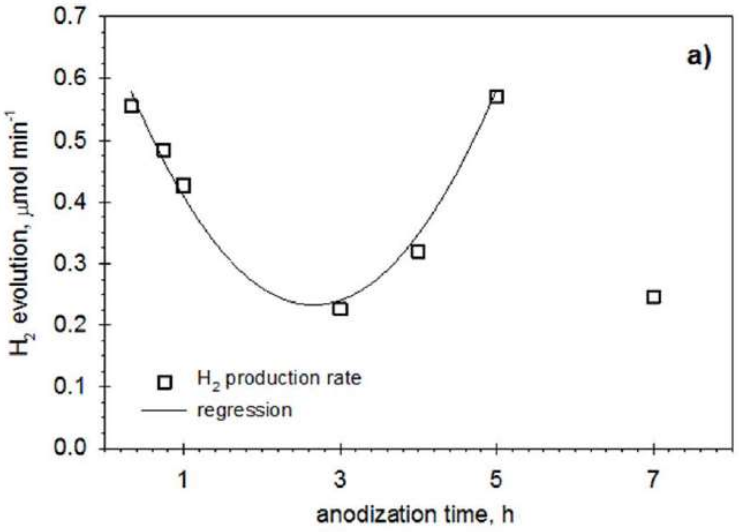

Figure 3.19: anodization time vs H_2 production for the 50V anodized samples

These 3D type titania nanotubes based electrodes, not only act as photoactive materials for water splitting, but also operate as a membrane that allows the permeation of the electrolyte to and from the Nafion© membrane with the improvement of the mass transport effect.

3.6 Conclusions

The aim of this chapter was to investigate the morphology of the titania nanotubes array TNTs and improve the performances in a PECa cell for H_2 generation through the water splitting reaction. The following results were obtained:

1) **Synthesis** of TNT films with different tube length was performed by the use of anodization technique that allows to prepare highly order TNT arrays with tube length from 1 to 5 µm by increasing the anodization time from 30 min to 5 h. The as-prepared TNTs have similar nanotube diameter, show uniform thickness and clean top surface and are characterized by the same crystallinity degree in anatase phase.
2) **Tests** in a compact PECa device for the water photo-electrolysis reaction were conducted for the as prepared samples. Results showed that the increase of thickness, despite the increase of light absorbance, negatively affects the photocurrent generation and the relatively H_2 production. The sample anodized for 45 min providing the maximum H_2 production of 22.4 µmol h^{-1} cm^{-2}.

3) **Efficiencies** were determined in order to evaluate the entire system (TNTs + PECa). A photoconversion efficiency (solar-to-hydrogen –STH- efficiency) of about 2.5% was obtained. This value is among the best ever reported insofar as PECa cells use undoped TiO_2 photoanodes and in absence of external bias or sacrificial agents. Quantum efficiency (IPCE and APCE) were also measured confirming the presence of visible light activity related to the nanostructure of TNTs.
4) **Mass Transport** phenomena were investigated and the realization of 3D type interconnected structure was made in collaboration with the CNRS-CPE of Lyon. The results showed that both length and inner diameter of the tubes affect the H_2 production with an opposite trend with the samples anodized at 20 min and 5 h at the top and the sample at 3h at the minimum.

Next chapter will be focused on solving the other main issue related to the use of titanium dioxide as efficient photocatalyst, i.e. the visible light harvesting.

3.7 References

[1] A. Fujishima, K. Honda, *Electrochemical Photolysis of Water at a Semiconductor Electrode. Nature* 238, 37 (1972)

[2] W. Fang, M. Xing, J. Zhang, *Modifications on reduced titanium dioxide photocatalysts: A review*, J. of Photochem. and Photobio. C: Photochem. Rev. 32, 21–39 (2017)

[3] Z. Xing, J. Zhang, J. Cui, J. Yin, T. Zhao, J. Kuang, Z. Xiu, N. Wan, W. Zhou, *Recent advances in floating TiO_2-based photocatalysts for environmental application*, App. Cat. B: Envir. 225 452–467 (2018)

[4] D. Gong, C.A. Grimes, O.K. Varghese, W. Hu, R.S. Singh, Z. Chen, E.C. Dickey, *Titanium oxide nanotube arrays prepared by anodic oxidation* J. Mater. Res. 16 3331 (2001)

[5] Berger, S., Hahn, R., Roy, P., Schmuki, P. *Self-organized TiO2 nanotubes: Factors affecting their morphology and properties* Phys. Stat. Solid (B) Basic Res. 247, 10, 2424-2435 (2010)

[6] R. Singh, S. Dutta, *A review on H_2 production through photocatalytic reactions using TiO_2/ TiO_2-assisted catalysts* Fuel 220 607–620 (2018)

[7] Y. Zhao N. Hoivik K. Wang, Recent advance on engineering titanium dioxide nanotubes for photochemical and photoelectrochemical water splitting Nano Energy 30, 728-744 (2016)

[8] C. Ampelli, G. Centi, R. Passalacqua, S. Perathoner. *Synthesis of solar fuels by a novel photoelectrocatalytic approach*, Ener. & Envir. Sci., 3, 292-301 (2010)

[9] C. Ampelli, C. Genovese, R. Passalacqua, S. Perathoner, G. Centi. *The Use of a Solar Photoelectrochemical Reactor for Sustainable Production of Energy*, Theor. Found. of Chem. Engineer., 46, 6, 651-657 (2012)

[10] C. Ampelli, R. Passalacqua, S. Perathoner, G. Centi. *Development of a TiO_2 nanotube array-based photo-reactor for H_2 production by water splitting*, Chem. Engineer. Trans., 24 187-192, (2011)

[11] C. Ampelli, F. Tavella, S. Perathoner, G. Centi, *Engineering of photoanodes based on ordered TiO_2-nanotube arrays in solar photo-electrocatalytic (PECa) cells*, Chem. Engineer. J. 320 352–362 (2017)

[12] T. Saboo, F. Tavella, C. Ampelli, S. Perathoner, C. Genovese, B. C. Marepally, L. Veyrea, E. A. Quadrelli, G. Centi *Water splitting on 3D-type meso/macro porous structured photoanodes based on Ti mesh*, Sol. Energy Mat. and Sol. Cells 178 98–105 (2018)

[13] G.K. Mor, O.K. Varghese, M. Paulose, *A Review on highly ordered vertically oriented TiO_2 nanotube arrays*, Sol. Energy Mat. & Sol. Cells 90, 2011–2075 (2006)

[14] L.V. Taveira, J.M. Macák, H. Tsuchiya, L.F.P. Dick, P. Schmuki, *Initiation and growth of self-organized TiO_2 nanotubes anodically formed in $NH_4F/(NH_4)$ SO_4 electrolytes,* J. Electrochem. Soc. 152 B405–B410, (2005)

[15] C. Ampelli, R. Passalacqua, S. Perathoner, G. Centi. *Nano-engineered materials for H_2 production by water photo-electrolysis,* Chem. Engineer. Trans., 17, 1011-1016 (2009)

[16] O.K. Varghese, C.A. Grimes, *Appropriate strategies for determining the photoconversion efficiency of water photoelectrolysis cells: A review with examples using titania nanotube array photoanodes,* Sol. Energy Mat. Sol. Cells 92 374–384, (2008)

[17] C. Dette, M.A. Pérez-Osorio, C.S. Kley, P. Punke, C.E. Patrick, P. Jacobson, F. Giustino, S. Jung Jung, K. Kern, *TiO_2 anatase with a bandgap in the visible region*, Nano Lett. 14 6533–6538 (2014)

[18] P. Li, S.-L. Chen, A.-J. Wang, Y. Wang, *Probing photon localization effect between titania and photonic crystals on enhanced photocatalytic activity of titania film*, Chem. Eng. J. 284 305–314 (2016)

[19] C. Ampelli, F. Tavella, C. Genovese, S. Perathoner, M. Favaro, G. Centi, *Analysis of the factors controlling performances of Au-modified TiO_2 nanotube array based photoanode in photo-electrocatalytic (PECa) cells*, J. Energy Chem. (2016),

[20] C. Ampelli, R. Passalacqua, S. Perathoner, G. Centi, D.S. Su, G. Weinberg, *Synthesis of TiO_2 thin films: relationship between preparation conditions and nanostructure,* Top. Catal. 50 133–144, (2008)

[21] S. Gimenez, H.K. Dunn, P. Rodenas, F. Fabregat-Santiago, S.G. Miralles, E.M. Barea, R. Trevisan, A. Guerrero, J. Bisquert, *Carrier density and interfacial kinetics of mesoporous TiO_2 in aqueous electrolyte determined by impedance spectroscopy,* J. Electroanal. Chem. 668 119–125 (2012)

[22] M. Antoniadou, S. Sfaelou, P. Lianos, *Quantum dot sensitized titania for photofuel-cell and for water splitting operation in the presence of sacrificial agents,* Chem. Eng. J. 254 245–251 (2014)

[23] T. Stoll, G. Zafeiropoulos, M.N. Tsampas, *Solar fuel production in a novel polymeric electrolyte membrane photoelectrochemical (PEM-PEC) cell with a web of titania nanotube arrays as photoanode and gaseous reactants,* Int. J. Hydrog. Energy (2016)

[24] J. Yoo, M. Altomare, M. Mokhtar, A. Alshehri, S.A. Al-Thabaiti, A. Mazare, P. Schmuki, *Photocatalytic H_2 generation using dewetted Pt-decorated TiO_2 nanotubes: optimized dewetting and oxide crystallization by a multiple annealing process,* J. Phys. Chem. C 120 15884–15892 (2016)

[25] G.L. Chiarello, A. Zuliani, D. Ceresoli, R. Martinazzo, E. Selli, *Exploiting the photonic crystal properties of TiO_2 nanotube arrays to enhance photocatalytic hydrogen production,* ACS Catal. 6 1345–1353 (2016)

[26] S.-F. Leung, Q. Zhang, M.M. Tavakoli, J. He, X. Mo, Z. Fan, Progress and design concerns of nanostructured solar energy harvesting devices, Small 12 (2016) 2536–2548.

4 Improving visible light activity

4.1 State of the art

One of the most important challenges in photocatalysis and photo-electrocatalysis is to develop a catalytic material able to work efficiently in the conversion of solar energy into chemicals and fuels. In general, an efficient photocatalyst should have the following characteristics: i) light harvesting, especially under visible light to exploit the entire solar spectrum; ii) electron-hole pair formation, with no fast charge recombination and iii) stability and resistance to photo-corrosion [1]. Thin films based on ordered arrays of vertically aligned TiO_2 nanotubes have been successively developed to overcome most of the issues reported above: they are stable and show a vectorial transport of electrons, minimizing the charge recombination phenomena. Moreover, TiO_2 nanotube arrays behave as efficient photo-active materials not only in the UV light region, but they also show some activity under visible light. As discussed in Chapter 3, this can be ascribed to the structural resonance effect, due to the presence of highly ordered nanotubes, even if in principle this could not be associated to an increase of photocatalytic activity.

Thus, a great interest exists on the modification of titania-based photocatalysts with the attempt of further improving their visible light absorption properties [2-3]. In this context, the deposition of metal particles on TiO_2 has been widely investigated in literature, in order to improve the photo-catalytic performances by heterojunction, co-catalysis, co-alloying or plasmonic effects [4]. Noble metal (Au, Pt) nanoparticles have been used to modify TiO_2 surface [5-6]. However, the use of non-critical raw materials should be preferable for both cost and sustainability motivations. In this context, the use of CuO and Cu_2O as earth-abundant materials has become of great interest due to their photoactive properties, good environmental acceptability, low thermal emittance, non-toxicity and simple and low-cost production process [7-8]. Recently, the modification of TiO_2 nanotubes with copper oxides (CuO and Cu_2O) and metallic copper has been studied in order to improve the photo-response of the system [9-10].

4.2 The scope of the chapter

There are several strategies to improve the characteristics of TiO_2–based photocatalysts. Chapter 3 was dedicated to the synthesis of ordered arrays of vertically aligned TiO_2 nanotubes, in order to improve the electrical transport and minimize charge recombination phenomena, particularly focusing on the optimization of the nanotube length. The aim of this chapter is instead to improve the visible light absorption properties of the TiO_2 nanotube arrays, by investigating different techniques for the modification of TiO_2. In particular, the surface of nanostructured TiO_2 was decorated with metal nanoparticles (NPs), acting as visible light absorption centres and also as catalytic active sites for the combination of protons and electrons to produce hydrogen.

Particularly, nanoparticles of gold (Au) (evidencing the typical plasmonic effect) were deposited on the surface of the TiO_2 nanotubes by three different techniques (wet impregnation, photo-reduction and electrodeposition) and their performances were studied under different operating conditions by using a gas photo-reactor (GP) and a homemade photo-electrochemical (PEC) cell. The photo-catalytic behaviour of Au-doped TNTs was evaluated in the process of water photo-electrolysis, as well as in the photo-reforming of simulated organic streams.

Then, the attention has moved towards Cu-doped TiO_2 nanotubes, with the aim of exploiting earth-abundant and low-cost materials. Copper is an interesting element, evidencing a behaviour of p-type semiconductor and also showing the plasmonic effect when present in the form of nanoparticles. This makes copper-doped materials suitable to be used as efficient visible light photo-catalysts. This part of the work was carried out in collaboration with the Institute of Chemistry in Araraquara (Brazil). The Cu-based nanoparticles were deposited on TNTs by adopting three different techniques, dip-coating, spray coating and electrodeposition. Finally, they were tested for ethanol degradation in GP reactor and water splitting in the PEC cell.

4.3 Experimental

The synthesis of titanium dioxide nanotubes through the anodization process has already been described in Chapter 3 (paragraph 3.3.1). The experimental section of this chapter will

focus on the techniques of deposition adopted for the decoration of TNT with gold (Au) and copper (Cu) nanoparticles (NPs).

4.3.1 Deposition of Au nanoparticles (Au NP)

For the synthesis of TNTs with gold nanoparticles (Au NPs) three techniques were performed: (1) wet impregnation, (2) photo-reduction and (3) electrodeposition:

1) *Wet impregnation* a modified wet impregnation technique was used for the deposition of gold on the TNT surface. After calcination, the TNT/Ti electrode was located at the bottom of a beaker (having a diameter slightly larger than the round 3.5 cm TNT/Ti disc), which was filled with an aqueous solution of $HAuCl_4$ and heated to 60 °C under constant slow stirring until complete evaporation of the water.

2) *The photo-reduction* using the gas phase reactor described below (figure 4.1), Au NPs were deposited on TNT/Ti film. The electrodes were first immersed in the aqueous metal precursor solution ($HAuCl_4$) for the time necessary to fill the nanotubes by capillary forces (30 min) and then they were exposed to the UV-visible lamp under a low inert gas flow (N_2) to reduce Au and form NPs.

3) *Electrodeposition* the Au/TNTs by electrodeposition was produced in a conventional electrochemical cell with a three-electrode configuration using Ag/AgCl as the reference electrode and a Pt rod as the counter-electrode. The working electrode (TNT/Ti) was subjected to cyclic voltammetry in presence of the metal precursor ($HAuCl_4$) in 1 M phosphate buffer solution (PBS). Seven cycles from 0 to + 1.4 V were performed at a scan rate of 20 mV s^{-1} and at 50 °C. Later, the electrodes were washed in deionized water under sonication to remove the excess of gold.

All the samples prepared by the described techniques, after the deposition procedure were dried in air at 200 °C for 2 h at a heating rate of 2 °C min^{-1}.

4.3.2 Deposition of Cu nanoparticles (Cu NP)

For the deposition of copper nanoparticles (Cu NPs) three main techniques were adopted 1) electrodeposition; 2) deposition of preformed nanoparticles; 3) dip-coating:

1) *Electrodeposition* for the electrodeposition of Cu NPs, a conventional electrochemical cell with three electrodes was used: the TNT/Ti as the working electrode, the Ag / AgCl as the reference electrode and a Pt wire as the counter-electrode. The electrode was subjected to seven cycles of potential variations ranging from 0 V to -0.8 V in an aqueous solution of 0.5 mM $CuSO_4$ at a scanning rate of 20 mV s^{-1} and 50 °C of temperature. After the Cu electrodeposition, the sample was dried in air at 200 °C for 2 hours with a heating rate of 2 ° C min^{-1}.

2) *Preformed (size-controlled) Cu nanoparticles* the synthesis of Cu NPs was made by using polyethylene glycol (PEG) as spacing agent and sodium borohydride as reducer in a basic solution. Ascorbic acid was added to avoid the fast metal oxidation. An aqueous solution containing 0.01 M of $CuSO_4$ $5H_2O$, 0.02 M of PEG 2000 and 0.03 M of l-ascorbic acid was prepared. A solution containing 0.1 M of $NaBH_4$ was added dropwise to obtain the complete reduction in 2 h. Later, the preformed Cu NPs were deposited on titania nanotube thin films by two methods: in situ reduction and spray coating. Regarding the in-situ reduction, the TNT electrode was added into the mixed solution before the $NaBH_4$ addition. The copper loading in this case was low, around 0.15 wt%. By spray coating, the metal nanoparticles were filtered and re dispersed in ethanol to be sprayed on the surface of the titania nanotube layer. In this case the loading obtained was higher (around 1 wt%).

3) *Dip coating* technique was used to decorate TNTs with Cu NPs by using an adapted methodology from Perazolli et al. [11]. The solution used for dip coating was prepared with copper nitrate hydrate (8.4×10^{-3} mol L^{-1} of metal) as copper oxide precursor, citric acid and ethylene glycol in molar ratio of 1:4:16, respectively. The electrode, after drying, was annealed at 450 °C for 3 h.

4.3.3 Gas phase reactor

The photo-reactor used for the ethanol degradation is homemade and made of Pyrex, with a quartz window to allow the irradiation of the photo-catalyst. The irradiated area is ca. 10 cm^2. Figure 4.1 shows the schematic drawing of the gas phase reactor (GP). The photocatalytic film is suspended inside the reactor behind the quartz window. 20 ml of EtOH aqueous solution (10% EtOH) is placed on bottom of the reactor and heated at 60°C. The entire set-up for the experiments is the same used for the PECa cell: a Xe-arc lamp (ORIEL, 300W) is used as light source and a gas chromatograph (Agilent 7090A) for products detection.

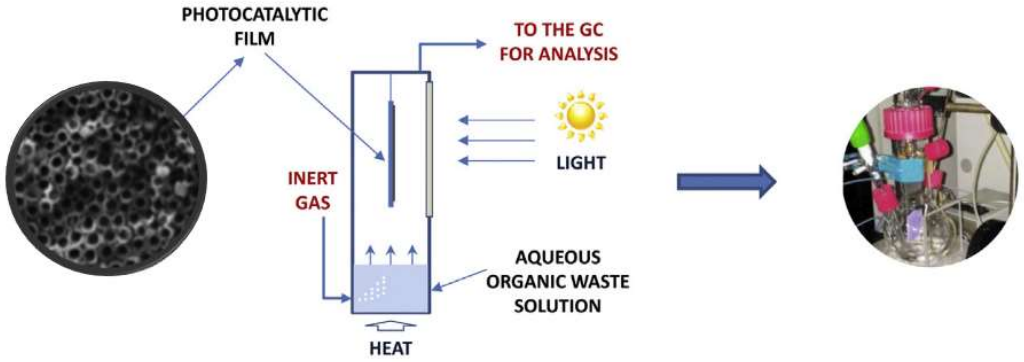

Figure 4.1: Scheme of the reactor used for gas-phase photocatalytic tests.

4.3.4 Characterization

Part of the characterization by electron microscopy (especially for Au-doped TNTs) was carried out in collaboration with the Department of Chemical Sciences of the University of Padua, by using a field emission scanning electron microscopy (FE-SEM, Zeiss model Supra 35) equipped with an energy dispersive X-ray (EDX) spectrometer. Copper-doped TNTs were instead analysed by using a SEM Philips XL-30-FEG operated at an accelerating voltage of 5 kV. High resolution transmission electron microscopy (TEM) images were recorded using a CM200 transmission electron microscope (TEM) (Philips/FEI, Netherlands) operated at 200 kV.

The total metal loading was evaluated by Atomic Absorption Spectroscopy (AAS) using an AAnalyst 200 spectrometer by PerkinElmer. For the analysis, the Cu and Au TNTs samples were sonicated in concentrated HF aqueous solution (48 wt%) to dissolve Cu/Au and the resulting

solution was analysed after proper dilution. The calibration curve was obtained by means of three standard solutions in the range 1–5 ppm by diluting Copper and Gold Standard for AAS (1000 mg L^{-1} in nitric acid) supplied by Sigma Aldrich.

X-ray Diffraction (XRD) patterns were recorded on a Bruker Model D2 Phaser. X-ray Photoemission (XPS) spectra were collected using PHI VersaProbe II analyzer. Cu_{2p} binding energies (BE) were recorded using AlKα (1486.6 eV) as the excitation source and a pass energy of 23.5 eV. The XPS spectra were recorded with setting of 100 µ100W20kv_HP. Position of XPS peaks of the corresponding element is referred to the C_{1s} peak of carbonaceous contamination, whose energy is taken equal to 284.80 eV.

An UV/Vis spectrometer (Jasco V-570PerkinElmer Lambda 1050) was used for diffuse reflectance measurements in order to obtain the optical band gap. Chrono-amperometry measurements were performed by the use of a three-electrode cell (already described in Chapter 3), with a Pt wire as counter-electrode and a saturated KCl-Ag/AgCl reference electrode. All the tests were performed at room temperature in 1 M KOH or 1 M Na_2SO_3 solutions at 0.1 V using a potentiostat–galvanostat (2049 AMEL).

4.4 Result and discussion

4.4.1 TNTs/Au NP characterization

Chapter 3 has shown that the length of the nanotubes has much influence on performance of a PECa cell. The transport of electrons occurs from the top of the nanotubes, where light harvesting is the greatest, to the bottom of the nanotubes and towards the collector layer (which is the metallic Ti remained non-oxidized after the anodization). Light absorption could be maximized by increasing the quantity of the photo-catalytic materials, for example obtaining longer TNTs by increasing the time of anodization. However, the results reported in Chapter 3 have demonstrated that, in PECa cells, the longer TiO_2 nanotubes are the more charge recombination phenomena occur; thus, a thin nanotube layer is preferable.

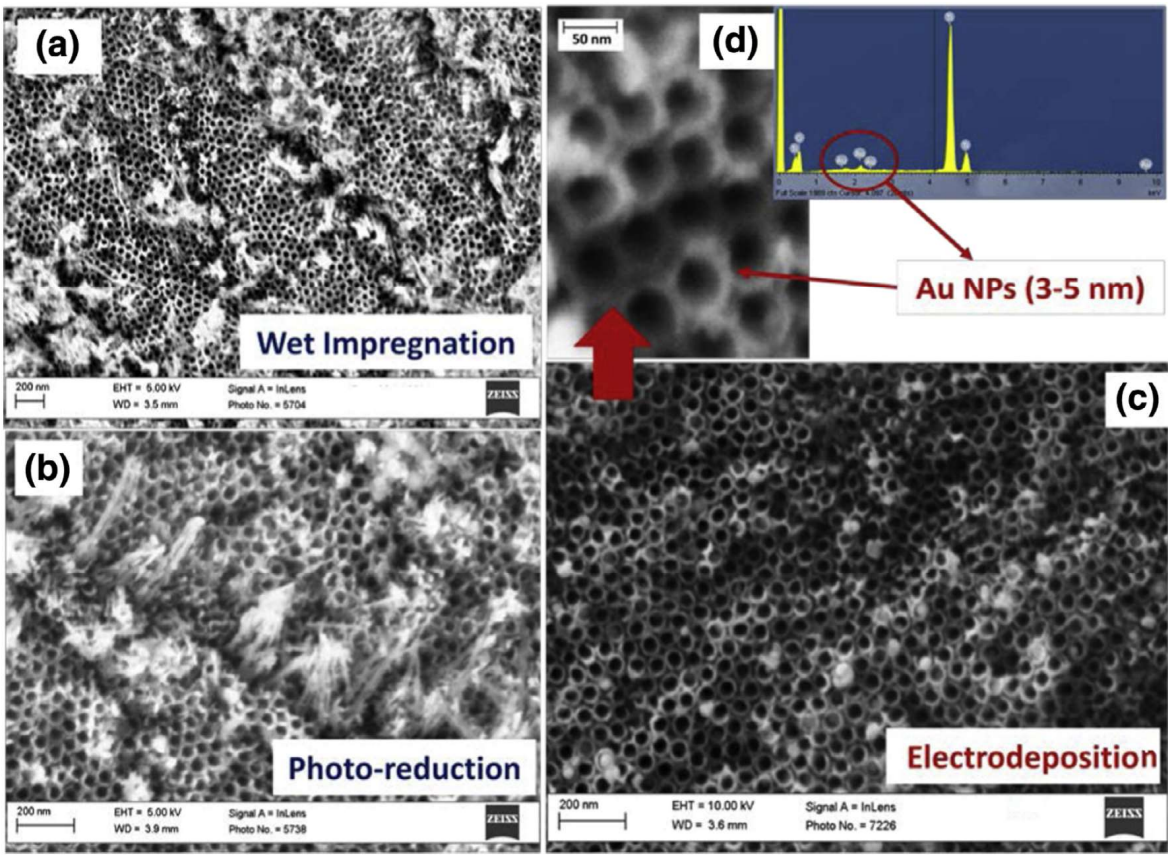

Figure 4.2: SEM top images of Au-modified TNT arrays with Au deposited by (a) wet impregnation, (b) photo-reduction, (c) electrodeposition. In (d) a magnification of (c) image is reported showing 3–5 nm Au NPs. EDX analysis is also reported.

Figure 4.2 shows the morphologies of the prepared vertically aligned Au-modified TNTs arrays. By the wet impregnation method, the samples showed aggregation of not well-dispersed Au NPs, deposited mainly on the top of the TNTs (figure 4.2a). Smaller and quite dispersed Au NPs (8–15 nm) were obtained by photo-reduction method (figure 4.2b). Some debris was present on the TiO_2 surface, which are residuals from the evaporation of the aqueous solution containing the precursor salt. Figure 4.2c shows the particles obtained with the electrodeposition method, resulting to be the best method for decorating homogeneously the surface of the TNTs. The electrodeposition technique allows to obtain a uniform dispersion of small particles (3-5 nm). The onset of figure 4.2d shows the EDX analysis, confirming the presence of gold on the TNT surface. A few bigger Au NPs (with size similar to the opening of the tubes) blocked up the holes of some tubes. Due to the resistance encountered by the aqueous Au precursor solution to fill completely the tubes by capillarity, the major part of Au NPs was deposited on the top of TNTs.

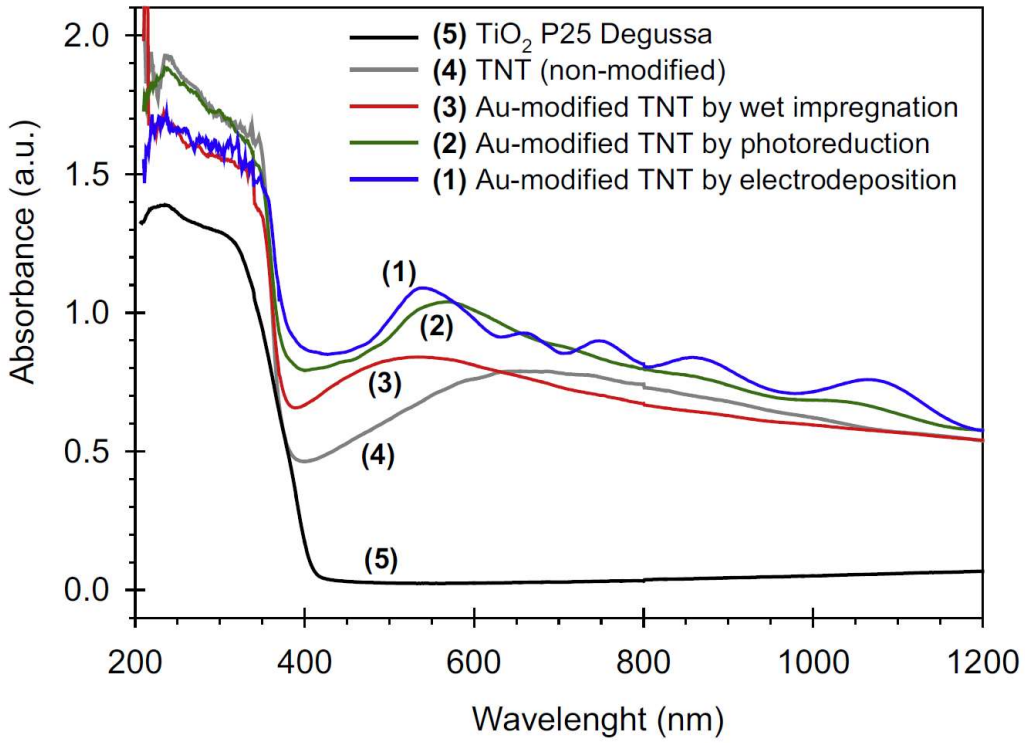

Figure 4.3: UV–visible diffuse reflectance spectra of Au-modified TNT arrays prepared by different Au deposition methods.

UV–visible diffuse reflectance spectra of the Au-modified TNT arrays prepared with the three different technique of Au deposition were reported in figure 4.3, together with the spectra of the bare TNTs arrays (non-modified) and commercial TiO_2 P25 Degussa. All the spectra exhibit a strong absorption band centred at about 350–400 nm related to the lowest energy charge transfer $O_2 \rightarrow Ti^{4+}$ and thus associated to the TiO_2 band gap consistent with expectations for a mixture of anatase and rutile TiO_2 polymorphs. The band-gap modification by the different deposition of gold are reported table 4.1.

Sample	Band gap (eV)
TNT	3.26
TNT-Au wet impregnation	3.16
TNT-Au photo-reduction	3.13
TNT-Au electrodeposition	3.08
TiO_2 P25 Degussa	3.04

Table 4.1: Bandgap modification of the three different TNT-Au samples.

All the spectra evidence a broad absorption peak centred around 550 nm (except for TiO_2 P25 Degussa) with a broad tail on the low energy side extending to the whole visible region. Also non-modified TNTs sample shows a broad absorption band in the visible region, although with a maximum centred around 650–700 nm This kind of absorption band is not present in films of TiO_2 prepared by sol–gel or by depositing commercial TiO_2 nanoparticles. It is related to light diffraction in 2D-type photonic materials. Au-modified TNT arrays prepared by electrodeposition presents a series of interference fringes in the range 600–1200 nm; this is probably related to the difference in distribution of Au NPs with respect to the other two methods of preparation. Likely, very small Au NPs on the top of the TNTs induce a localized surface resonance coupling with the resonances deriving from the Au NPs localized in other positions of the TNTs, where they are more influenced from the electromagnetic field generated by the photonic crystal.

BET surface area analysis showed a little increment of the surface area of TNT arrays in respect to that of Degussa P25 (68.1 vs. 48 $m^2 g^{-1}$) and no significant changes were observed after Au deposition. TNTs arrays were completely removed by a strong sonication treatment in order to discern the peaks of Ti to that of TNTs during the XRD analysis (figure 4.4). After annealing the TNT reached the crystallization, and only the anatase phase was present.

Diffraction Au peaks were also observed, even if barely discernible from the background, due to the low Au concentration on TNTs and to the small size of Au NPs obtained by electrodeposition technique, as confirmed by SEM analysis. To evaluate the effective Au metal loading in TNT, the as-prepared Au-modified TNT arrays were sonicated in concentrated HF aqueous solution (48 wt%) to dissolve Au and the resulting solutions, after proper dilution, were analysed by AAS. Calibration curves were obtained by means of three standard solutions in the range 1–5 ppm by diluting gold atomic spectroscopy standard concentrate (1.00 g L^{-1}) supplied by Sigma Aldrich. The analytical results showed about 1.5 wt% Au loading for the sample prepared by electrodeposition; a similar value was detected for the Au-modified TNTs sample prepared by photo-reduction, while the Au loading for the sample prepared by wet impregnation was higher (2.4 wt%).

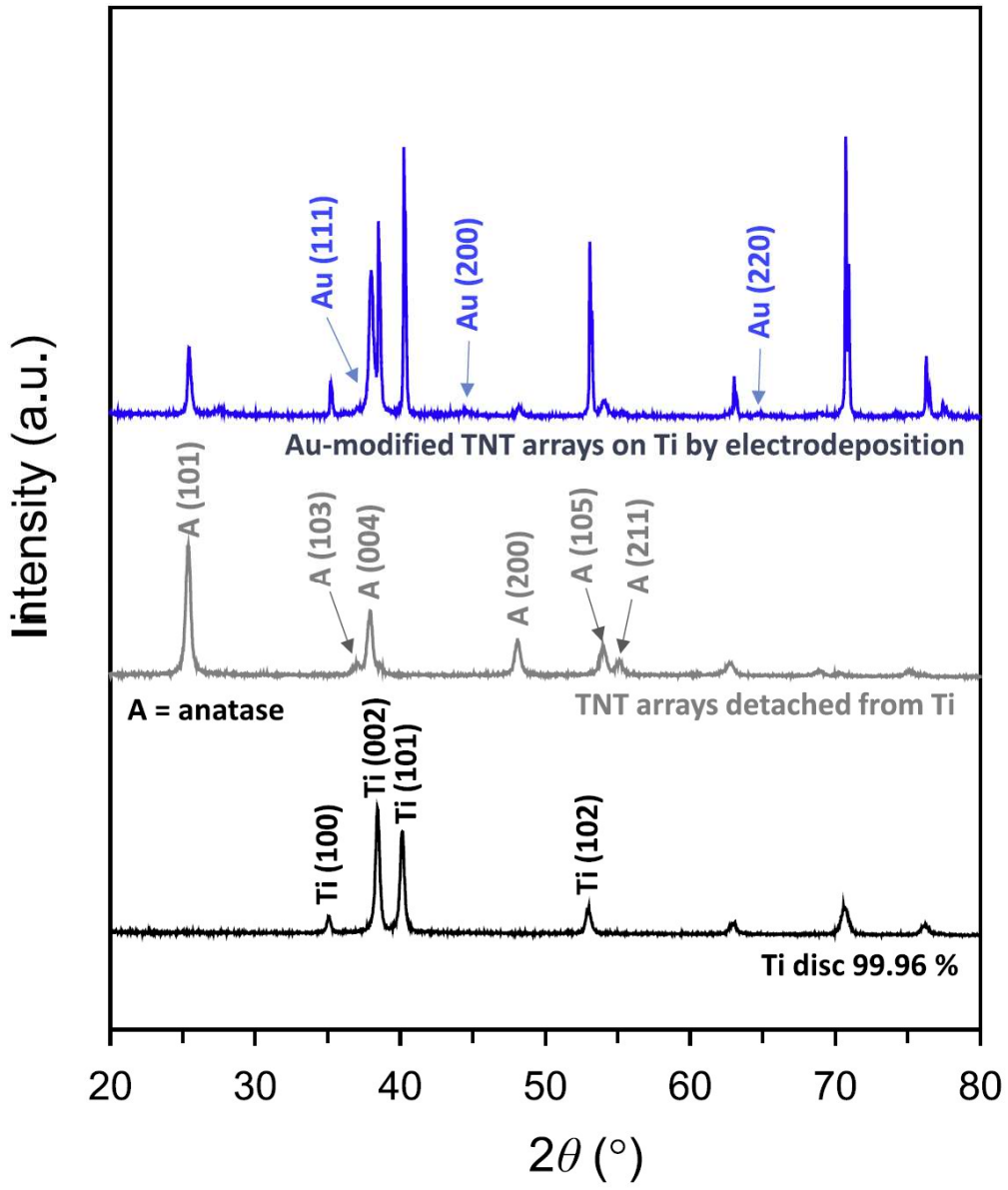

Figure 4.4: XRD patterns of (1) Au-modified TNT arrays on Ti with Au deposited by electrodeposition, (2) TNT arrays detached from the Ti layer and (3) pure Ti disc (99.96%).

The samples were also characterized by chrono-amperometric measurements, using different filters to select the desired wavelength region. Figure 4.5a shows the typical photocurrent vs. time profiles referred to non-modified TNTs arrays, obtained in a three-electrode cell using an aqueous solution of 1 M KOH at 0.1 V (Ag/AgCl reference electrode, Pt counter-electrode). The ON/OFF illumination at open spectrum displayed a quick rise in photocurrent and fast recovery to the original value through multiple ON/OFF cycles (four cycles). There is a stable and reproducible photocurrent for all the tested samples. By using the AM 1.5 G filter (simulating standard terrestrial solar irradiance distribution) the ON/OFF

increment was ~18% with respect to the value at open spectrum (no filter). Considering that the percentage of UV light in solar spectrum is only 4%, this result obtained by AM 1.5 G filter evidences the improved performance of TNT arrays in the visible region with respect to standard TiO_2.

Figure 4.5b shows the comparison between the all Au-modified TNT arrays prepared by the three different deposition techniques. Electrodeposition method allowed enhancing the photocurrent response, being 1.6 times higher than the photocurrent of the non-modified TNTs arrays, which becomes 1.8 times higher when the AM 1.5 G filter was used. The other deposition methods (wet impregnation and photo-reduction) did not give any improvements and photocurrent values even diminished with respect to the non-modified sample due to the charge recombination effect that affects mainly bigger Au particles.

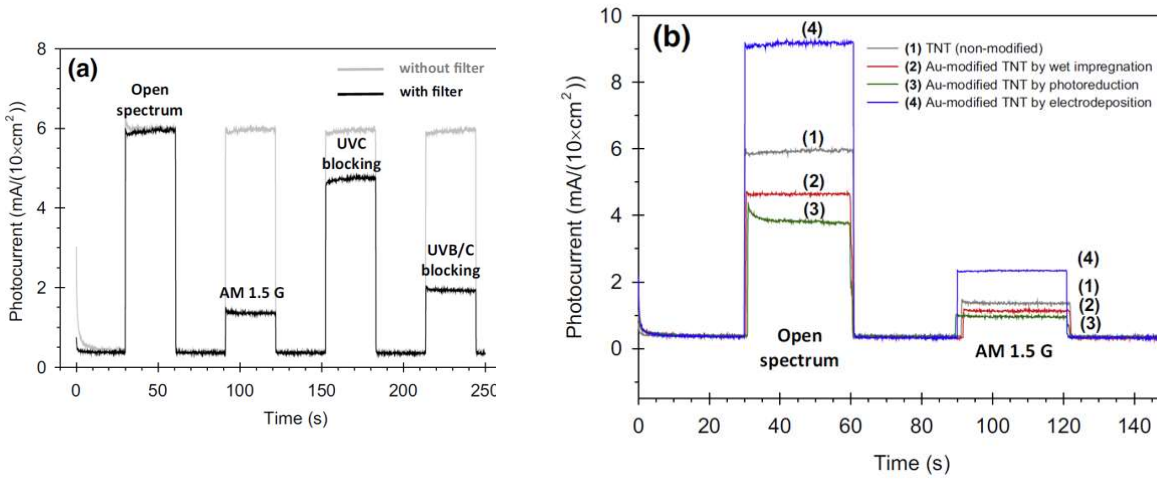

A ***B***

Figure 4.5: Chronoamperometric measurements for (a) non-modified and (b) Au- modified TNT arrays (0.1 V, 1 M KOH).

4.4.2 TNTs/Au NP testing

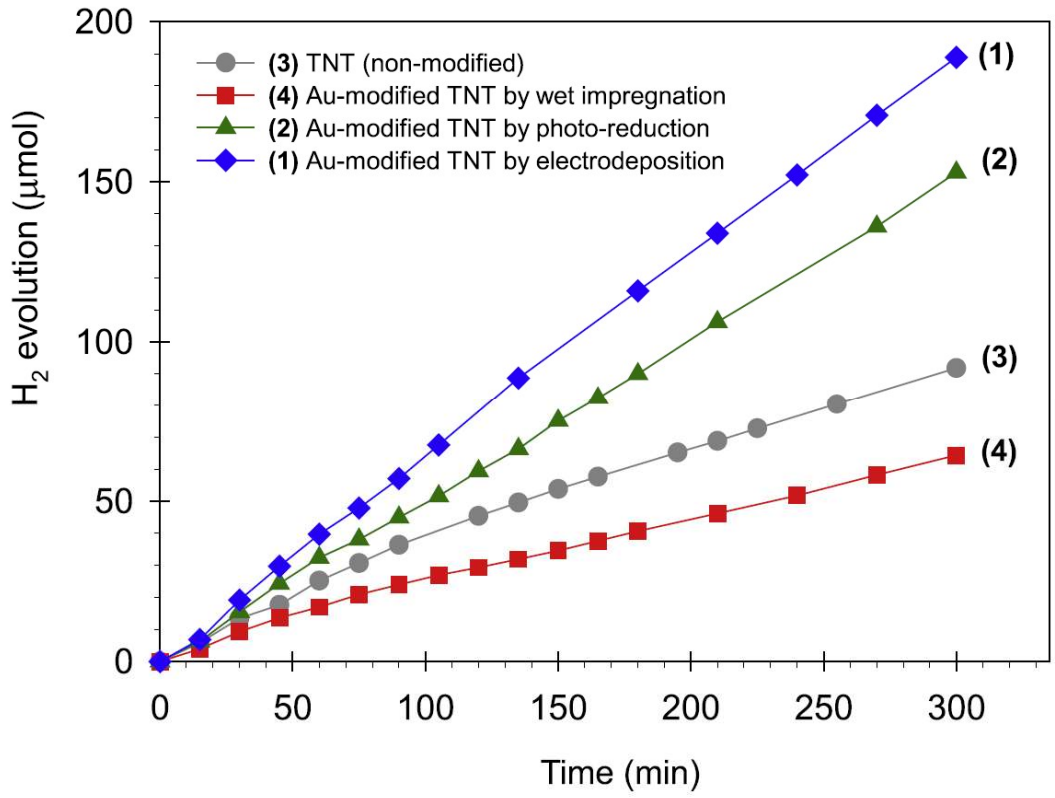

Figure 4.6: Hydrogen evolution as a function of time in gas-phase photo-catalytic experiments of ethanol photo-dehydrogenation over Au-modified TNT arrays.

H_2 productivity in gas-phase photo-reforming experiments (GP) of the different Au-modified TNT arrays was reported in figure 4.6. The maximum productivity of hydrogen was observed for the photo-catalyst prepared by electrodeposition, giving about 190 µmol H_2 in 5 h of light irradiation, followed by the sample prepared by photo-reduction technique with a 19% lower production. This difference can be related to the larger particles obtained by photoreduction with respect to electrodeposition technique, as confirmed by SEM analysis. A decrease of the performance with respect to the bare TNTs sample was observed for the Au modified TNT prepared by wet-impregnation. The bigger particles, acting as charge recombination centers and partially covering the surface area, played a negative effect on the H_2 production. Even if the process that occurs in the GP reactor is manly photocatalytic, the reaction occuring in the single modified tube can be considered as a short circuit type electrochemical cell. The figure 4.7 schematizes this concept: TNT arrays work as the anode for the oxidation reaction and the Au NPs work the cathode for the proton reduction. The holes, created in TNTs during light

irradiation, oxidize ethanol to acetaldehyde (and/or water to O_2), while the electrons are attracted by Au NPs combining with protons coming from the ethanol deprotonation.

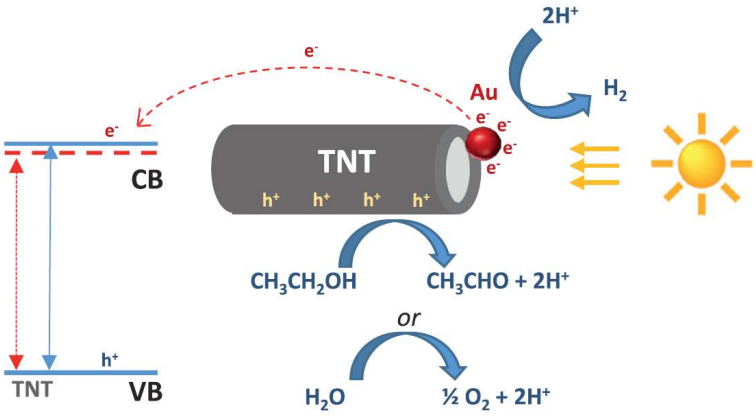

Figure 4.7: Schematic mechanism of water photo-electrolysis and/or ethanol photo- dehydrogenation over Au-modified TNT arrays with both redox reactions occurring in the same environment.

Selectivity of the reaction to acetaldehyde is above 98% and thus this reaction, which may likely be extended to other types of alcohols or possible other types of substrates, can be a good example of solar-driven chemistry.

For the tests in the PECa cell, the Au-modified TNTs by electrodeposition were chosen and tested for both water splitting (WE) and ethanol photo-dehydrogenation (DE); a comparison was made with the non-modified TNTs arrays. The results, reported in Figure 4.8, showed that about 195 µmol of hydrogen were measured in the cathode side after five-hour time of irradiation for the non-modified TNT, while no H_2 was detected in the anode part. This value is almost twice of that obtained in GPR reactor for ethanol dehydrogenation (about 92 µmol). The addition of ethanol to the photo-anode increasing the H_2 productivity even to about 355 µmol (four times higher). These results evidencing the importance of using a PECa design. The presence of Au NPs on TNTs surface decreased the quantity of H_2 at the cathode to about 93 µmol, but hydrogen was also formed at the photo-anode. This phenomenon is because the Au NPs can also act as reduction centers in the anode side in a process quite similar to that of GP reactor (figure 4.7). This was confirmed by the detection of H_2 in the anode side.

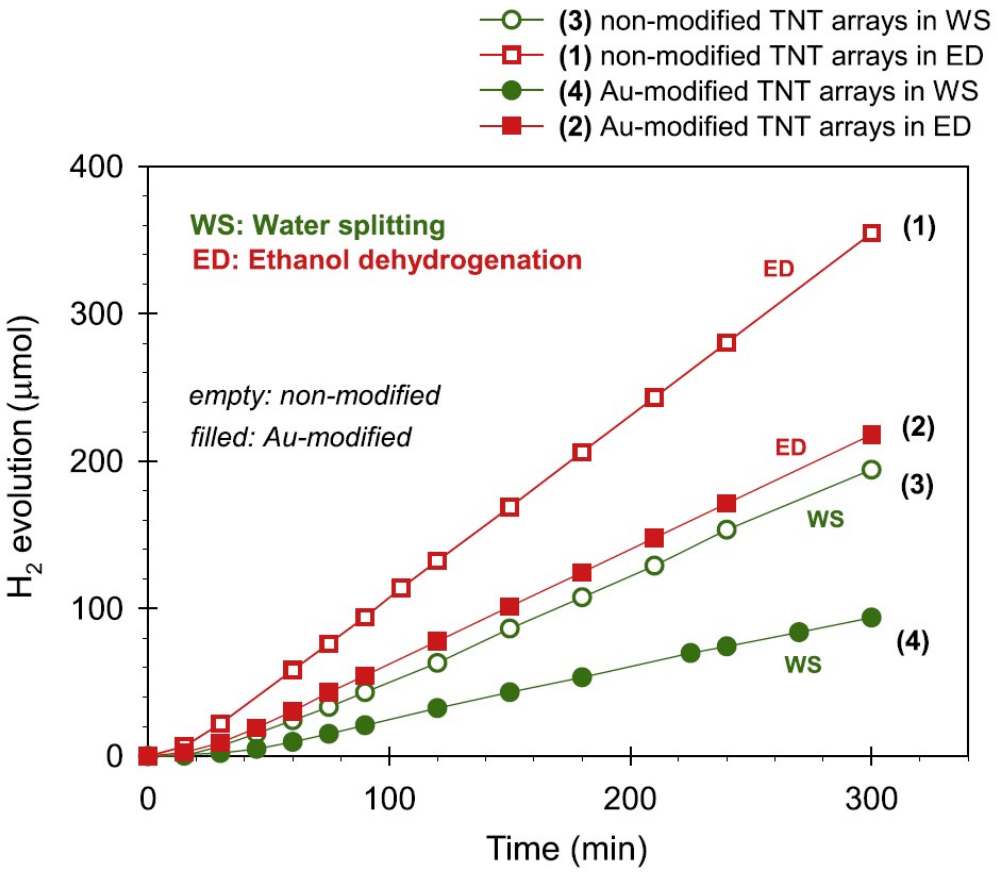

Figure 4.8: Hydrogen evolution as a function of time from the cathode of a PECa cell in water splitting (WS) and ethanol dehydrogenation (ED).

The tests conducted by using the filter AM 1.5 G to simulate the solar spectrum (figure 4.9) showed a similar behaviour of that conducted at open spectrum (figure 4.8). Some considerations should be done about the ratio of AM1.5 G/open spectrum values for the different photo-catalysts. This ratio is about 16% for the non-modified TNT arrays by water photo-electrolysis and increases to about 18% in presence of Au NPs, as gold improves light absorption in the visible region. The percentages increase in presence of ethanol, becoming ~21% and ~25% for the non- and Au-modified TNT arrays, respectively. Differently from the gas phase reactor, in the PECa approach, in the anode side the electrons and protons were generated and later transported to the cathode side (through a Nafion membrane for protons and through an external wire for electrons) when the reduction reaction occurs. The reduction/oxidation products of WS and/or ED are thus produced separately in the two reaction chambers.

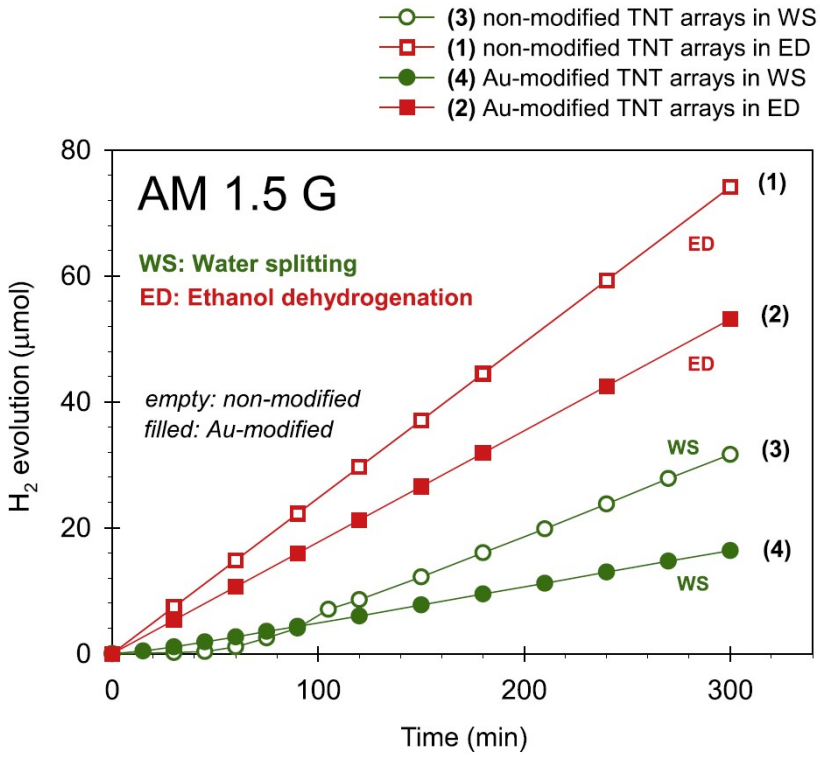

Figure 4.9: Hydrogen evolution as a function of time from the cathode of a PECa cell in water splitting (WS) and ethanol dehydrogenation (ED). AM 1.5 G filter was used to filter the incident light.

Figure 4.10 shows a schematic mechanism of water splitting (or ethanol photo-reforming) over Au-modified TNT arrays as photo-anode in a PECa. The presence of vertically aligned TNT arrays is necessary, in addition to the plasmonic–photonic synergetic effects discussed before, to improve the transport of electrons and protons (produced from water photo-oxidation) from the top of the tubes to the bottom part to be collected from the Ti porous layer (to be transferred through the external circuit to the cathode side) or to be transferred to the cathode side via the H^+ conductive membrane (Nafion-type) to the electrocathode. It is clear that the main advantage of this cell is to have a separate zone for oxidation and reduction thus improving the collection of the products and limiting the recombination of charge.

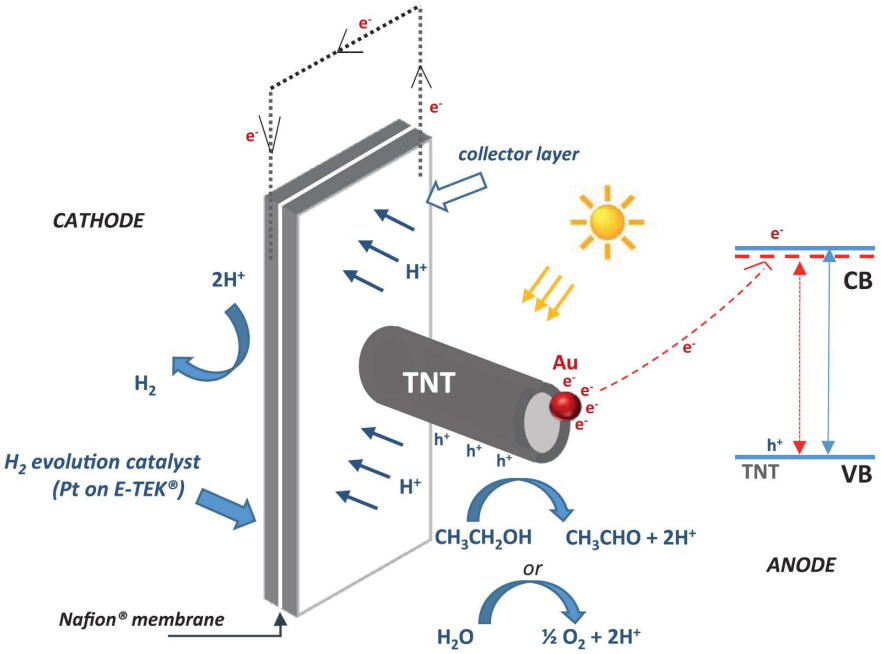

Figure 4.10: Schematic mechanism of water photo-electrolysis and/or ethanol photo-dehydrogenation over Au-modified TNT arrays as photo-anode in a PECa cell with separation of oxidation and reduction zones.

4.4.3 TNTs/Au NP efficiency

The main aspects to be considered for the evaluation of PECa cell efficiency are: i) the absorption of photons having sufficient energy to equal or exceed the band gap of the semiconductor; ii) the conversion of absorbed photons into separated charges and iii) the utilization of these charges for water splitting and/or ethanol photo-reforming.

The evaluation of these three main aspects can be included in a single parameter: the solar-to-hydrogen efficiency (STH), which has already introduced in chapter 3. The values of STH efficiency, obtained by testing Au-doped TNT electrodes in both WS and DE processes, are reported in table 4.2. In absence of sacrificial reagents (water photo-electrolysis), the maximum value of STH efficiency was obtained for the non- modified TNT sample (in this case the TNTs were prepared in 5 h of anodization). It is difficult to make comparison with other results reported in literature, because the reported photo-devices are very different in terms of materials, configuration, and operating conditions, as well as different expressions are generally used for efficiency calculation.

Process	***Sample***	***STH (%)***	***Filter***
Water photoelectrolysis	TNT arrays	0.83	Open spectrum
	TNT arrays	0.23	AM 1.5 G
	Au-TNT arrays	0.39	Open spectrum
	Au-TNT arrays	0.11	AM 1.5 G
Ethanol photo-dehydrogenation	TNT arrays	1.43	Open spectrum
	TNT arrays	0.24	AM 1.5 G
	Au-TNT arrays	0.93	Open spectrum
	Au-TNT arrays	0.20	AM 1.5 G

Table 4.2: Solar-to-hydrogen (STH) efficiency for non- and Au-modified TNT arrays in PECa cell.

The results obtained in the PECa system (with separation of oxidation/reduction zones) showed a different behaviour with respect to the experiments performed in gas phase (GPR). In these latter tests, in fact, H_2 production was higher in presence of Au NPs, while in PECa cell experiment the performances of the non-modified TNT sample, in terms of both H_2 production and STH efficiency, are higher. This phenomenon can be explained by the fact that the photo-generated current was partially short-circuited towards the Au NPs, which are deposited on the TNT electrode surface in the anodic side. For this reason, a good amount of the electric current was not collected and transferred to the cathode side, but it was lost in the anode in form of H_2 that can be easily recombine with O_2. This hypothesis is confirmed by the detection of hydrogen also in the anode side of the PECa cell. It is to be noticed that the amount of H_2 produced from the anode side has not been taken into account for the STH efficiency calculation.

Sample	***η (%)***	***Filter***
TNT arrays	61	Open spectrum
TNT arrays	50	AM 1.5 G
Au-TNT arrays	91	Open spectrum
Au-TNT arrays	56	AM 1.5 G

Table 4.3: Faradaic efficiency (η) for non- and Au-modified TNT arrays in PECa cell by water photo-electrolysis.

The Faradaic efficiency (equation 3.3) were reported in table 4.3 and shows the values for the Au-modified TNT arrays prepared by electrodeposition in comparison with the non-modified TNT sample for the process of water photo-electrolysis. All these values closed within 5% of error determination. Notwithstanding STH efficiency is higher for the non-modified TNT arrays, due to less H_2 production rate for Au-modified TNT samples at the cathode side, Faradaic efficiency is higher when gold is present, especially for tests performed at open spectrum. This is to ascribe to the reduced charge recombination phenomena (in TNT lattice) when Au NPs are present on the top surface of the tubes. This effect is more evident at open spectrum, as the charge recombination between electrons and holes mainly refers to the conduction and valence bands of titania, working better if irradiated in the ultraviolet region. These results well evidenced how PECa performance and efficiency depend not only on the properties of the photo-active materials, but also on the design of the PECa device in which the catalysts are tested.

4.4.4 TNTs/Cu NP characterization

After the study of the influence of gold nanoparticles deposited onto titania nanotubes, the attention was shifted to the possibility to use a non-noble metal: copper (Cu). For the deposition of Cu nanoparticles (Cu NPs) three techniques were investigated: 1) electrodeposition, 2) preformed (size-controlled) Cu nanoparticles and 3) dip coating.

***1) Electrodeposition*:** SEM images of the TNT-array thin film prepared by electrodeposition are reported in figure 4.11. After 1 cycle of deposition (figure 4.11a) big particles appear on the surface of the TNT with an average 60–100 nm diameter. After seven cycles (figure 4.12b), cubic-shaped copper nanoparticles (average size of 200 nm) cover the entire surface, forming in some cases also larger agglomerates. Using the electrodeposition method, even at the beginning of the process, nanoparticles larger than the TiO_2 nanotube size form and thus remaining deposited on the external surface of the TNT electrode. For more extended electrodeposition, the copper nanoparticles grow forming well cubic-shaped particles, which totally cover the surface of the titania nanostructure.

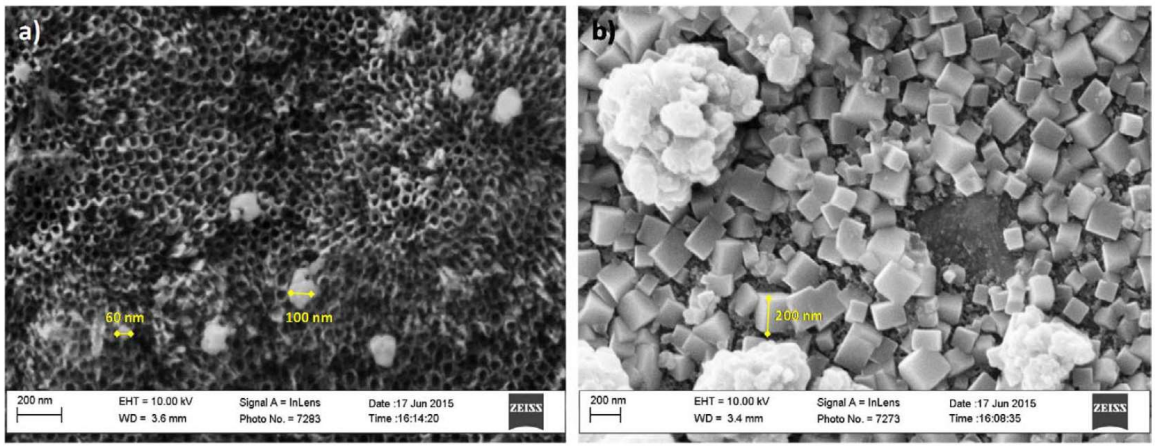

A ***B***

Figure 4.11: SEM images (top view) of copper deposed over TNT-array thin film by electrodeposition: (a) after 1 cycle, and (b) after 7 cycles.

2) Preformed Cu0 nanoparticles: Figure 4.12 shows the TEM images of the Cu NPs prepared by reduction of sodium borohydride in a basic solution in the presence of PEG. The images well evidence the presence of are very small particles (2–4 nm range), with uniform size and with a narrow distribution. SEM images of the deposited Cu NPs into the titania nanotubes evidence a completely different situation with respect to electrodeposition. Copper particles are evident on the surface of the TNT-array thin film but the EDX mapping (figure 4.13b) evidence their presence and well uniform distribution. The confirmation of the presence of small Cu nanoparticles was made by analysing this sample by TEM with high-magnification. Figure 4.14 shows the presence of small Cu NPs (average size 3 nm) homogenously distributed on the titania nanotubes. The Cu NPs retain the very narrow size distribution of the initial separate preparation. Changes in the loading of the particles into TNT was observed by preparing two TNT-array thin films at different time of anodization (1h and 3 h), with increasing thickness (1.3 and 2.9 μm for 1 and 3 h anodization, respectively): the average particles diameter remains the same, but the copper loading increasing from 0.15% for 1 h-anodized TNT to 0.37 wt%, for TNT anodized for 3 h. There is a good homogeneous distribution in both cases of the Cu NPs, without evidences of preferential surface deposition at the top surface of the nanotubes in the TNT-array thin film. By performing the spray coating technique, it was possible to increase the copper loading to 1 wt% maintaining a high copper dispersion.

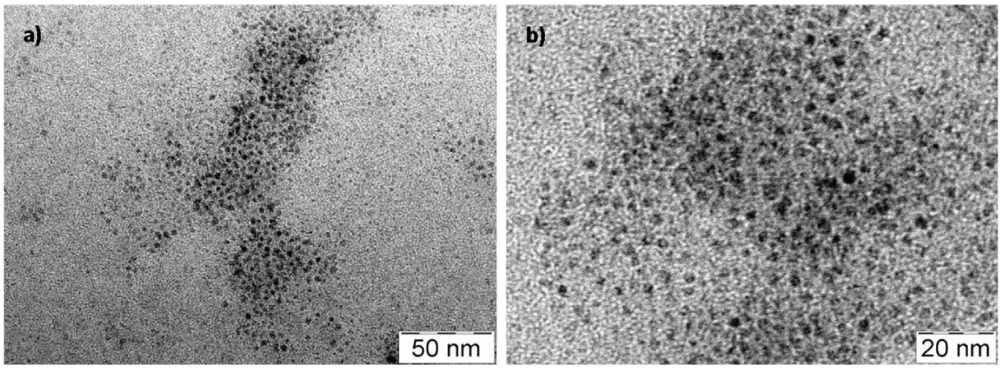

A ***B***

Figure 4.12: TEM images at different magnifications of copper nanoparticles prepared by reduction with sodium borohydride in a basic solution in the presence of PEG

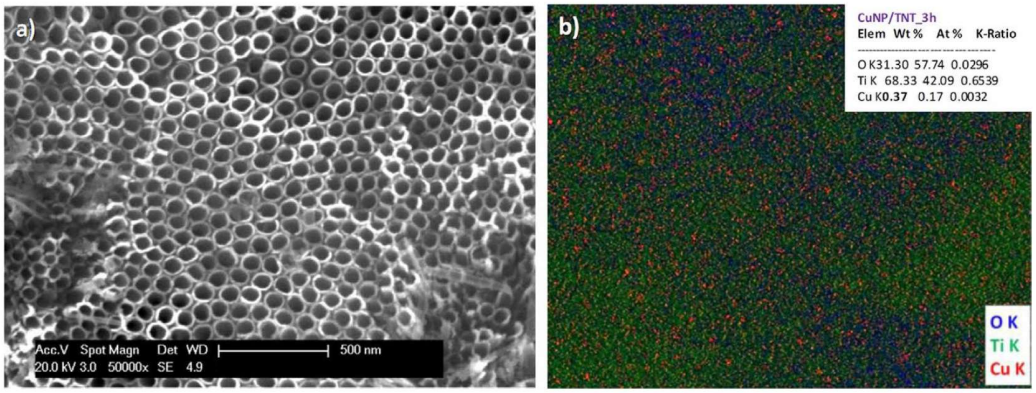

A ***B***

Figure 4.13: (a) SEM images (top view) of Cu NPs deposited on a TNT-array thin film (obtained by 3 h anodization). (b) EDX analysis of Cu NPs supported on TNT-array thin film anodized for 3 h.

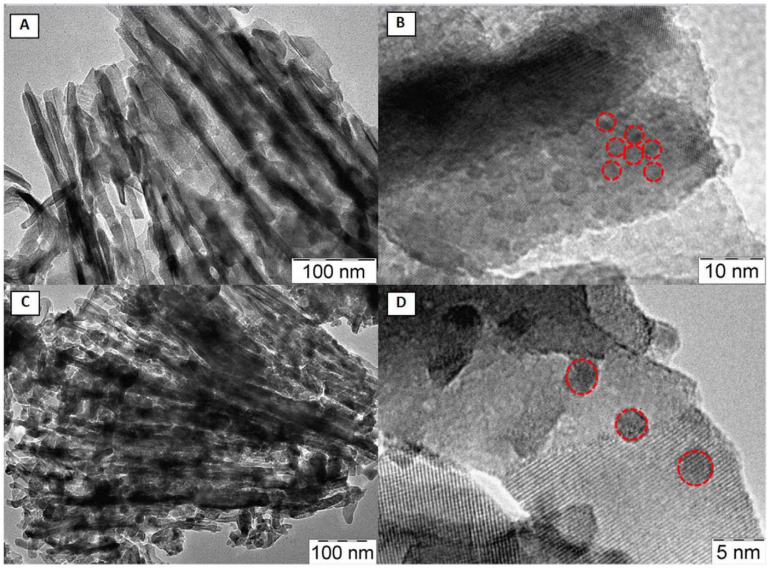

Figure 4.14: TEM images (A–D different magnifications) of Cu NPs supported on TNT-array thin film anodized for 3 h. In red in Fig. 4B and C the copper nanoparticles are evidenced.

UV–visible diffuse reflectance spectra of the Cu NP TNT samples are reported in figure 4.15. The base TNT-array thin film (spectrum 2) and a TiO_2 sample (P25 Degussa, about 80% anatase form and 20% rutile form) have also been reported as references. The TiO_2 P25 shows the classical spectrum of titania, with almost no absorption above 400 nm but a strong absorption below 400 nm (band gap around 3.1 eV) resulting from electron transitions from the valence band to the conduction band (O^{2-} to Ti^{4+}). TNT-array thin film, as already seen in Chapter 3, shows an intense and broad absorption in the visible region centered around 600 nm. The deposition of Cu NPs on the TNT-array thin film does not change significantly the spectrum, but in the case of Cu NPs, differently from Cu ED, the absorption intensity in the 400–500 nm range increases, proportionally to the copper loading. Cu_2O hollow nanoparticles show a relatively strong band around 434 nm attributed to the intrinsic band gap absorption (optical band gap energy of 2.22 eV). The increasing absorption in the 400–500 nm region could be thus attributed to the presence of very small Cu nanoparticles. This can be due to the slow oxidation of Cu^0 NP to Cu_2O and later to CuO, when the samples are exposed to air. The oxidation is enhanced upon calcination, which is required to eliminate also the organic complexing agent necessary to maintain well-dispersed copper nanoparticles.

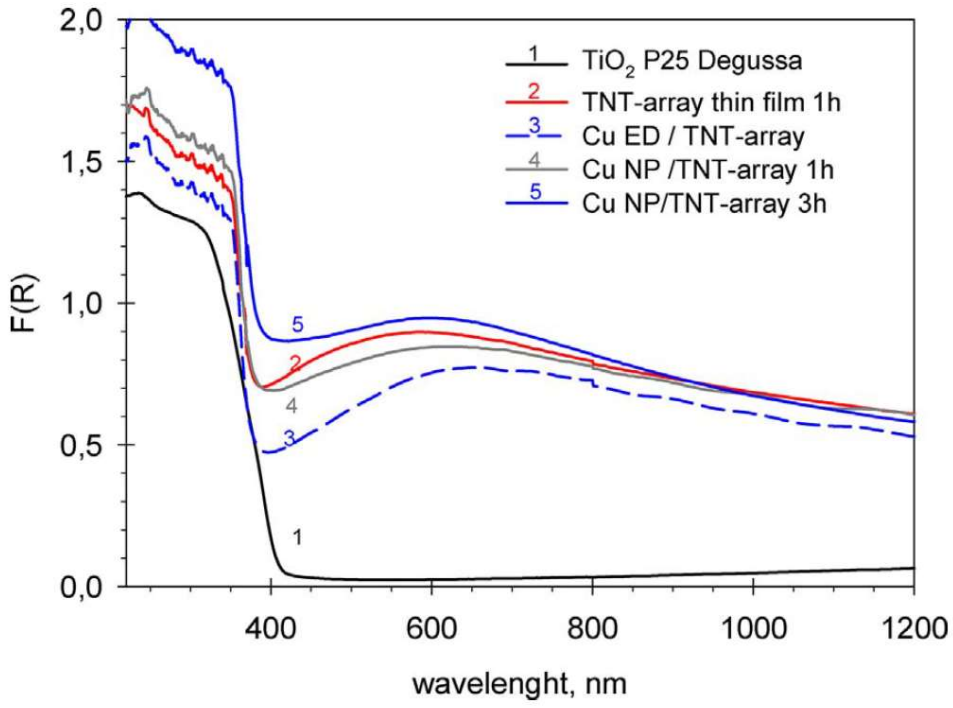

Figure 4.15: UV–vis diffuse reflectance spectra of (1) reference TiO_2 P25 Degussa and 2) TNT array 1h, 3) CuED/TNT, 3) CuNP/TNT 1h and 3) CuNP/TNT 3h.

Figure 4.16 reports the UV–visible reflectance spectra of Cu NPs/TNTs deposited by in-situ reduction, in comparison with that prepared by spray-coating (SC) of the preformed Cu NPs. The sample deposited by spray coating shows a slight shift of the broad maximum from 600 nm to 630 nm, making in this case more visible the presence of a shoulder (red arrow) centered to 460 nm. This tiny peak can be attributed to the presence of Cu_2O nanoparticles. The slight shift in the maximum of the broad absorption is due to the preferential deposition of Cu NPs at the top part of the TNT film (with formation of a multilayer), with a consequent slight change in the PGB (photonic band gap), which is very sensitive to TiO_2 NT inner diameter, wall thickness, and distance between the pores, as indicated before. After the calcination (450°C) there is a significant change in the spectrum (spectrum 3) with the broad band in the visible region shifting to 900–950 nm, due to the better crystallization of TiO_2, which slightly changes the titania wall thickness. Although a slight tail (centred around 420 nm) on the titania band gap edge could be observed, there is a clear decrease of the intensity of the band related to Cu_2O nanoparticles. This is reasonably due to the partial oxidation of these nanoparticles to CuO, evidencing the weakness of the optical band gap of Cu_2O. CuO nanoparticles, in fact, in the visible region show only the presence of weak d-d bands related to Cu^{2+} ions, centred at around 800 nm, but covered from the stronger PGB band of TNT-array. The presence of CuO nanoparticles, in the sample calcined at 450 °C, with a size in the range 10–20 nm was confirmed by TEM and XRD.

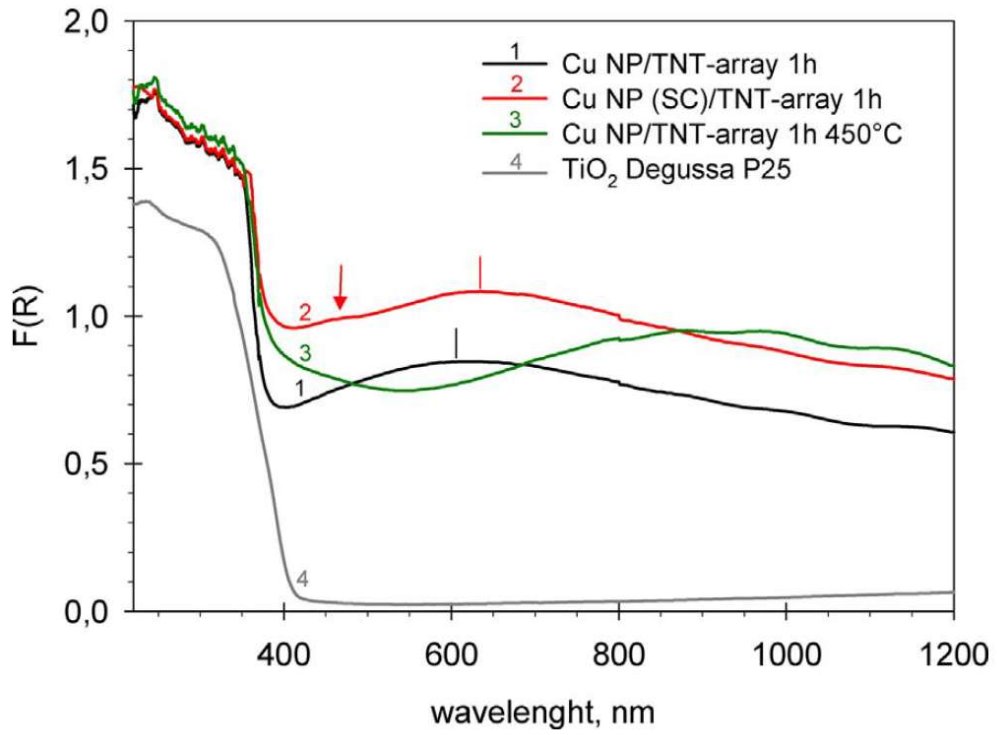

Figure 4.16: UV–vis diffuse reflectance spectra of (1) Cu NPs deposited by in-situ reduction on TNT-array thin film (1h anodization).

Figure 4.17 reports the photocurrent measurements for as prepared Cu/TNT-array thin films. The irradiance at open spectrum is around 0.1 mW cm^{-2} nm^{-1}. All the samples show a fast response to the light with a fast recovery of the initial value and a good reproducibility of the results in consecutive on-off cycles. The irradiance spectra of the all cut-off filters used are reported in figure 4.18 while the total irradiance value is reported in table 4.4. By using the UVC blocking filter (green curve), all the light below 300 nm is blocked, this results in a slight decreasing of the photocurrent response while by using the UVC/B the decreasing of the photocurrent response is quite higher because this filter blocks the light below 400 nm and a portion of the visible region between 500 and 700 nm. Obviously the amount of energy provided, in terms of W cm^{-2} is different as shows in table 4.4.

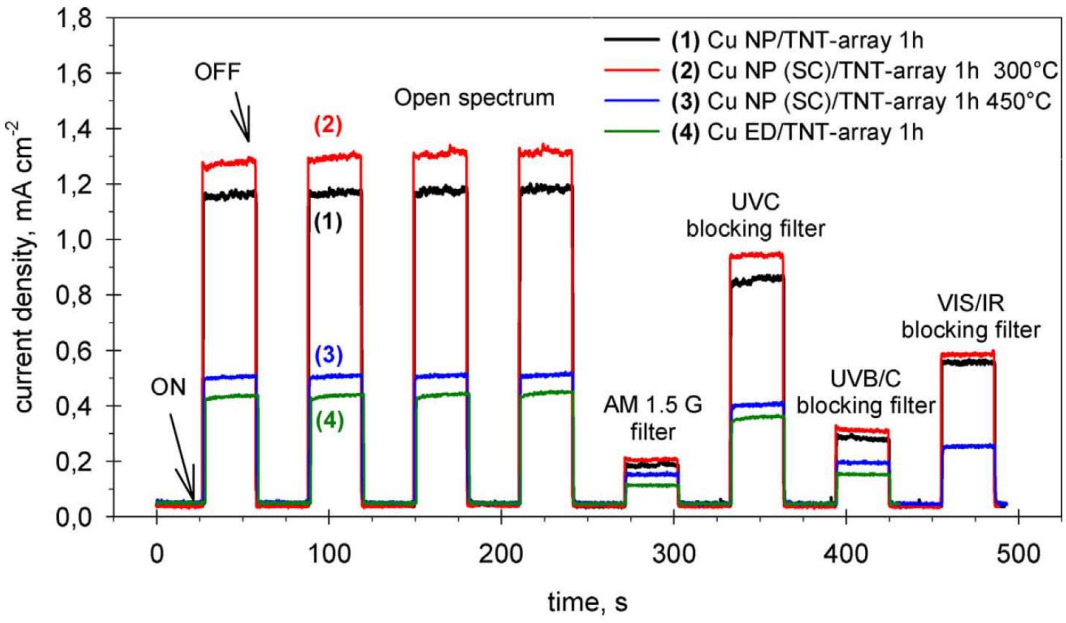

Figure 4.17: Chronoamperometry measurements (raw data) for different Cu/TNT-array thin films and application of different filters to solar simulator light.

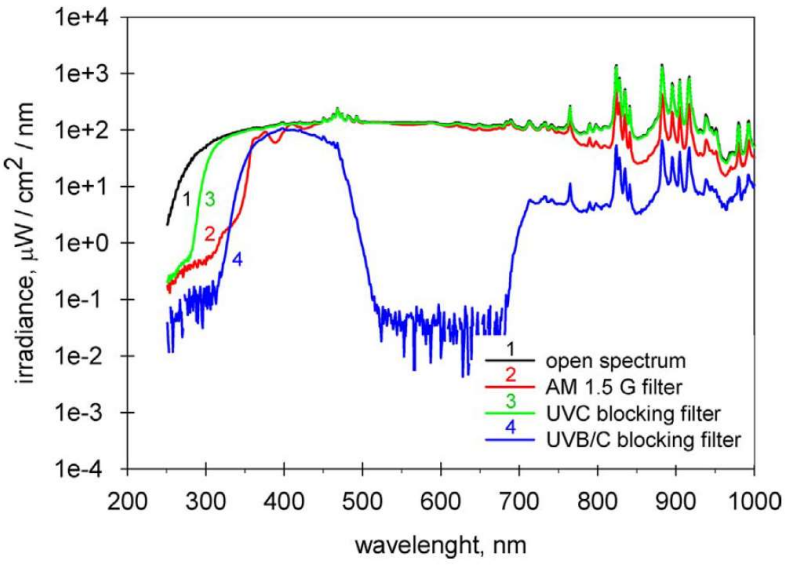

Figure 4.18: Irradiance spectra of solar simulator light with different applied filters

Filter	***Light irradiance W cm^{-2}***
Open spectrum	0.135
AM 1.5 G	0.088
UVC blocking filter	0.126
UVB/C blocking filter	0.018

Table 4.4: total light irradiance of the different filters

Normalization of the chrono-amperometry measurements to the total irradiance of the solar simulator light upon application of different filters, gives the results reported in figure 4.19. Due to the cut of blue components below 350 nm and 300 nm for the AM 1.5 G filter and the UVC blocking filter, respectively, the normalized current density results lower with respect to the open spectrum case. However, the UV B/C blocking filter, which cuts below 350 nm, but also above 500 nm (from green to red component) shows an enhanced normalized current density with respect to the open spectrum. This indicates that differently from what usually considered, i.e. that titania is active only with UV light below 300 nm, the light fraction in the 350–500 nm range is effective in producing photocurrent.

In all the cases, the TNT-array thin film results about 80% on the average more effective in photocurrent generation than an equivalent TiO_2 P25 thin film produced by spin coating. The effect of the presence of Cu NPs depends on both the method of deposition and the calcination treatment, which in turn influences the partial transformation of Cu_2O to CuO nanoparticles, as commented before. When large cubic-type copper-based nanoparticles (Cu ED/TNT-array 1h) or small Cu NPs, but mainly CuO-type due to calcination treatment (Cu NP (SC)/TNT-array 1h 450 °C), the behaviour is well comparable (or slightly worsen) than that of the reference TiO_2 P25 thin film, but less effective with respect to support (TNT-array 1h) without copper deposition. When Cu NPs are present mainly as Cu_2O, deposited either by in-situ reduction or by spray coating, the result is a quite comparable behaviour, or even slightly better, than that of the support (TNT-array 1h) without copper deposition, but definitively better than the reference TiO_2 P25 thin film.

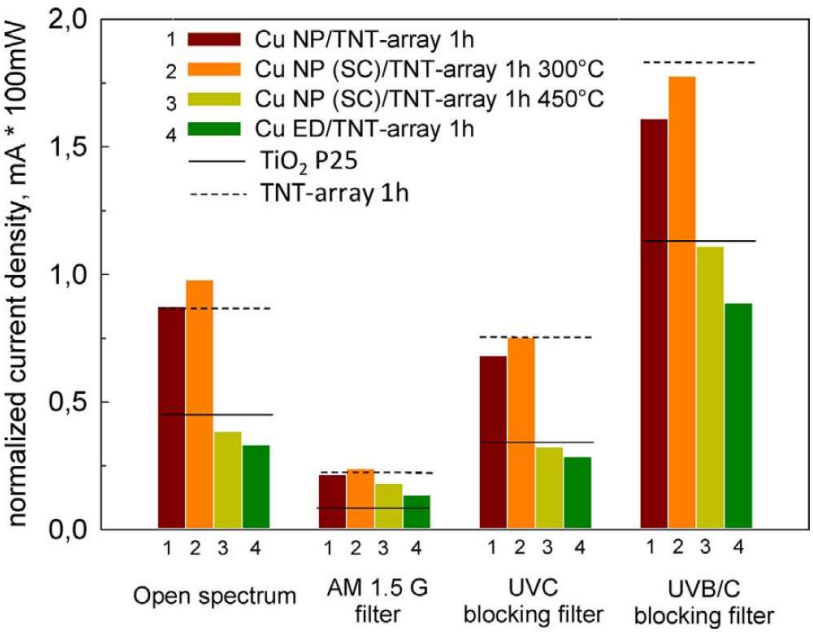

Figure 4.19: Normalized (to 100 mW) chronoamperometry measurements for different Cu/ TNT-array thin films and application of different filters to solar simulator light.

3) Dip coating: Figure 4.20 shows the FE-SEM images of TNT and CuO-TNT samples. It can be observed that there is an increment in the wall thickness that ranges from 27 to 36 nm after Cu deposition. The top view of un-modified TNT is showed in figure 4.20a indicating the presence of well-ordered TiO_2 nanotubes with wall thickness ranging from 20 to 27 nm and internal nanotube size in the 40–55 nm range. Through the use of the dip-coating technique the copper oxide was deposited around the TiO_2 nanotube wall (figure 4.20b). Cu nanoparticles are present mainly disposed around the tube wall (figure 4.20d). Some Cu nanoparticles with size between 18–33 nm are present on top of the TiO_2 nanotubes as evidenced by figure 4.20c. The effective Cu loading was obtained by AAS, with a procedure similar to that used for Au, and resulting to be about 9 wt.%. The presence of small Cu nanoparticles was confirmed by high resolution TEM image (figure 4.21a), which reports the presence of a TiO_2 nanotube with small CuO nanoparticles of about 2 nm decorating the internal walls of the nanotube (yellow arrow in figure 4.21a). Figure 4.21b also shows the presence of titania nanosheets with distance of 3.63 Å plane (101) as expected, as well as the presence of CuO from the lattice spacing of plane (111) measured as 2.43 Å.

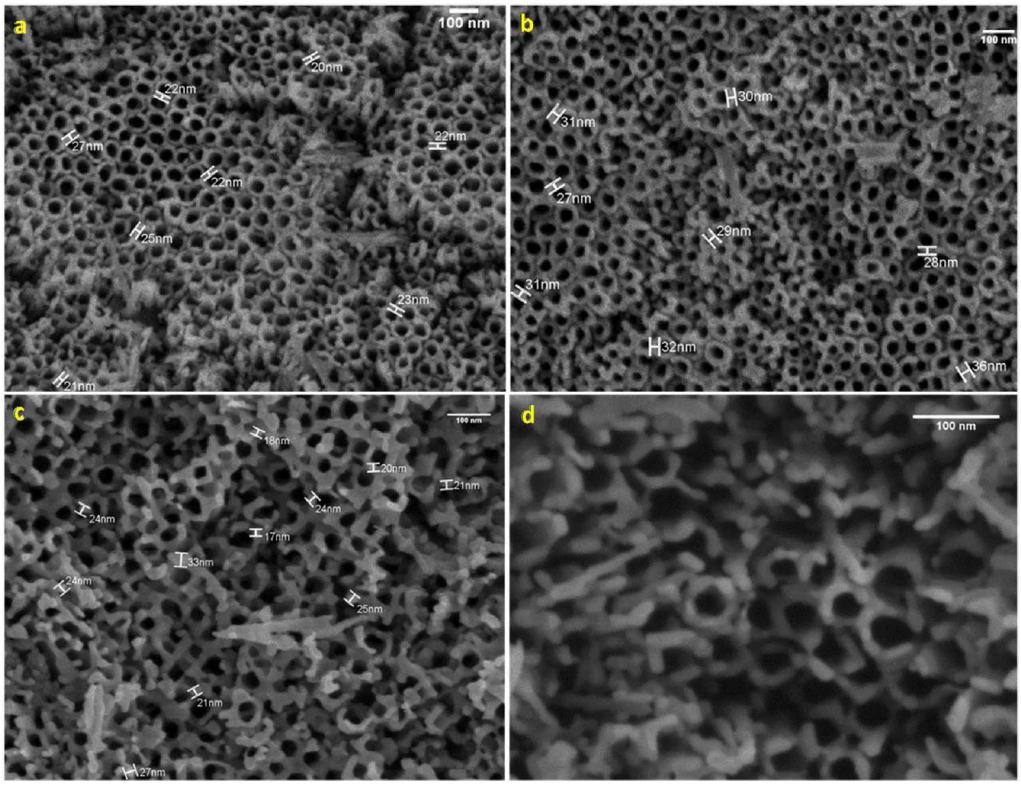

Figure 4.20: FE-SEM image of TiO_2 nanotubes without modification (a) and TiO_2 nanotubes decorated with CuO nanoparticles at 50000 (b), 100000 (c) and 200000 times (d) of magnification.

UV-visible diffuse reflectance spectra (with the calculation of the band gap energy for the materials) are reported in figures 4.22a and b respectively. Tauc's graphic was obtained by using the Kubelka-Munk function, according to the equation 4.1:

$$\alpha = (1 - R)1/\gamma/2R \qquad (4.1)$$

where α is the material absorptivity and R being the reflectance. The γ was assumed as two (indirect electronic transition allowed) once this is the electronic transition more suitably indicated for both the TiO_2 and CuO. The band gap for TiO_2 nanotubes (3.2 eV) corresponds to that typically reported for anatase TiO_2. A shift in the band gap energy to around 2.8 eV was observed for CuO-TNT. However, the clear tail in the absorption edge of band gap is an indication of the presence of Cu_2O nanoparticles, evidencing an additional band gap energy of about 2.0 eV, in accordance with what reported in literature for Cu_2O [12].

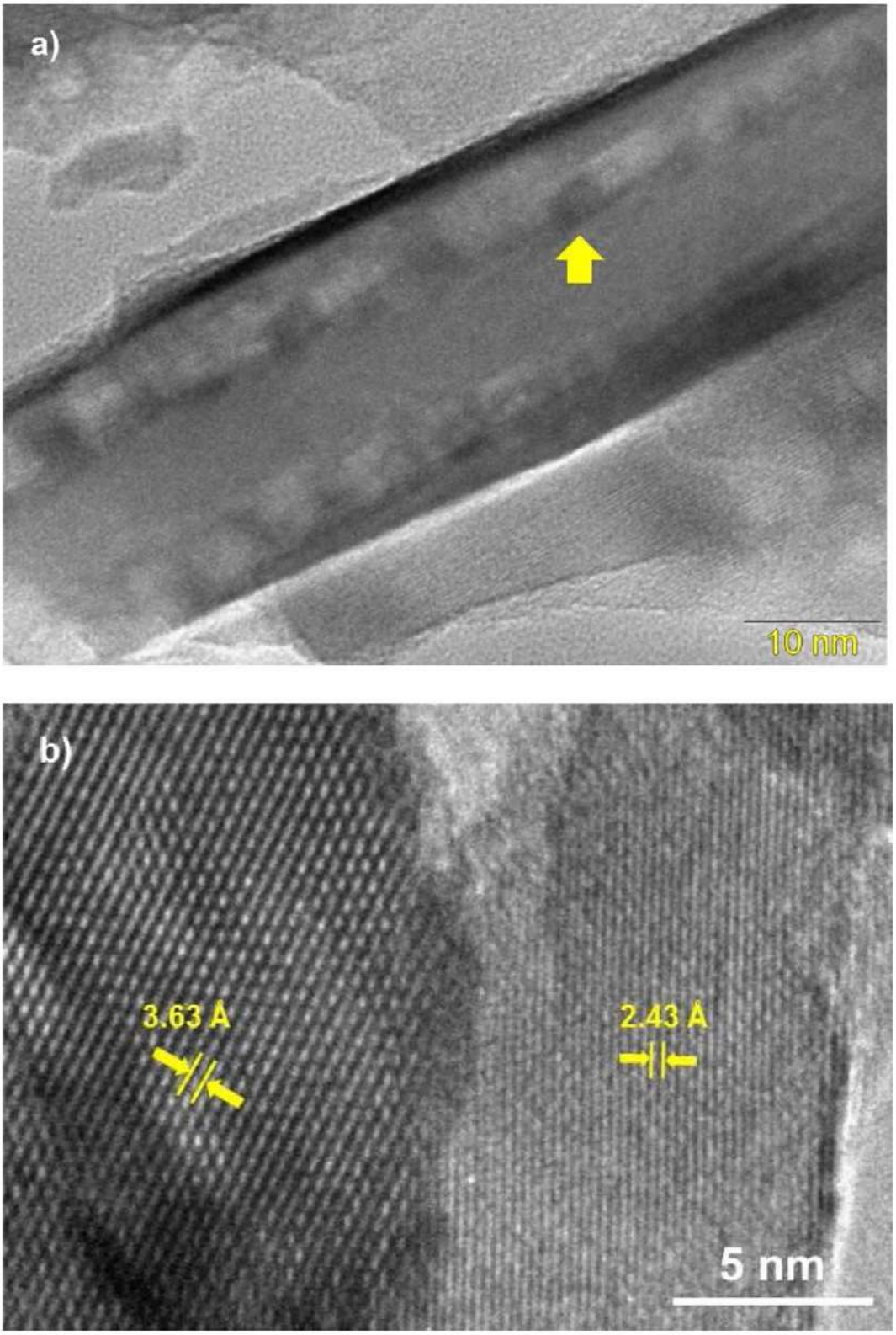

Figure 4.21: TEM images of CuO-TNT sample showing: a) a TiO_2 nanotube decorated in the internal walls with CuO nanoparticles (one evidenced by an arrow) and b) the lattice planes of TiO_2 and CuO.

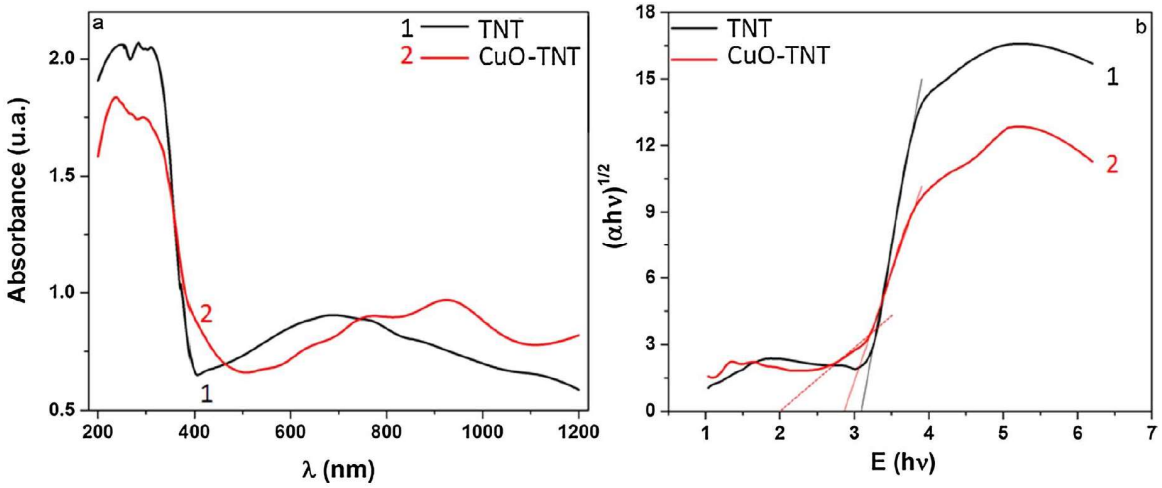

Figure 4.22: a) Diffuse reflectance spectrum in the UV–vis region of TNT (black line) and CuO-TNT (red line) and b) band gap energy calculated by Kubelka-Munk for TNT (black line) and CuOTNT (red line). The dashed red line indicates an additional band gap edge related to Cu_2O.

XRD results for CuO-TNT sample were reported in figure 4.23a. The XRD pattern confirming the presence of crystalline anatase TiO_2 phase and CuO crystallites, in addition to the background signal of Ti relative to the metallic titanium substrate of the electrode. With respect to relative intensities of reflections in TiO_2 anatase, the reflections corresponding to (002) plane are slightly intensified with respect to the more intense (101) reflection. This corresponds to TiO_2 crystals slightly elongated along this crystalline plane and exposing preferentially {001} facets. The XRD of CuO phase corresponds instead to that expected for CuO nanoparticles with monoclinic structure. The presence of Ti, Cu and O were further confirmed from the EDX analysis (figure 4.23b). The XPS spectrum reported in figure 4.23 evidenced the Cu 2p3/2 and Cu 2p1/2 peaks at 933.5 eV and 952.4 eV, respectively, which are related to the presence of CuO. No signals of Cu_2O were detected, probably because only a small amount of Cu_2O nanoparticles are present and they are under the detection limit of the instrument.

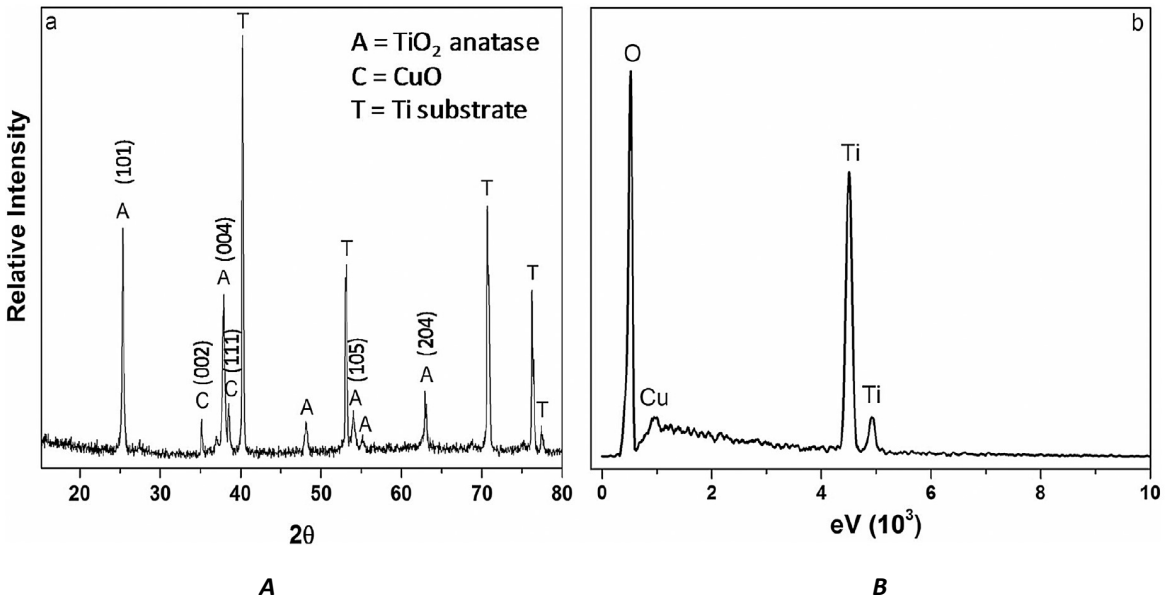

Figure 4.23: CuO-TNT: a) XRD pattern where A represents anatase phases of TiO_2, T represents the metallic titanium used as substrate and C represents the CuO peaks and b) EDX spectrum.

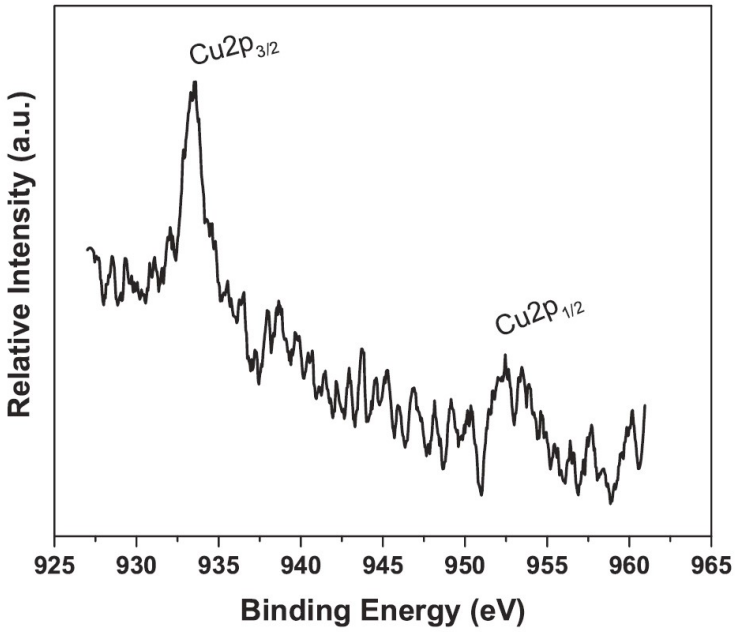

Figure 4.24: X-ray photoemission spectrum of CuO-TNT sample, showing Cu 2p3/2 and Cu 2p1/ 2 peaks related to CuO.

The chronoamperometric measurements were performed by using a three-electrode cell with 1.0 mol L^{-1} Na_2SO_3 as the electrolyte and an open and close light incidence system with and without the application of the solar filter AM 1.5 G (simulating standard terrestrial solar irradiance distribution).

The results have been normalized for 0.1 W cm^{-2} incident light irradiance. Figure 4.25a shows the ON/OFF cycles of the CuO/TNT sample, like the other TNT based electrodes, there is a stable and reproducible behaviour in several consecutive chronoamperometric cycles. Figure 4.25b shows an expansion of one of the chronoamperometric cycles, at open spectrum, to evidence better the differences between TNT and CuO-TNT samples. CuO-TNT samples show about 27% increase in normalized current density with respect to TNT with open spectrum and about 42% increase with AM 1.5G filtered light, even if the normalized current density in the latter case is about 23% of that of open spectrum. As reference, figure 4.25c reports the irradiance spectra for open spectrum and AM 1.5 G filtered light from solar simulator. The AM 1.5 G cuts essentially the light component before 350 nm; this means that about 75% of the photocurrent density derives from the UV light component and this is related to the band gap of TiO_2. The decoration of TNT with CuO leads to an enhancement of the normalized photocurrent density both with open spectrum and AM 1.5G filtered light, more intense in the latter case (42% increase with respect to 27% enhancement).

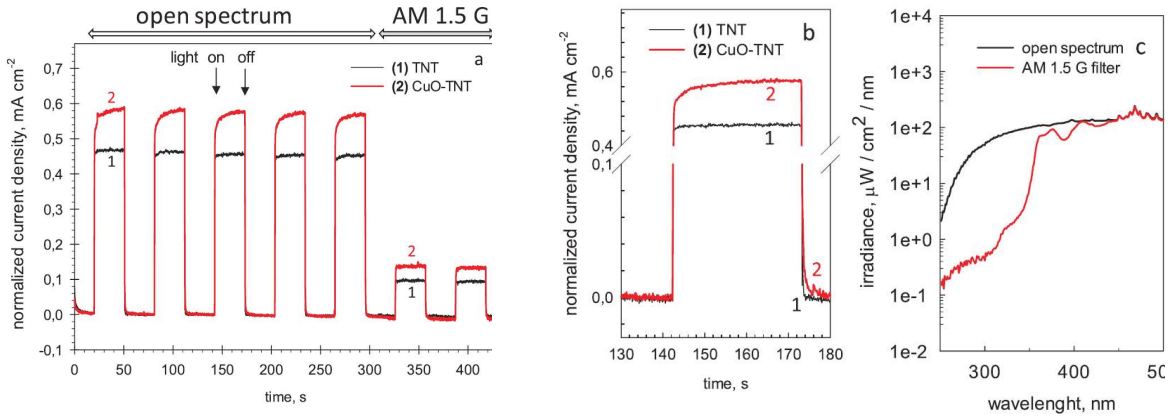

Fig. 4.25: a) Chronoamperometric measurements for TNT and CuO-TNT samples using open spectrum and AM 1.5G filtered light of a solar simulator. The data were normalized for 0.1 W cm^{-2} incident light irradiance. b) Expansion of one of chronoamperometric cycles. c) Irradiance for open spectrum and AM 1.5 G filtered light from solar simulator.

In the case of CuO-TNT, the current density reaches quickly about 85% of the maximum value, and then slowly further increases in the next 30–40s up to reach a constant value. The effect is well reproducible in consecutive cycles. When light is switched-off, there is instead a tail in reaching the background value in the case of CuO-TNT. The effect is not present in the case of AM 1.5G filtered light. The effect can be interpreted as a trapping of part of the

electrons with sufficient energy in heterojunctions created at the CuO-TNT interface, which leads to a partial delay in reaching steady current density. These trapped electrons are then released during switching off the light and are responsible for the tail.

4.4.5 TNTs/Cu NP testing

Like the study carried out for titania nanotubes modified with gold nanoparticles (TNT/Au NP), also the Cu NPs/TNTs electrodes were tested in two different reactions: ethanol dehydrogenation in gas phase reactor (GP) and water splitting into PECa cell (WS).

Gas phase experiments (GP): Figure 4.26 reports the results for the test performed in gas phase experiments (GP) for the samples 1) TiO_2 P25 thin film, 2) TNT-array 1h and 3) CuNP (SC)/TNT-array 450 °C. In the latter a calcination at 450 °C was necessary to have stable photocatalytic performances. The data shows a linear evolution of H_2 during the entire exposure to the light, with no deactivation within the 5 h of the experiments. No H_2 was detected at 0 time this means that the catalytic dark activity is zero under these experimental conditions. The best performance was obtained by the CuNP (SC)/TNT followed by the support alone (TNT) and the reference thin layer of P25 Degussa. Table 4.5 reports the rate constants of H_2 formation determined for these three photocatalysts and the photocurrent densities measured for the same samples.

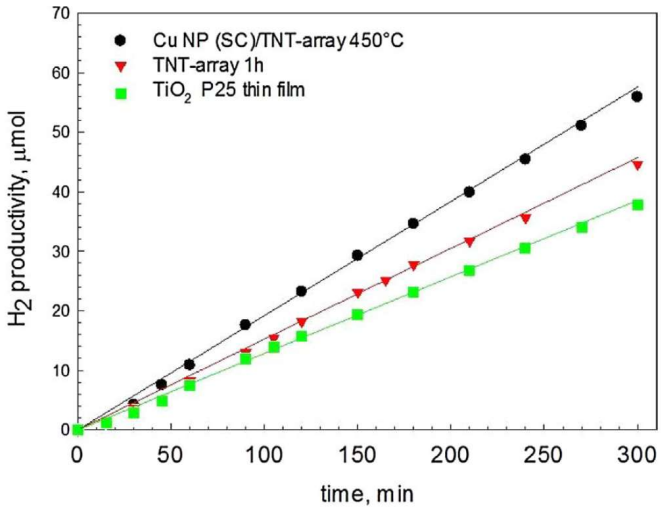

Figure 4.26: H_2 productivity as a function of reaction time in gas-phase reactor photocatalytic tests.

	Rate constant min^{-1}	Photocurrent density mA cm^{-2}
TiO_2 P25 thin film	0.135	0.64
TNT array 1h	0.152	1.21
CuNP(SC)/TNT 450°C	0.192	0.51

Table 4.5: Rates constant of H_2 production in gas-phase reactor photocatalytic tests and photocurrent densities.

The increase in the photocurrent generation of the TNT arrays with respect to reference TiO_2 P25 thin film was lower than 87%, while the increase in H_2 production rate is just the 19%. Cu NP (SC)/TNT-array 450 °C shows a 20% decrease in the photocurrent with a 42% increase in the rate constant of H_2 photo-generation. This absence of relationship could be ascribed of a direct co-catalytic role by the CuO nanoparticles in the photogeneration of H_2. The introduction of CuO nanoparticles creates a short-circuit-type electrochemical cell, with the TNT arrays being the anode for the oxidation reaction and the Cu NPs the cathode for the proton reduction, with a behaviour very similar to that already observed for the case of gold. The holes created in TNTs during light irradiation, oxidize ethanol (mainly to acetaldehyde), while electrons are moved to CuO NPs (due to lower conduction band energy with respect to that in TiO_2, although strongly depending on nanoparticle size and TiO_2 nanostructure) combining with protons coming from the ethanol deprotonation. The difference of performance in the case of CuNP (SC) TNT between photocurrent generation and H_2 production can be addicted to a distance effect: while for the photocatalytic experiment a short-distance effect exists, the case of photocurrent generation requires also the longer distance transport of the electrons to the collector substrate (Ti). During this transport, they may recombine with holes and decrease photocurrent density.

Photoelectrochemical water splitting (WS): the sample CuO/TNT prepared through dip coating was tested in the photo-electrochemical water splitting, following the procedure and using the PECa cell already described for the case of Au NPs/TNTs. In accordance with what observed in chronoamperometry results (figure 4.25), a stable current density was observed in these tests (figure 4.27a), with the current density higher for the case of CuO-TNT with respect to TNT. The small spikes observed in the current density are related to H_2 or O_2 bubbles

formation. The initial change in current density during about the first 10–15 min is related to the establishment of equilibrium in the PEC solar cell upon the start of the illumination.

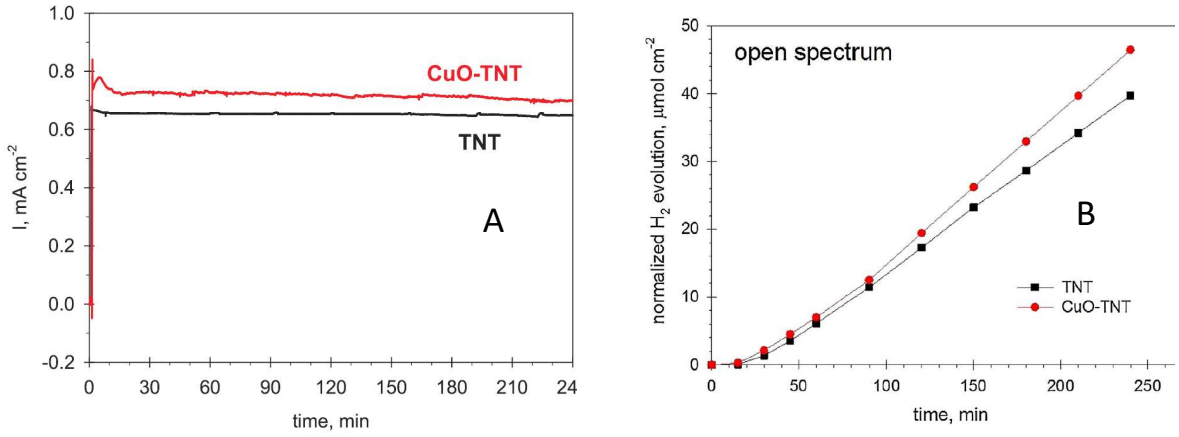

Figure 4.27: a) Current density generated applying open spectrum solar simulator light to TNT and CuO-TNT photoanodes in the compact PEC solar cell; b) Cumulative hydrogen formation as a function of time from the cathode of the PEC cell using TNT or CuO-TNT as photoanodes in tests with not-filtered light (open spectrum from the lamp) of a solar simulator.

Figure 4.27b reports the cumulative H_2 formation as a function of time in the compact PEC solar cell using TNT or CuO-TNT as photoanodes in tests with not-filtered light of a solar simulator (open spectrum). As commented for chronoamperometry tests, the data were normalized for 0.1 W cm^{-2} incident light irradiance. The initial apparent induction time is related to the establishment of the equilibrium in the PEC solar cell, as commented above. It is to be noticed that H_2 evolves at the cathode (on the commercial Pt/GDL electrode), but the modification in the photoanode (TNT, CuO-TNT) determines a different rate of photogeneration of H^+/e^-. There is a stable continuous production of H^2 for both TNT and CuO-TNT photoanodes within the investigated time period (about 4 h), indicating no deactivation. A parallel O_2 evolution from the other cell compartment, according to stoichiometry, was observed. Whereas an apparent increase in the rate of H_2 production from the first period (30–90 min) to the period from 90 to 250 min was detected, but this is related to establishment of equilibrium in the PEC cell. After about 90 min the rate of H_2 production (normalized for 0.1 W cm^{-2} incident light irradiance) is stable and equal to 11.32 and 13.64 µmol H_2 cm^{-2} h^{-1} for TNT and CuO-TNT, respectively. The rate is about 20% higher for CuO-TNT photoanode, which well corresponds to the increase in photogenerated current density determined either in-situ or in the separated chronoamperometry tests (figure 4.25).

Both the electrodes were tested under the application of the solar simulator filter (AM 1.5 G) (figure 4.28). The lower amount of photogenerated H_2 prolonged the initial apparent induction time. The normalized rates of generation of H_2 (after the initial time of about 90 min) are 1.56 and 3.43 $\mu molH_2\ cm^{-2}\ h^{-1}$ for TNT and CuO-TNT, respectively (normalized for 0.1 W cm^{-2} incident light irradiance). The increase in H_2 production in this case is about 120% with respect to TNT. This is more than twice the increment observed in current density (about 50%) observed during these tests and in chronoamperometric experiments (figure 4.26). However, the normalized H_2 production rate for CuO-TNT using AM 1.5G filtered light is about 25% of that measured for open spectrum, in well agreement with the observed relation between photocurrent and H_2 producition (already discussed in Chapter 3).

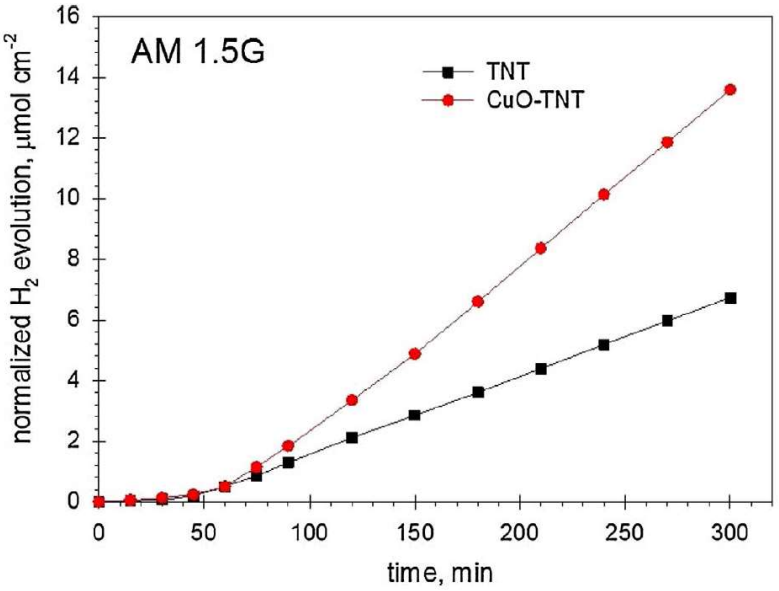

Figure 4.28: Cumulative hydrogen formation as a function of time from the cathode of the PEC cell using TNT or CuO-TNT as photoanodes in tests with AM 1.5G filtered light of a solar simulator.

4.4.6 TNTs/Cu NP Efficiency

By using a monocromator to select the single wavelength, it was possible to evaluate the quantum efficiency for CuO/TNT. Figure 4.29 shows the comparison between TNT and CuO/TNT for the external quantum efficiency (IPCE). Solar spectrum is also reported as reference (details about the equation used for IPCE calculation can be found in Chapter 3). Both TNT samples show a big peak in the UV region due to the well-known characteristics of TiO_2;

the presence of CuO nanoparticles onto TiO_2 nanotubes slightly increases IPCE in the 350– 390 nm spectral region, while it has essentially no effect at higher wavelengths.

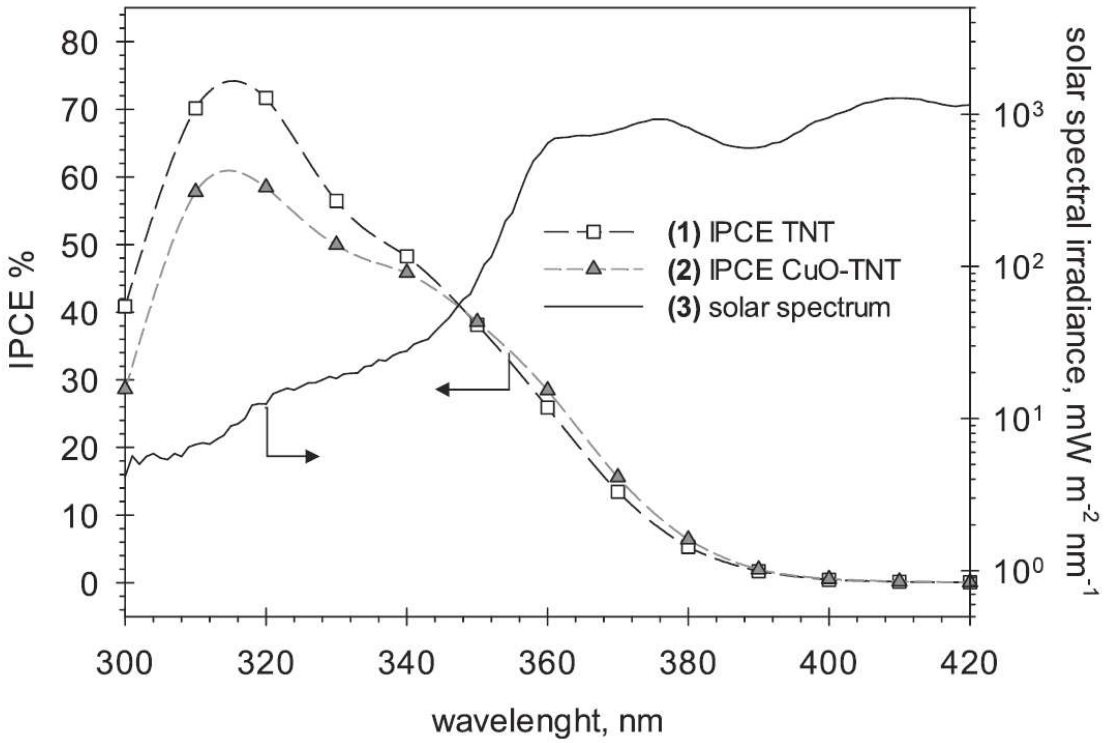

Figure 4.29: Incident photon to current conversion efficiency (IPCE) spectra of TNT and CuO TNT photoanodes tested in the PEC cell. The solar simulating spectral irradiance vs. wavelength is also reported.

It was also possible to calculate the solar-to-hydrogen (STH) efficiency, as discussed in Chapter 3, and the results have been reported in table 4.6. The STH efficiency of TNT is 1.68%, which increases to over 2% for CuO-TNT sample (about 20% increase) using not-filtered light (open spectrum) from the solar simulator. Using AM 1.5G filtered light the STH efficiency is lower, and increases from 0.24% to 0.53% moving from TNT to CuO-TNT.

Sample	Incident light	H_2 production rate μmol h^{-1}	STH efficiency (%)
TNT	Open spectrum	85.5	1.68
TNT	AM1.5 G	7.8	0.24
CuO-TNT	Open spectrum	104.3	2.04
CuO-TNT	AM1.5 G	17.4	0.53

Table 4.6: H2 production rate and solar-to-hydrogen (STH) efficiency for PEC cell using TNT and CuO-TNT photoanodes.

4.5 Conclusion

In this chapter, different strategies to improve the visible light absorbance characteristics of TiO_2 nanotubes have been studied, by depositing both noble (Au) and non-noble (Cu) metals nanoparticles on titania surface. The main achievements are summarized as follows:

1) ***Au nanoparticles:*** the deposition of gold nanoparticles was performed by three different techniques: 1) wet impregnation; 2) photoreduction and 3) electrodeposition. Characterization data of Au-modified TNT arrays prepared by electrodeposition evidenced small Au NPs (3–5 nm) well dispersed on top surface of highly ordered TNT arrays, providing a broad peak in the visible region due to both structural and surface plasmon resonance (SPR) effects. Au- modified TNTs prepared by electrodeposition also showed a slight shift of band gap towards the visible light region with respect to non-modified TNT arrays and the presence of interference fringes in UV–visible spectrum. The synergic effect between nanotubular structures of TiO_2 and uniformly dispersed Au NPs, as well as the synergy between plasmonic–photonic effects allowed to obtain good performance in terms of photo-generated current and H_2 production. Particularly, the deposition of Au nanoparticles by electrodeposition allowed to:
    - enhance the photocurrent response, being 1.6 times higher than the photocurrent obtained by the non-modified TNT arrays;
    - increase the hydrogen production rate in the gas-phase tests of ethanol photo-reforming (~60% higher than bare nanotubes).

2) ***Cu nanoparticles:*** in order to move to a cheaper economy and to the reduction of use of noble metals, Cu-based nanoparticles were deposited onto TNTs. Also in this case, three methods were performed: 1) electrodeposition, 2) spray coating of preformed NPs and 3) dip coating. Copper-based nanoparticles (Cu NPs) with average size of 3 nm, well dispersed over a TNT-array thin film were prepared by in-situ reduction with sodium borohydride in a basic solution using polyethylene glycol as spacing agent, or by preforming the Cu NPs with the same methodology, and then depositing these particles by spray coating over the TNT-array thin film. The presence of Cu^0 NPs allowed to:

- improve the H_2 photogeneration behaviour in gas-phase photoreactor experiments, even when their presence decreases the photocurrent generation.

The deposition of CuO nanoparticles in TNT thin films led to:

- photoanodes with improved photocurrent behaviour;
- increase H_2 generation by water splitting in a full PEC device;
- improve the solar-to-hydrogen (STH) efficiency.

The increase in STH efficiency was of about 20% with respect to the bare TNT photoanode using open spectrum light from a solar simulator and about 50% increase using standard solar irradiation (AM 1.5G filtered light).

4.6 References

[1] C. Ampelli, F. Tavella, S. Perathoner, G. Centi, *Engineering of photoanodes based on ordered TiO_2-nanotube arrays in solar photo-electrocatalytic (PECa) cells*, Chem. Eng. J. 320, 352–362 (2017)

[2] H. Pan, *Principles on design and fabrication of nanomaterials as photocatalysts for water-splitting*, Renew. Sust. Energy Rev. 57, 584–601 (2016)

[3] X. Chen, Z. Zhang, L. Chi, A.K. Nair, W. Shangguan, Z. Jiang, *Recent advances in visible-light-driven photoelectrochemical water splitting: catalyst nanostructures and reaction systems,* Nano-Micro Lett. 8 1–12, (2016)

[4] Y. Ma, X. Wang, Y. Jia, X. Chen, H. Han, C. Li, *Titanium dioxide-Based nanomaterials for photocatalytic fuel generations,* Chem. Rev. 114 9987–10043, (2014)

[5] C. Ampelli, F. Tavella, C. Genovese, S. Perathoner, M. Favaro, G. Centi, *Analysis of the factors controlling performances of Au-modified TiO_2 nanotube array based photoanode in photo-electrocatalytic (PECa) cells,* J. Energy Chem. 26, 284–294 (2017)

[6] P. Peerakiatkhajohn, T. Butburee, J.-H. Yun, H. Chen, R.M. Richards, L. Wang, *A hybrid photoelectrode with plasmonic Au@TiO_2 nanoparticles for enhanced photoelectrochemical water splitting,* J. Mat. Chem. A 3 20127–20133 (2015)

[7] J. F. de Brito, F. Tavella, C. Genovese, C. Ampelli, M. V. B. Zanoni, G. Centi, S. Perathoner, *Role of CuO in the modification of the photocatalytic water splitting behavior of TiO_2 nanotube thin films*, App. Cat. B: Envir., 224, 136-145, (2018)

[8] F. Tavella, C. Ampelli, L. Frusteri, F. Frusteri, S. Perathoner, G. Centi, *Development of photoanodes for photoelectrocatalytic solar cells based on copper-based nanoparticles on titania thin films of vertically aligned nanotubes,* Cat. Tod., 304, 190-198 (2018)

[9] J.F. De Brito, M. Valnice, B. Zanoni, *On the application of Ti/TiO_2/CuO n-p junction semiconductor: a case study of electrolyte, temperature and potential influence on CO_2 reduction,* Chem. Eng. J. 318 264–271 (2017)

[10] G.K. Mor, O.K. Varghese, R.H.T. Wilke, S. Sharma, K. Shankar, T.J. Latempa, K.- S. Choi, C.A. Grimes, *P-Type Cu-Ti-O nanotube arrays and their use in self-Biased heterojunction photoelectrochemical diodes for hydrogen generation*, Nano Lett. 8 1906–1911 (2008)

[11] L. Perazolli, L. Nuñez, M.R. Apolinário da Silva, G.F. Pegler, A.G. Cavalarri Costalonga, R. Gimenes, M.M. Kondo, M.A. Zaghete Bertochi, *TiO_2/CuO films obtained by citrate precursor method for photocatalytic application,* Mater. Sci. Appl. 2 564–571 (2011)

[12] M. Hara, T. Kondo, M. Komoda, S. Ikeda, K. Shinohara, A. Tanaka, J.N. Kondo, K. Domen, *Cu_2O as a photocatalyst for overall water splitting under visible light irradiation,* Chem. Commun. 357–358, (1998)

5 Tantalum Oxynitride nanotube arrays

5.1 State of the art

Many semiconductors show a band gap suitable to be used as photocatalysts in water photo-electrolysis. Theoretically, the band gap should be higher than 1.23 eV, as this is the energy (in standard conditions) needed for the reduction/oxidation half reactions for the production of H_2 and O_2, respectively. However, most of the semiconductors have a bang gap too high (e.g. TiO_2, band gap 3.0-3.2 eV) to exploit the visible part of the solar spectrum. Thus, the development of novel materials with improved properties in terms of visible light harvesting is needed.

In this context, tantalum oxynitride (Ta-oxy-N) based materials have recently received much attention as a class of attractive light absorbers to construct high-efficiency bias-free photoanodes for photo-electrochemical (PEC) water oxidation [1-2]. The relatively wide band gap of about 4.4 eV hinders Ta_2O_5 to be utilized as a visible light absorber, but Ta_2O_5 can easily be converted to Ta_3N_5, providing a band gap of about 2.1 eV and a theoretical maximum solar energy conversion efficiency of about 15.9% [3].

Tantalum-oxide-based materials have been fabricated by various methods, such as hydrothermal [4], vapour phase hydrothermal [5], sol–gel [6] and electrochemical anodization [7-9]. The properties of Ta-oxy-N catalysts can strongly be enhanced by adopting morphology control and nano-structuring methodologies. This makes the electrochemical anodization as the most suitable technique to prepare controlled nanostructured Ta-oxy-N [10-12]. 1-D nanostructures, in fact, show many advantages for PEC water photo-electrolysis (large surface area, high aspect ratio, direct electron transport with minor probability of charge recombination). The main advantage of these tantalum-oxy-nitride materials refers to their lower band-gap (in the range 1.9-2.5 eV depending on N loading) with respect to titania (3.0-3.2 eV), thus improving light absorption in the visible region [13-15].

5.2 Scope of the chapter

This chapter focuses on the development of photo-active materials different than TiO_2, in order to improve the absorption of visible light in PEC cells. In particular, highly ordered Ta-oxy-N nanotube arrays were synthesized by controlled anodic oxidation of Ta foils followed by nitridation with ammonia.

The anodization method can be described as a reconstruction of a thin Ta_2O_5 oxide layer (formed initially by oxidation of a Ta sheet), which occurs under the application of a constant voltage in the presence of fluoride-based electrolytes. The samples were anodized in a two-electrode electrochemical cell under the application of a constant bias (in the range 20-60 V) and in two oxidation steps. The synthetic procedure was optimized in order to obtain a stable and robust photo-catalytic layer. After the anodization, the Ta oxide nanotubes were treated at high temperature (600-900 °C) with ammonia to replace partially oxygen with nitrogen in the Ta_2O_5 lattice. The presence of nitrogen allows reducing the band gap of these electrodic materials, enhancing their visible light absorption properties, as well as limiting charge recombination phenomena.

The anodized samples were fully characterized by SEM-EDX, UV-visible Diffuse Reflectance Spectroscopy and Chrono-amperometry, to determine the structural and morphological properties of these photocatalysts, as well as their light absorption properties.

The main scope of the chapter is to find a correlation between the parameters using during the synthesis (applied voltage, anodization time) and the Ta-oxy-N nanostructures (nanotube diameter and length, wall thickness and grade of voids).

5.3 Experimental

5.3.1 Synthesis of Ta_2O_5 nanotube arrays

Table 5.1 shows the as made Ta-oxy-N nanotube arrays prepared by varying: 1) electrolyte concentration; 2) anodization time (from 1 min to 1 h); 3) anodization voltage (from 20 to 60 V); 4) pre and post-treatment; 5) annealing time and temperature.

Anodization of Ta discs (35 mm diameter, 0.125 mm thickness, supplied by Sigma Aldrich) was performed in a two-electrode cell with the Ta disc as the anode and a Pt rod as the counter-electrode. Before the anodization, the samples were pre-treated with 400 grit abrasive paper and later sonicated in isopropyl alcohol for 30 min. The electrolyte was mainly composed of H_2SO_4 with different concentrations of HF and H_2O, except for a few samples that were prepared in ethylene glycol (EG) as the main component (see Table 5.1). The set voltage was reached by using an Agilent E3612A DC Power Supply, while the resulting current was saved by a Keithley 2000 Multimeter. After the anodization, the samples were sonicated in H_2O to remove the oxide and reused for a second anodization. In general, the growth of Ta_2O_5 nanotube arrays is faster than TiO_2, and 1-2 µm long nanotubes were obtained in few minutes (no more than 2 min). The experimental apparatus used for the anodization of Ta was the same of the system used for the preparation of TiO_2 nanotubes showed in Chapter 3 (paragraph 3.2).

5.3.2 Nitridation of Ta_2O_5 nanotube arrays

Tantalum oxide has a band gap higher than TiO_2 (about 4.4 eV for Ta_2O_5 vs. about 3.2 eV for TiO_2); this limits the absorbance of Ta oxide only in the UV light region. In order to shift the band gap of Ta_2O_5 to the visible region, it is necessary to convert Ta_2O_5 to Ta nitride (Ta_3N_5) or sub-nitride (TaOxNx), which have a band gap of about 1.9-2.5 eV (this value strongly depends on the grade of N substitution in the lattice). For that conversion, the as-anodized samples were annealed in a tubular quartz furnace under an ammonia flow. The set temperature (see table 5.1) was reached by a 25 C° min-1 ramp and then kept constant for the entire nitridation treatment. An inert gas was flown for 30 min to remove the oxygen from the tube and then 20 mL min-1 of ammonia flow was sent into the reactor. A tank containing 10 vol.% NH_3 in He was used as the ammonia source. The inert gas was used again for cooling the quartz tube.

SAMPLE	ANODIC OXDIDATION					ANNEALING
	V	RAMP	ELECTROLYTE	TIME	Ta THICKNESS	
TA1	15		HF/H2SO4 1:9 85%vol H2O	30 m	Ta 0.0025 mm	450°C / 3 h
TA2	15		HF/H2SO4 1:9 75%vol H2O	30 m	Ta 0.0025 mm	450°C / 3 h
TA3	20		HF/H2SO4 1:9 85%vol H2O	30 m	Ta 0.0025 mm	450°C / 3 h
TA4	10		HF/H2SO4 1:9 85%vol H2O	30 m	Ta 0.0025 mm	450°C / 3 h
TA5	15		HF/H2SO4 2:8 85%vol H2O	30 m	Ta 0.0025 mm	450°C / 3 h
TA6	25		EG/H2O 2:1 0,5% NH4F	60 m	Ta 0.0025 mm	450°C / 3 h
TA7	15		HF 0,4mL / H2SO4 11,6 mL / H2O 68 mL	30 m	Ta 0.0025 mm	450°C / 3 h
TA8	15		HF 0,4mL / H2SO4 11,6 mL / H2O 68 mL	30 m	Ta 0.0025 mm	450°C / 3 h
TA9	15		HF 0,4mL / H2SO4 11,6 mL / H2O 68 mL	20 m	Ta 0.0025 mm	450°C / 3 h
TA10	15		HF 0,8mL / H2SO4 11,6 mL / H2O 68 mL	20 m	Ta 0.0025 mm	450°C / 3 h
TA11	60		H2SO4 98% / 0,8%wt NH4F / 13,6% vol H2O	5 + 20m	Ta 0.0025 mm	450°C / 3 h
TA12	60		H2SO4 98% / 0,8%wt NH4F / 13,6% vol H2O	5 +20m	Ta 0.0025 mm	450°C / 3 h
TA13	60		H2SO4 98% / 1% vol HF / 4% vol H2O	20m	Ta 0.0025 mm	450°C / 3 h
TA14	60		H2SO4 98% / 1% vol HF / 4% vol H2O	5 + 15m	Ta 0.0025 mm	450°C / 3 h
TA15	60		H2SO4 98% / 1% vol HF / 4% vol H2O	5 + 15m	Ta 0.0025 mm	
TA16	60		H2SO4 98% / 1% vol HF / 4% vol H2O	5 + 15m	Ta 0.0025 mm	
TA17	60		H2SO4 98% / 1% vol HF / 4% vol H2O	5 + 15m	Ta 0.0025 mm	
TA18	60		H2SO4 98% / 1% vol HF / 4% vol H2O	5 + 15m	Ta 0.0025 mm	450°C / 3 h
TA19	60		H2SO4 98% / 1% vol HF / 4% vol H2O	10 + 10	Ta 0.0025 mm	
TA20	60		H2SO4 98% / 1% vol HF / 4% vol H2O	10 + 20	Ta 0.0025 mm	
TA21	60		H2SO4 98% / 1% vol HF / 4% vol H2O	20m	Ta 0.0025 mm	
TA22	60		H2SO4 98% / 1% vol HF / 4% vol H2O	20m	Ta 0.0025 mm	
TA23	60		H2SO4 98% / 1% vol HF / 4% vol H2O	10+10	Ta 0.0025 mm	
TA24	60		H2SO4 98% / 1% vol HF / 4% vol H2O	20m	Ta 0.0025 mm	
TA25	60		H2SO4 98% / 1% vol HF / 4% vol H2O	5+15	Ta 0.0025 mm	
TA26	60		H2SO4 98% / 1% vol HF / 4% vol H2O	10+15	Ta 0.0025 mm	450°C3h - 500°C3hNH3 - 700°C3hNH3
TA27	60		H2SO4 98% / 1% vol HF / 4% vol H2O	1+15	Ta 0.0025 mm	
TA28	60/40		H2SO4 98% / 1% vol HF / 4% vol H2O	10+15	Ta 0.0025 mm	700°C NH3 - 30m
TA29	60		H2SO4 98% / 1% vol HF / 4% vol H2O	10+15+5	Ta 0.0025 mm	
TA30	60		H2SO4 98% / 1% vol HF / 4% vol H2O	10+15	Ta 0.0025 mm	450°C3h - 600°C3hNH3
TA31	60		H2SO4 98% / 1% vol HF / 4% vol H2O	10+10	Ta 0.0025 mm	
TA32	60		H2SO4 98% / 1% vol HF / 4% vol H2O	10+10	Ta 0.0025 mm	500°C NH3
TA33	60		H2SO4 98% / 1% vol HF / 4% vol H2O	7+10	Ta 0.0025 mm	
TA34	60		H2SO4 98% / 1% vol HF / 4% vol H2O	7+5	Ta 0.0025 mm	
TA35	60		H2SO4 98% / 1% vol HF / 4% vol H2O	10+5	Ta 0.0025 mm	600°C / 700 °C NH3 3h
TA36	60		H2SO4 98% / 1% vol HF / 4% vol H2O	10+1	Ta 0.0025 mm	600°C / 700 °C NH3 3h
TA37	60/rampa		H2SO4 98% / 1% vol HF / 4% vol H2O	10+10	Ta 0.0025 mm	
TA38	10		H2SO4 98% / 1% vol HF / 4% vol H2O	10+30	Ta 0.0025 mm	650°C NH3 3h
TA39			EG / 1% NH4F / 4% vol H2O		Ta 0.0025 mm	
TA40			EG / 1% vol HF / 4% vol H2O		Ta 0.0025 mm	
TA41	60		H2SO4 98% / 1% vol HF / 4% vol H2O	10+5	Ta 0.0025 mm	700°C NH3 3h
TA42	20		H2SO4 98% / 1% vol HF / 4% vol H2O	10+40	Ta 0.0025 mm	
TA43	30		H2SO4 98% / 1% vol HF / 4% vol H2O	10+20	Ta 0.0025 mm	
TA44	20		H2SO4 98% / 1% vol HF / 4% vol H2O	10+40+15	Ta 0.0025 mm	
TA45	20		H2SO4 98% / 1% vol HF / 4% vol H2O	10+30+30	Ta 0.0025 mm	
TA46	20		H2SO4 98% / 1% vol HF / 4% vol H2O	30+	Ta 0.0025 mm	600°C air
TA47	20		H2SO4 98% / 1% vol HF / 4% vol H2O		Ta 0.0025 mm	
TA48	20		H2SO4 98% / 1% vol HF / 4% vol H2O	15+pochi m	Ta 0.0025 mm	450°C NH3 3h
TA49	20		H2SO4 98% / 1% vol HF / 4% vol H2O	15+20	Ta 0.0025 mm	
TA50	20		H2SO4 98% / 1% vol HF / 4% vol H2O	15+45	Ta 1mm	700°C 3h NH3
TA51	20		H2SO4 98% / 1% vol HF / 4% vol H2O	40	Ta 0.125 thick	700°C 3h NH3
TA52	30		H2SO4 98% / 1% vol HF / 4% vol H2O	20	Ta 0.125 thick	
TA53	60		H2SO4 98% / 1% vol HF / 4% vol H2O	10+10	Ta 0.125 thick	700°C 3h NH3
TA54	60/20		H2SO4 98% / 1% vol HF / 4% vol H2O	10+10	Ta 0.125 thick	
TA55	60/30		H2SO4 98% / 1% vol HF / 4% vol H2O	10+10	Ta 0.125 thick	
TA56	40		H2SO4 98% / 1% vol HF / 4% vol H2O	10+10	Ta 0.125 thick	
TA57	40		H2SO4 98% / 1% vol HF / 4% vol H2O	10+10	Ta 0.125 thick	700°C 3h NH3
TA58	40		H2SO4 98% / 1% vol HF / 4% vol H2O	10+10	Ta 0.125 thick	
TA59	40		H2SO4 98% / 1% vol HF / 4% vol H2O	10+10	Ta 0.125 thick	
TA60	40		H2SO4 98% / 1% vol HF / 4% vol H2O	10+10	Ta 0.125 thick	
TA61	40		H2SO4 98% / 1% vol HF / 4% vol H2O	10+10	Ta 0.125 thick	
TA62	40		H2SO4 98% / 1% vol HF / 4% vol H2O	10+1	Ta 0.125 thick	700°C 3h NH3
TA63	40		H2SO4 98% / 1% vol HF / 4% vol H2O	10+1	Ta 0.125 thick	700°C 3h NH3
TA64	40		H2SO4 98% / 1% vol HF / 4% vol H2O	10+1	Ta 0.125 thick	700°C 3h NH3
TA65	40		H2SO4 98% / 1% vol HF / 4% vol H2O	10+1	Ta 0.125 thick	700°C 3h NH3
TA66	40		H2SO4 98% / 1% vol HF / 4% vol H2O	10	Ta 0.125 thick	
TA67	40		H2SO4 98% / 1% vol HF / 4% vol H2O	10	Ta 0.125 thick	
TA68	40		H2SO4 98% / 1% vol HF / 4% vol H2O	10+1	Ta 0.125 thick	
TA69	40		H2SO4 98% / 1% vol HF / 4% vol H2O	10+1	Ta 0.125 thick	
TA70	40		H2SO4 98% / 1% vol HF / 4% vol H2O	10+1	Ta 0.125 thick	
TA71	40		H2SO4 98% / 1% vol HF / 4% vol H2O	10+1	Ta 0.125 thick	900°C 3h NH3
TA72	40		H2SO4 98% / 1% vol HF / 4% vol H2O	10+1	Ta 0.125 thick	800°C 3h NH3
TA73	40		H2SO4 98% / 1% vol HF / 4% vol H2O	10+1	Ta 0.125 thick	800°C 3h NH3
TA74	40		H2SO4 98% / 1% vol HF / 4% vol H2O	10+5	Ta 0.125 thick	800°C 3h NH3
TA75	40		H2SO4 98% / 1% vol HF / 4% vol H2O	10	Ta 0.125 thick	800°C 3h NH3
TA76	40		H2SO4 98% / 1% vol HF / 4% vol H2O	10+5	Ta 0.125 thick	800°C 3h NH3
TA77	40		H2SO4 98% / 1% vol HF / 4% vol H2O	10+5	Ta 0.125 thick	800°C 3h NH3
TA78	40		H2SO4 98% / 1% vol HF / 4% vol H2O	10+5	Ta 0.125 thick	450°C AIR
TA79	40		H2SO4 98% / 1% vol HF / 4% vol H2O	10+5	Ta 0.125 thick	800°C 3h NH3
TA80	40		H2SO4 98% / 1% vol HF / 4% vol H2O	10+6	Ta 0.125 thick	800°C 3h NH3

Table 5.1: Ta-oxy-N samples prepared at different voltage, time and with different electrolyte composition.

5.3.3 Characterization

UV-visible Diffuse Reflectance Spectroscopy measurements were performed by a Jasco V570 spectrometer equipped with an integrating sphere for solid samples, using $BaSO_4$ as the reference and in air. Scanning Electron Microscopy (Phenom ProX Desktop) was used for structural and morphological characterization of the TNT materials operated at an accelerating voltage of 5 kV. The nanotube diameter and length were directly measured by SEM images.

A homemade set-up (already described in paragraph 3.2 and shown in figure 3.2) was used for chrono-amperometry measurements. The device consists of a three-electrode photo-electrochemical cell, with a Pt wire as the counter-electrode and a 3M KCl-Ag/AgCl as the reference electrode. All the tests were performed at room temperature in 1 M Na_2SO_3 solution at 0.3 V using a 2049 AMEL potentiostat-galvanostat.

5.4 Results and discussion

5.4.1 Morphological study

Tantalum oxy-nitrides (Ta-oxy-N) nanotube arrays were synthesised by controlled anodic oxidation technique followed by ammonia treatment at high temperature, as described in the experimental section. The aim of preparing these kinds of electrodes derives from the issues evidenced by TiO_2 nanotube arrays, especially for what concerning the low response in visible light absorption.

The lower band gap of Ta-oxy-N seems very suitable to reduce/oxidize water and absorb light in the visible region. However, the use of Ta_2O_5 and its sub-nitrides gives some other issues, mainly related to their mechanical stability and photo-corrosion, as it will be described later. In this PhD work, many efforts have been made to overcome those limitations, through the optimization of the synthesis procedure acting on both the double step anodization and nitridation conditions.

First, the electrolyte mixing composition was investigated. Figure 5.1a shows a SEM image of Ta oxide prepared by one step of anodization in ethylene glycol with NH_4F as fluorine source and 4% vol. of H_2O (TA 39), while figure 5.1b shows a SEM image of a sample prepared with HF

as direct fluorine source (TA 40). In both the images, the presence of an irregular porous oxide structure (with pores ranging from 40 to 100 nm) can be observed and there is no evidence of a tubular structure. However, the sample prepared with HF has a more homogeneous surface.

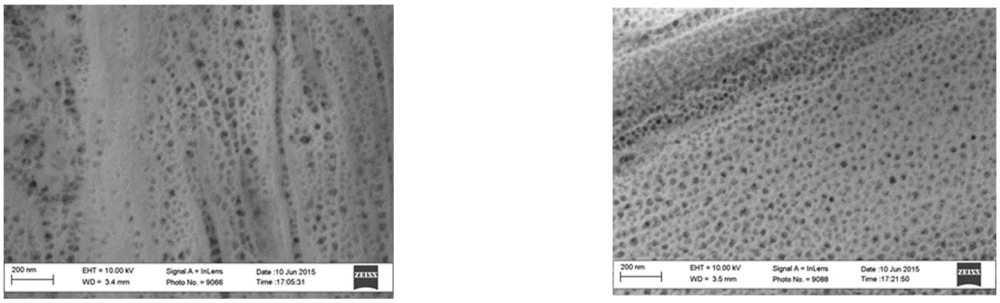

a b

Figure 5.1: SEM images of Ta oxide anodized in EG-based electrolyte, a) TA39 and b) TA 40.

Better results were obtained by using H_2SO_4 as the electrolyte, as shown in figure 5.2. Specifically, the SEM images refer to the sample prepared at 60 V for 10 min (figure 5.2a, b) (TA23) and 15 min (figure 5.2c,d) (TA25). The samples were rather inhomogeneous and their surface was not completely covered by Ta oxide nanopores (figure 5.2a), with some debris covering the tubes (figure 5.2c). The cross section image (reported in figure 2.5b) has confirmed the presence of a nano-tubular structure, but without the highly ordered arrays that usually characterize TiO_2 nanotubes. Particularly, the presence of nano-islands with flower-like tube organization can be observed in figure 5.2c. The 1-D vertical alignment at a nanoscale level is of fundamental importance to obtain a vectorial transport of electrons in the PEC cell, thus improving photo-catalytic performances.

After these preliminary experiments, the best conditions of synthesis in terms of electrolyte nature and concentration were set as follows: H_2SO_4 98% vol / HF 1% vol / H_2O 1% vol.

a ***b***

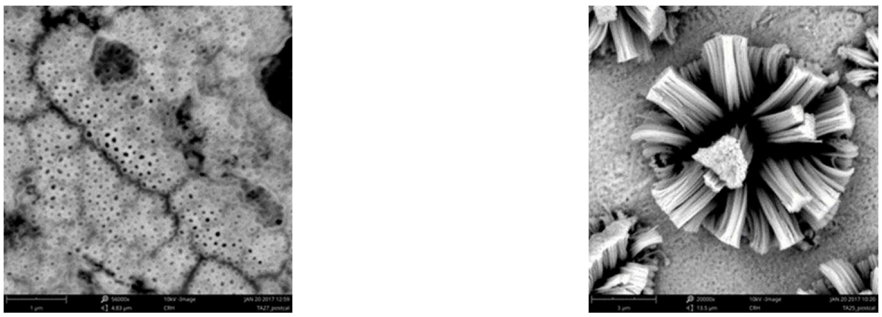

c ***d***

Figure 5.2: a) SEM image of Ta_2O_5 nanotubes, b) cross section image, c) high magnification of Ta_2O_5 nanotubes and d) flower-type island nanotubes.

In order to obtain a more robust and homogeneous photo-active layer, a double step of anodization was performed. After the first step of anodization, the nanostructured oxide layer was rinsed with deionized water and then removed by an ultrasonic treatment for 30 min in water. The remaining Ta substrate was then anodized shortly in a second step of anodization. The diagram in figure 5.3 shows a depiction of the Ta/Ta_2O_5 nanostructured electrode, with the support of SEM images showing the different steps of the nanotube formation. Specifically, figure 5.3a shows the top view of the Ta_2O_5 nanotube arrays, evidencing a homogeneous structure with a honeycomb aspect. Figure 5.3b shows the resulting oxide layer after the detachment of the membrane, revealing the template used for the second anodization step. Figure 3.5c shows the upside down view of the nanotube oxide membrane. Figure 3.5d shows the cross section image of the membrane, revealing the high 1-D nano-order needed for improving the electron transport.

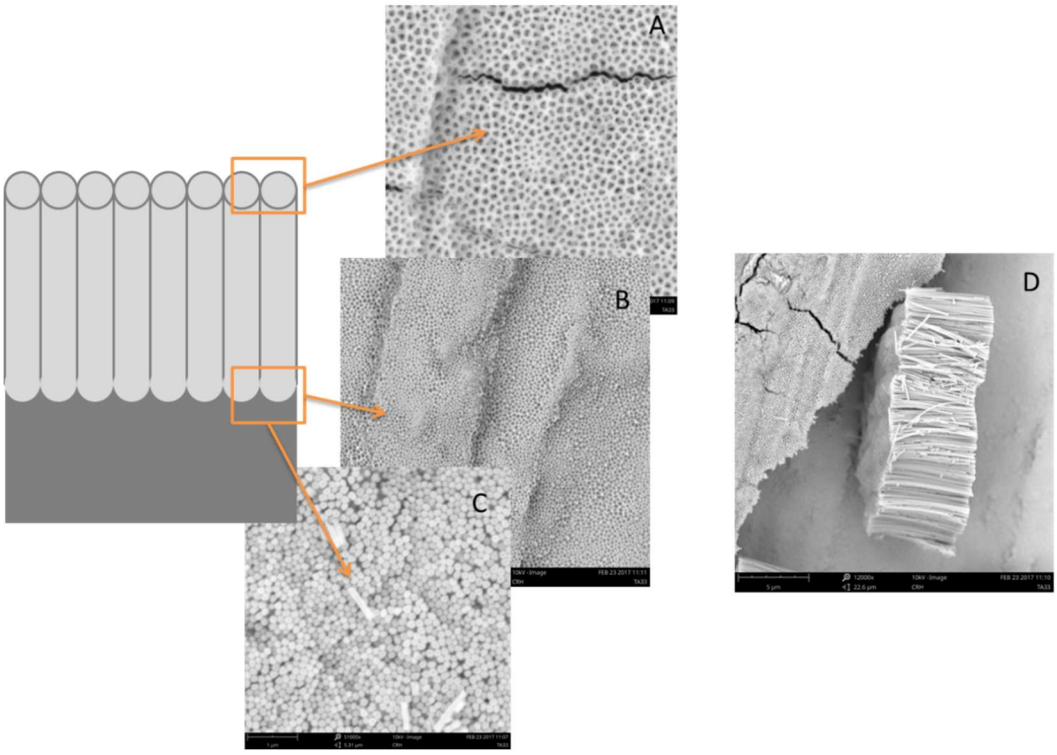

Figure 5.3: Schematic representation and SEM images of the different layers of Ta/Ta_2O_5 nanotube arrays. SEM images: a) top view, b) reaming template after sonication, c) upside down view of the membrane and d) cross section image.

Figure 5.4 shows the SEM images of Ta oxide nanotube arrays obtained by double-step anodization technique at 40 V (10 min each step) (TA56). The nanotube arrays appear quite compact and homogenous; the pores at the top surface are the opening of the nanotubes, while no interstitial spaces are present among the nanotubes.

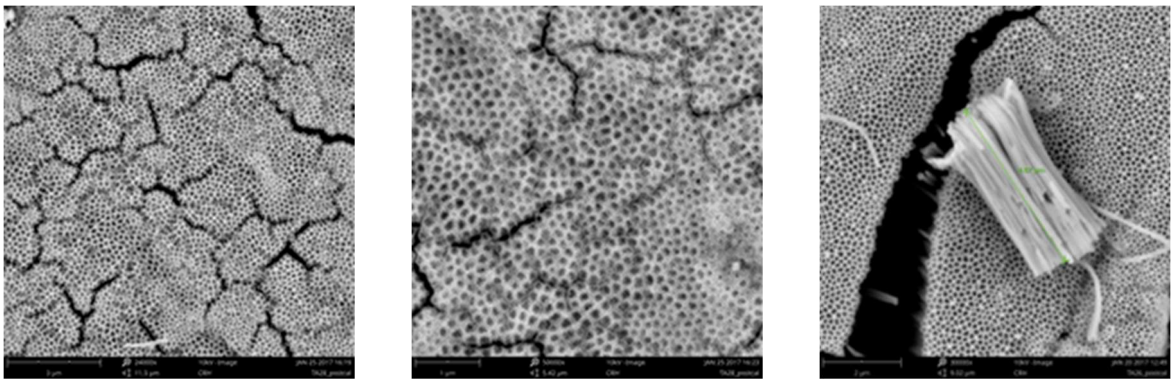

a ***b*** ***c***

Figure 5.4: SEM images of a) low magnification of Ta_2O_5 nantoubes, b) high magnification and c) cross section obtained from a detached piece of nanostructured Ta oxide.

In order to find a correlation between synthesis conditions and Ta oxide morphology/nano-architecture, the modulation of two parameters was investigated: i) anodization time (from 1 to 15 min) and ii) the applied potential (from 20 to 60 V). Figure 5.5a shows the profiles of tube length (green circles) and inner diameter (blue squares) versus the anodization time. As it can be observed, the higher the anodization time, the longer the nanotubes are (and the thicker the photo-catalytic layer is), while the tube diameter is quite constant. This trend is very similar with respect to TiO_2, even if the anodization times are quite shorter for Ta_2O_5 nanotube formation. Figure 5.5b, instead, shows the profile of the internal diameter of the tubes versus the applied potential for two cases: 1) blue triangles: first step set at 60 V; 2) red circles: the same voltage for both the steps. Results showed that the diameter of the nanotubes is mainly controlled by the first step of anodization.

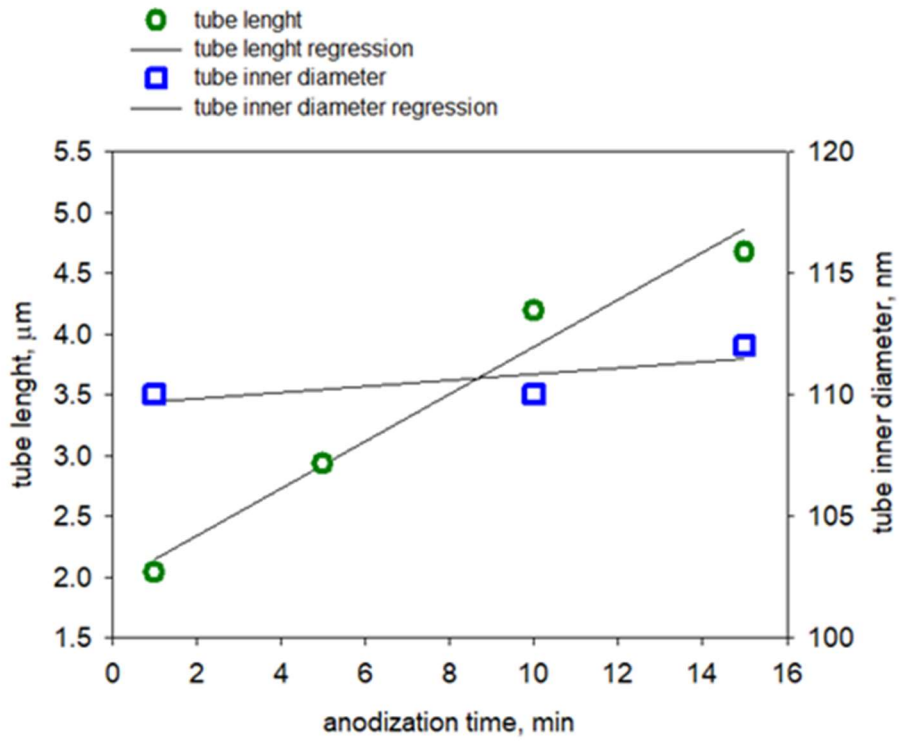

A

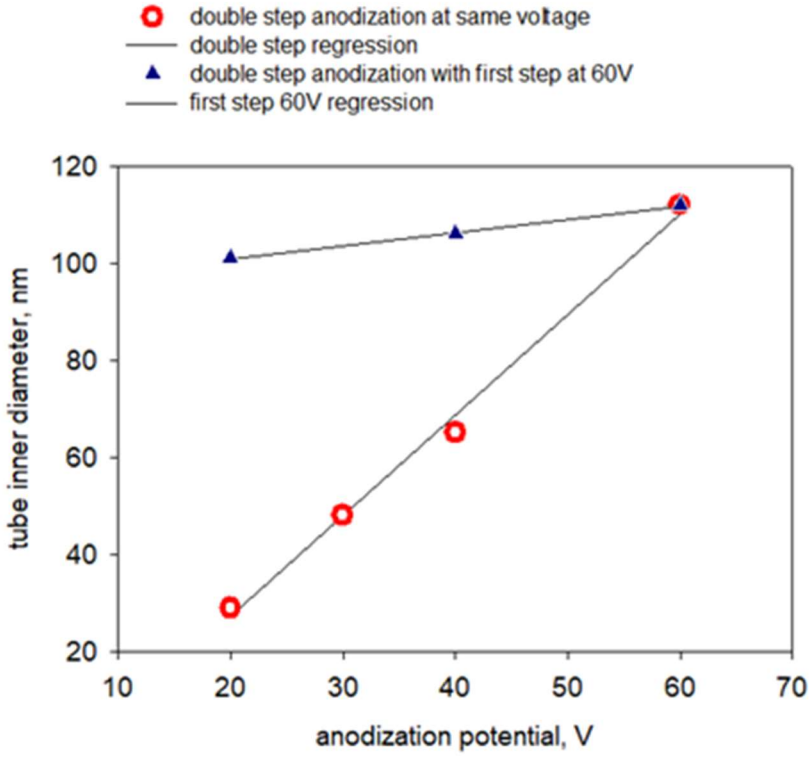

B

Figure 5.5: Relationship between voltage and time on tube morphology for a) single step anodization and b) double step anodization.

5.4.2 Influence of nitridation process

As discussed above, in order to convert the as-anodized Ta_2O_5 nanotubes to Ta-oxy-N, the layers were annealed at high temperature (ranging from 500 to 900°C) for different times (form 2 to 6 h) under ammonia flow. This high temperature post-treatment was needed to replace partially the O atoms with N in the Ta_2O_5 lattice. The decrease of the band gap should be directly proportional to the N loading. However, Ta-oxy-N nanotube arrays showed some mechanical issues, as they did not have a strong adhesion to the underlying Ta substrate and suffered from serious cracking and peeling-off of the nanotubes from the substrate. Figure 5.6 shows schematically what occurred after the nitridation process with the support of SEM images and EDX analysis. The Ta-oxy-N nanotubes, reported in orange, have a highly ordered tubular architecture, as expected, with about 28% of nitrogen provided by EDX analysis. Under the nanotubes, a further oxide layer can be observed (reported in yellow), with a partial

replacement of about 9% of nitrogen. Furthermore, another Ta oxide amorphous layer was detected (reported in dark green) over the metallic Ta remained non-oxidized, evidencing a nitrogen concentration of about 19%. This latter amorphous layer is responsible of the detachment of Ta-oxy-N nanotube membrane from the metallic Ta substrate.

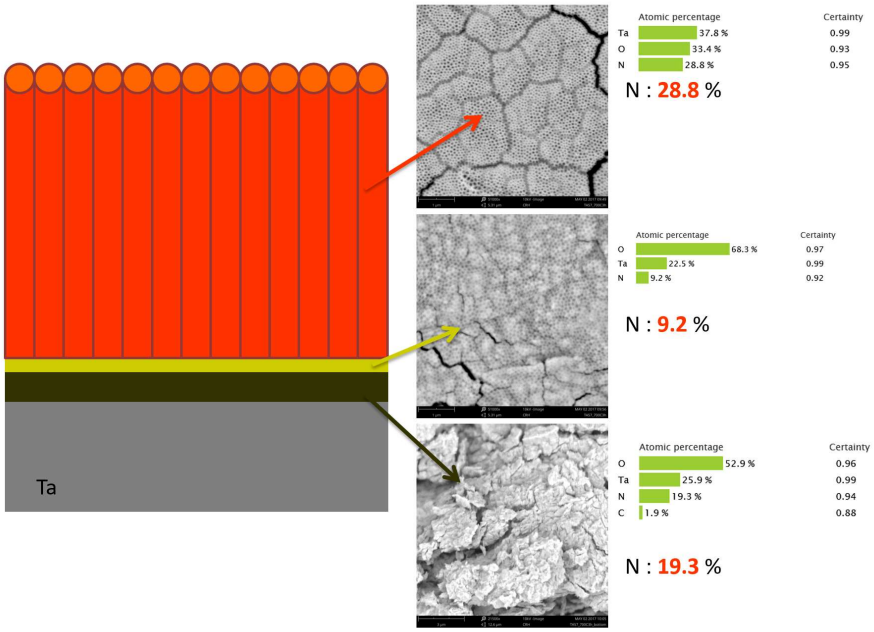

Figure 5.6: Schematic illustration of different layers of Ta-oxy-N electrodes after the nitridation process.

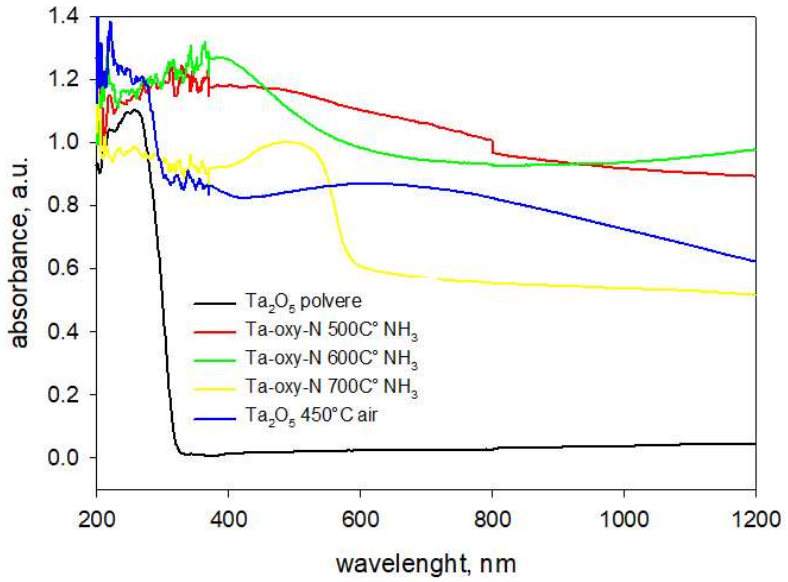

Figure 5.7: UV-visible spectra of Ta-oxy-N nanotube arrays treated at different nitridation temperature. Ta_2O_5 nanotubes and commercial Ta oxide powder are reported as reference.

Figure 5.7 shows the UV-visible spectra of the Ta-oxy-N nanotube arrays annealed in NH_3 at different temperatures. Commercial Ta_2O_5 and the Ta_2O_5 nanotubes (without N) are also reported as reference. In all the spectra, the characteristic high absorbance in the UV region of the bare Ta oxide can be observed. However, Ta-oxy-N nanotubes show a wide absorption in the visible region, with a well-defined peak for Ta-oxy-N samples annealed at 600 and 700°C (maximum at 390 and 540, respectively).

EDX results (reported in figure. 5.8) showed clearly that by increasing the temperature of nitridation the quantity of N increased: from 2.7% at 500°C to 15% at 800°C. Figure. 5.8 also shows the presence of S at 500°C, probably coming from the electrolyte bath, not present at higher temperatures.

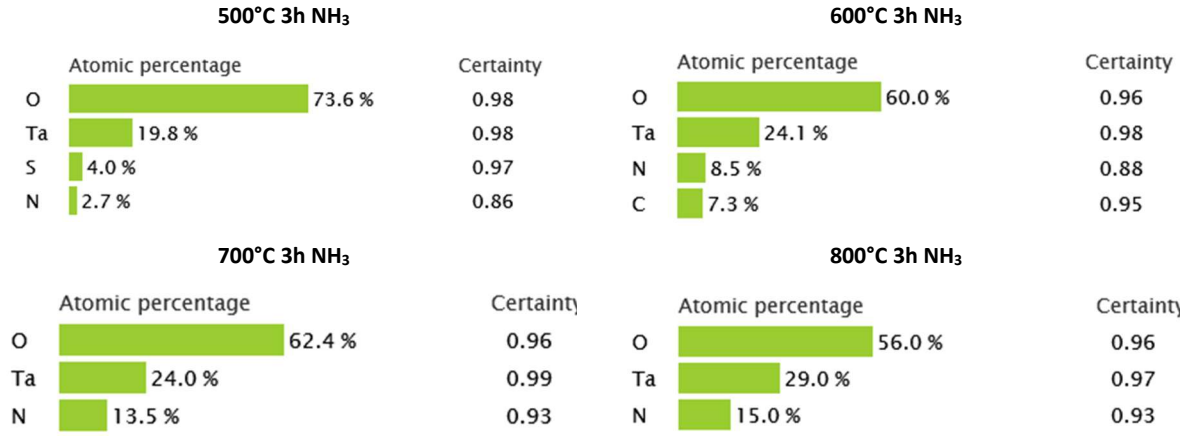

Figure 5.8: EDX atomic percentages for different temperatures of nitridation. Certainty refers to the probability of element identification (1.00 means absolute certainty)

5.4.3 Photo-electrochemical response

Figure 5.9 shows the photocurrent measurements under the application of the AM 1.5G filter, simulating the standard terrestrial solar distribution, for samples prepared at different applied voltages and nitridation temperatures. The sample anodized at 40 V (see figure 5.9a) provided the highest photocurrent response (with respect to the sample prepared at 20 and 60 V). It is to remark that the sample prepared at 40 V has a tube diameter of about 65-70 nm (see figure 5.5b) and a tube length less than 2 µm. This behaviour was similar to that already discussed in Chapter 3 for TiO_2 nanotubes about the length of the tubes. Figure 5.9b, instead,

shows the differences in photocurrent between two samples anodized at 40 V but treated with ammonia at different temperatures. As it can be observed, the nitridation temperature has a positive effect in terms of photocurrent; this is related to the higher substitution of N into the Ta_2O_5 lattice.

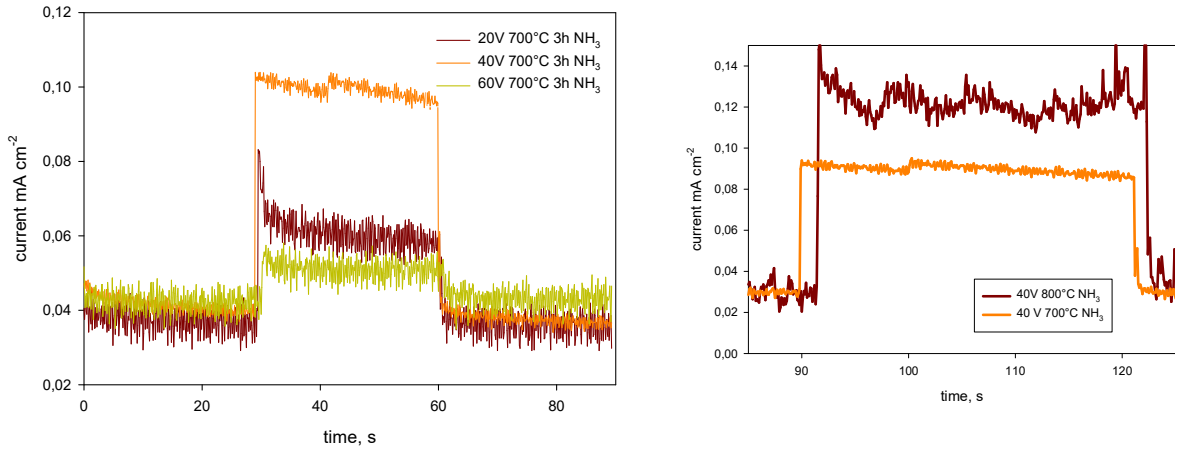

Figure 5.9: a) Photocurrent signals under AM 1.5G illumination of Ta-oxy-N nanotube arrays prepared at different voltages; b) photocurrent signals for 40 V anodized sample with different nitridation temperatures.

A photocatalytic test was conducted for the degradation of ethanol in gas phase (using the GP reactor, see Chapter 4, paragraph 4.3.3). Figure 5.10 shows the H_2 production rate (μmol min^{-1}) obtained for: i) commercial Ta_2O_5 powder (supplied by Sigma Aldrich -SA) annealed under ammonia flow at 900°C in 3 h, ii) Ta_2O_5 nanotube arrays (detached from Ta by strong sonication) and the commercial non-treated SA powder as reference. The results show the higher production of H_2 from Ta_2O_5 nanotubes in respect to the commercial SA powder, confirming the positive effects due to the presence of the nanostructure.

Ta_2O_5 (SA) treated with ammonia at 900°C provided the highest H_2 productivity, due to the higher absorbance in the visible region. Ta-oxy-nitrides cannot be tested due to their scarce robustness. However, these results are very promising and further studies are needed to improve the mechanical resistance of these Ta-oxy-N nanotube arrays to be used as efficient photoanodes for H_2 production in water photo-electrolysis.

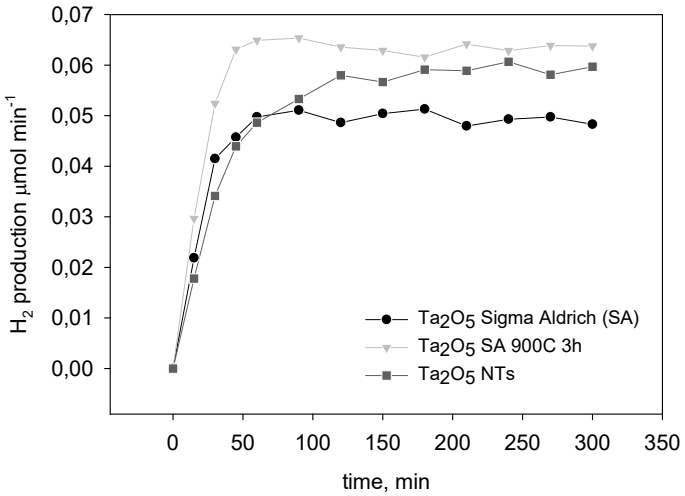

Figure 5.10: H_2 evolution during photoreforming experiments of Ta_2O_5 nanotubes and Sigma Aldrich (SA) powder as reference.

5.5 Conclusions

The synthesis of highly ordered Ta_2O_5 nanotube arrays through electrochemical anodization was performed. As in the case of TiO_2 nanotubes, the parameters of the anodization process influenced the morphology of the tantalum-based nanotube arrays and thus their electrochemical performances. Particularly in this chapter, the influence of voltage, anodization time and electrolyte concentration was investigated. A nitridation treatment at high temperature was necessary to convert Ta_2O_5 into Ta oxy-(sub)nitrides. The photo-electrochemical measurements showed:

- The sample anodized at 40 V provided the higher photocurrent response with respect to that anodized at 20 V and 60 V.
- Higher nitridation temperatures led to higher substitution of N into the Ta_2O_5 lattice, increasing from 2.7% for the sample treated at 500°C to about 15% for the sample prepared at 800°C.
- Increasing the temperature of nitridation (with the subsequent higher amount of N) results in an increase of the photocurrent response.

Further studies are needed to improve the Ta-oxy-N nanotube performances and stability but surely they represent a good candidate as photoanode to be used in PEC cells for water splitting reaction.

5.6 References

[1] C. Zhen, R. Chen, L. Wang, G. Liua, H.-M. Cheng, J. *Tantalum (oxy)nitride based photoanodes for solar-driven water oxidation* Mater. Chem. A, 4, 2783-2800 (2016)

[2] S. Naveenraj, G. J. Lee, S. Anandan, J. J. Wua, *Nanosized tantala based materials – synthesis and applications* Mat. Res. Bull. 67, 20–46 (2015)

[3] A.B. Murphy, P.R.F. Barnes, L.K. Randeniya, I.C. Plumb, I.E. Grey, M.D. Horne, J.A. Glasscock, *Efficiency of solar water splitting using semiconductor electrodes*, Int. J. Hydrogen Energy 31 1999–2017 (2006)

[4] J.Y. Duan, W.D. Shi, L.L. Xu, G.Y.Mou, Q.L. Xin, J.G. Guan, *Hierarchical nanostructures of fluorinated and naked Ta_2O_5 single crystalline nanorods: hydrothermal preparation, formation mechanism and photocatalytic activity for H_2 production*, Chem. Commun. 48 7301–7303 (2012)

[5] C. Zhen, L.Z. Wang, G. Liu, G.Q. Lu (Max), H.M. Cheng, *Template-free synthesis of Ta_3N_5 nanorod arrays for efficient photoelectrochemical water splitting*, Chem. Commun. 49, 3019–3021 (2013)

[6] F.Z. Tepehan, F.E. Ghodsi, N. Ozer, G.G. Tepehan, *Determination of optical properties of amorphous Ta_2O_5 films deposited by spin-and dip-coating methods*, Sol. Energy Mater. Sol. Cells 46 311–321 (1997)

[7] N. K. Allam, X. J. Feng, C. A. Grimes, *Self-Assembled Fabrication of Vertically Oriented Ta_2O_5 Nanotube Arrays, and Membranes Thereof, by One-Step Tantalum Anodization* Chem. Mater. 20, 6477–6481 (2008)

[8] H. A. El-Sayed, V. I. Birss, *Controlled Interconversion of Nanoarray of Ta Dimples and High Aspect Ratio Ta Oxide Nanotubes* Nano Lett., Vol. 9, No. 4, (2009)

[9] I. Sieber, B. Kannan, P. Schmuki, *Self-assembled porous tantalum oxide prepared in H_2SO_4/HF electrolytes*, Electrochem. Solid-State Lett. 8 J10–J12 (2005)

[10] H. A. El-Sayed V. I. Birss Controlled growth and monitoring of tantalum oxide nanostructures, Nanoscale, 2, 793–798 (2010)

[11] C.A. Horwood, H.A. El-Sayed, V.I. Birss *Precise electrochemical prediction of short tantalum oxidenanotube length*, Electroch. Acta 132 (2014)

[12] Z. Su, S. Grigorescu, L. Wang, K. Lee, P. Schmuki, *Fast fabrication of Ta_2O_5 nanotube arrays and their conversion to Ta_3N_5 for efficient solar driven water splitting* Electrochem. Comm. 50, 15–19 (2015)

[13] L. Wang, A. Mazare, I. Hwang, P. Schmuki *Tantalum nitride nanotube photoanodes: Establishing a beneficial back-contact by lift-off and transfer to titanium nitride layer* Electrochem. Comm. 72, 27–31 (2016)

[14] L. Wang, N. T. Nguyen, X. Zhou, I. Hwang, M. S. Killian, P. Schmuki *Enhanced Charge Transport in Tantalum Nitride Nanotube Photoanodes for Solar Water Splitting* ChemSusChem, 8,2615 –2620 (2015)

[15] S. Grigorescu, B. Bärhausen, L. Wang, A. Mazare, J. EunYoo, R. Hahn, P. Schmuki, *Tungsten doping of Ta_3N_5-nanotubes for band gap narrowing and enhanced photoelectrochemical water splitting efficiency,* Electrochem. Comm. 51, 85–88, (2015)

6 Conclusions

This PhD thesis focused on the development of nanostructured TiO_2-based photocatalysts for water photo-electrolysis.

Specifically, TiO_2 nanotube arrays were synthesised by anodic oxidation technique starting from metal titanium foils. An accurate control of the morphology/nanostructure of TiO_2 was made by modulating the parameters during the anodization, such as the electrolyte composition, the applied voltage and the anodization time. The anodization technique was perfectly suitable for the synthesis of thin catalytic films to be used as photo-anodes in advanced photo-electrochemical (PEC) cells, designed on purpose to improve performances in water photo-electrolysis. The presence of a controlled highly-ordered nanoarchitecture in TiO_2 allowed improving the vectorial transport of electrons, thus limiting charge recombination phenomena. In order to enhance light harvesting (especially in the visible region), metal (Au and Cu) nanoparticles were also deposited by different techniques on TiO_2 surface. The effects of these nanoparticles were widely investigated by different characterization techniques (SEM-EDX, TEM, XRD, UV-vis Diffuse Reflectance Spectroscopy, Cyclic Voltammetry, Chrono-amperometry) and by testing the modified TiO_2 electrodes for H_2 production in water photo-electrolysis, as well as in ethanol photo-reforming (simulating the processing of waste organic streams coming from biorefineries). Moreover, nanostructured tantalum oxynitride (Ta-oxy-N) electrodes were synthesized through controlled anodic oxidation, by adapting the operating conditions previously optimized for TiO_2, followed by ammonia treatment at high temperature to replace partially O with N atoms. The advantages of using these tantalum-based materials refer to their lower band-gap with respect to titania, thus improving light absorption in the visible region.

The general conclusion of the present PhD work was that, in order to develop a system able to convert efficiently solar energy into fuels/chemicals, two aspects should be taken into account: i) the synthesis of the photo-active materials, suitable to perform the reduction/oxidation reactions and ii) the engineering design of the cell and related electrodes, optimized to attain the maximum benefit from the irradiation pattern and minimize overpotential phenomena. However, the results have shown that these two aspects cannot be

tackled separately, but they are strictly connected each other as the same catalyst can provide large differences in terms of photocatalytic activity depending on the system used for testing.

Table 6.1 reports a summary of the most active samples prepared during the three years of PhD activity. The table reports the main conditions of synthesis (anodization time -AT, metal deposition technique -DP) and the structural parameters (nanotube length -TL and metal particle size -PS), as well as the performances of testing in water splitting (WS) and photo-reforming (i.e. ethanol dehydrogenation, ED), expressed as H_2 production rate (HP, μmol h^{-1}) and photoconversion efficiency (solar-to-hydrogen efficiency, STH).

Sample name	*AT, h*	*M*	*DP*	*TL, μm*	*PS, nm*	*R*	*TC*	*HP μmol h^{-1}*	*STH, %*	*SHT_{vis}, %*
TNT 45 m	0.75			1,0		WS	PEC	127.4	2.5	
TNT 1 h	1			1,3		WS	PEC	86.5	1.6	
TNT 1 h	1			1,3		ED	GP	9.1	1.6	
TNT 3 h	3			2,9		WS	PEC	68.7	1.1	
TNT 5 h	5			5,8		WS	PEC	51.1	0.7	0.23
TNT 5 h	5			5,8		ED	GP	25.2	0.7	0.23
TNT/Au WI	5	Au	WI	5,8	<100	ED	GP	16.8		
TNT/Au PD	5	Au	PD	5,8	8–15	ED	GP	32.3		
TNT/Au ED	5	Au	ELD	5,8	3–5	WS	PEC	9.6	0.4	0.11
TNT/Au ED	5	Au	ELD	5,8	3–5	ED	GP	39.7	0.4	0.11
TNT/Cu ED	1	Cu	ELD	1,3	~150					
TNT/Cu PF	1	Cu	SP	1,3	3-5	ED	GP	11.7		
TNT/Cu DC	1	Cu	DC	1,3	1-2	WS	PEC	104.3	2.0	0.53

Table 6.1: Summary of the most active tested TiO_2-based sample

TNT	Titania nanotube arrays	TL	Tube length
AT	Anodization time	PS	Metal particle size
M	Metal deposited on TNT	R	Reaction
DP	Metal deposition technique	WS	Water photo-electrolysis
WI	Wet-Impregnation	ED	Ethanol photo-reforming
PD	Photo-deposition	TC	Testing/reactor conditions
ELD	Electro-deposition	HP	Hydrogen production rate
SP	Spray coating	STH	Solar-to-hydrogen efficiency
DC	Dip-coating	STH_{vis}	Solar-to-hydrogen efficiency under AM1.5G

It can be observed that the photocatalytic performances were very different depending on testing conditions: i) a gas phase (GP) photo-reactor or ii) the PEC cell with separation of the two half-reactions.

In the GP system, the TiO_2-based photocatalyst was suspended inside the head space of the reactor in contact with the gas/vapour phase rich in ethanol, which partially condensed on the surface of TiO_2. By adopting this configuration, the more active samples were the substrates with higher amount of catalyst, corresponding to the TiO_2 nanotube arrays with longer nanotubes/higher thickness of the layer.

In GP-reactor tests, the presence of metal nanoparticles increased H_2 productivity, because: i) they increased the absorbance in the visible light region and ii) they acted as reduction centers for protons/electrons recombination. Particularly, the Au-doped TiO_2 nanotube arrays prepared by electrodeposition provided the highest H_2 production rate (14.4 % higher than the bare TiO_2 nanotube arrays). This result can be ascribed to the lower size of Au nanoparticles (about 3-5 nm) obtained by electrodeposition with respect to the bigger particles deposited by other techniques (e.g. by wet-impregnation). Copper nanoparticles had a positive effect on the production of hydrogen; particularly, Cu-TNT PF (pre-formed copper nanoparticles) sample provided a H_2 production rate 2.6% higher than the bare TiO_2 nanotubes having the same nanotube length.

In the PEC cell (with oxidation/reduction half reactions separated in two different chambers of the cell), the best performances were instead obtained with the 45-min-anodized TiO_2 nanotube arrays (tube length of about 1 μm), with a H_2 production of 127.4 μmol h^{-1} and a STH efficiency as high as 2.5%. These values are among the best ever reported insofar as undoped TiO_2 photoanodes are used and in absence of external bias or sacrificial agents.

In the PEC system, it was observed that the presence of metal nanoparticles on TiO_2 surface at the photo-anode can create a counter-circuited current, diminishing the H_2 production at the cathode side (and with the evolution of H_2 at the anode side). However, this phenomenon was successfully minimized especially for the case of copper, by preparing very small CuO nanoparticles (lower than 2 nm) decorating the internal walls of the TiO_2 nanotubes by controlled dip-coating technique.

Finally, the study on Ta-based photocatalysts allowed to obtain a clear correlation between the parameters using for the synthesis (i.e. applied voltage, anodization time) and the nanoarchitecture (nanotube diameter and length, wall thickness and grade of voids). The best photocurrent response was obtained for the Ta-oxy-N sample anodized at 40 V for 1 min and then thermally treated with ammonia at 800°C. However, further investigation is needed to improve the mechanical resistance of these photo-catalysts.

List of publications

Articles in journals (in ISI Web of Science/Scopus)

1. **Tavella, F.**, Ampelli, C., Leonardi, S.G., Neri, G. *Photo-electrochemical sensing of dopamine by a novel porous TiO_2 array-modified screen printed Ti electrode* Sensors, 18, 3566, pp. 1-11, (**2018**).
2. De Brito, J.F., **Tavella, F**., Genovese, C., Ampelli, C., Zanoni, M.V.B., Centi, G., Perathoner, S. *Role of CuO in the modification of the photocatalytic water splitting behavior of TiO_2 nanotube thin films* Applied Catalysis B: Environmental, 224, pp. 136-145 (**2018**)
3. Saboo, T., **Tavella, F**., Ampelli, C., Perathoner, S., Genovese, C., Marepally, B.C., Veyre, L., Quadrelli, E.A., Centi, G. *Water splitting on 3D-type meso/macro porous structured photoanodes based on Ti mesh* Solar Energy Materials and Solar Cells, 178, pp. 98-105 (**2018**)
4. **Tavella, F**., Ampelli, C., Frusteri, L., Frusteri, F., Perathoner, S., Centi, G. *Development of photoanodes for photoelectrocatalytic solar cells based on copper-based nanoparticles on titania thin films of vertically aligned nanotubes* Catalysis Today, 304, pp.190-198 (**2018**)
5. Marepally, B.C., Ampelli, C., Genovese, C., **Tavella, F**., Veyre, L., Quadrelli, E.A., Perathoner, S., Centi, G. *Role of small Cu nanoparticles in the behaviour of nanocarbon-based electrodes for the electrocatalytic reduction of CO_2* Journal of CO_2 Utilization, 21, pp. 534-542 (**2017**)
6. Ampelli, C., **Tavella, F**., Genovese, C., Perathoner, S., Favaro, M., Centi, G. *Analysis of the factors controlling performances of Au-modified TiO_2 nanotube array based photoanode in photo-electrocatalytic (PECa) cells* Journal of Energy Chemistry, 26 (2), pp. 284-294 (**2017**)
7. Ampelli, C., **Tavella,** F., Perathoner, S., Centi, G. *Engineering of photoanodes based on ordered TiO_2-nanotube arrays in solar photo-electrocatalytic (PECa) cells* Chemical Engineering Journal, 320, pp. 352-362 (**2017**)
8. Ampelli, C., Genovese, C., **Tavella, F**., Perathoner, S., Centi, G. *Nano-engineered electrodes for the generation of solar fuels: Benefits and drawbacks of adopting a photo-electrocatalytic (PECa) approach* Chemical Engineering Transactions, 57, pp. 1597-1602 (**2017**)
9. Ampelli, C., Genovese, C., **Tavella, F.**, Favaro, M., Agnoli, S., Granozzi, G., Perathoner, S., Centi, G. *Assembling of TiO_2 nanotube photoelectrodes with enhanced visible properties for a sustainable production of H_2* Chemical Engineering Transactions, 43, pp. 667-672 (**2015**)

Abstracts in national and international conferences

1. **F. Tavella**, C. Ampelli, C. Genovese, D. Giusi, S. Perathoner, G. Centi. Water Photo-Electrolysis onto Highly Ordered Nanotube Arrays Based on TiO_2 and Ta-oxy-N, XX Congresso Nazionale di Catalisi – XX Congresso Nazionale della Divisione di Chimica Industriale (GIC-DiChIn2018), *Book of abstracts*, O06PP, Milan (Italy), 2-5 September 2018
2. J. Ferreira de Brito, C. Genovese, **F. Tavella**, C. Ampelli, M.V. Boldrin Zanoni, G. Centi, S. Perathoner. High Faradaic selectivity in the CO_2 electrocatalytic reduction to formate over Cu_2O-Cu hybrid nanoparticles on gas-diffusion-layer electrode, The 8th Tokyo Conference on Advanced Catalytic Science and Technology (TOCAT8), *Book of abstracts*, ID307, Yokohama (Japan), 5-10 August 2018
3. D. Giusi, **F. Tavella**, C. Genovese, C. Ampelli, S. Perathoner, G. Centi, Photocatalytic reduction of CO_2 over Cu_2O nanocubes prepared via solvothermal and precipitation methods, EFCATS School on Catalysis, *Book of abstracts*, Liblice (Czech Republic), 25-29 June 2018
4. **F. Tavella**, C. Genovese, S. Chen, C. Ampelli, S. Perathoner, D. Su, G. Centi. Towards the activation of small molecules for the electrochemical production of solar fuels and ammonia: catalytic electrodes and cell design, 25th International Conference on Chemical Reaction Engineering – ISCRE 25 ("Engineering the Chemical Transformation by Bridging Science and Technology"), *Book of abstracts*, Af-We 10:30\1, Florence (Italy), 20-23 May 2018
5. S. Chen, H. Wei, C. Ampelli, C. Genovese, **F. Tavella**, D. Su, S. Perathoner, G. Centi. Electrochemical production of solar fuels and ammonia by using non-noble metal doped nanocarbons as electrocatalysts, 4th International Symposium on Chemistry for Energy Conversion and Storage (ChemEner2018), *Booklet of Abstracts*, P3, p. 53, Berlin (Germany), 28-31 January 2018
6. C. Ampelli, C. Genovese, **F. Tavella**, S. Perathoner, G. Centi. Nano-engineered electrodes based on TiO_2/Ti nanotubes and Cu doped carbon nanotubes for water photo-electrolysis and CO_2 conversion, 10th World Congress of Chemical Engineering (WCCE10) joint with the 11th European Congress of Chemical Engineering (ECCE11), *Abstracts*, OC-29556, Barcelona (Spain), 1-5 October 2017
7. **F. Tavella**, C. Ampelli, S. Perathoner, G. Centi. Tantalum oxynitride nanotube arrays as photoanode in photo-electrocatalytic (PECa) cells, 13th European Congress on Catalysis (EUROPACAT 2017), *Book of abstracts*, TS1.3.3, Florence (Italy), 27-31 August 2017
8. J. Ferreira de Brito, M.V. Boldrin Zanoni, **F. Tavella**, C. Genovese, C. Ampelli, S. Perathoner. Water Splitting and Simultaneous Photocatalytic CO_2 Reduction Using Coupling of $NtTiO_2$/CuO and GDL/Cu_2O Semiconductors Electrodes, IUPAC 49th General Assembly (IUPAC2017), *Proceedings*, 1151, São Paulo (Brazil), 7-13 July 2017
9. **F. Tavella**, C. Ampelli, L. Frusteri, F. Frusteri, S. Perathoner, G. Centi. Development of 2D-array on ordered oxide nanotubes as advanced electrodes and photocatalysts, 7th Czech-Italian-Spanish Symposium on Catalysis (CIS7), *Book of Abstracts*, Třešť (Czech Republic), 13-17 June 2017

10. N. Donato, S.G. Leonardi, C. Ampelli, **F. Tavella**, G. Neri. Photo-electrochemical sensing of dopamine by titania nanotubes array-electrodes fabricated by “in situ” modification of Ti screen printed electrodes, International Conference on Electrochemical Sensors (Mátrafüred 2017), *Book of Abstracts*, Mátrafüred (Hungary), 11-16 June 2017

11. T. Saboo, C. Ampelli, **F. Tavella**, B.C. Marepally, L, Veyre, C. Thieuleux, S. Perathoner, G. Centi, E.A. Quadrelli. Generation of solar hydrogen by water photo-oxidation on TiO_2 nanotubes/Ti gauze, 2ème Colloque “Solar Fuels” / Journée Nationale des Carburants Solaires, *Abstracts*, p. 63, Grenoble (France), 29 May-1 June 2017.

12. C. Ampelli, C. Genovese, **F. Tavella**, S. Perathoner, G. Centi. Nano-engineered electrodes for the generation of solar fuels: benefits and drawbacks of adopting a photo-electrocatalytic (PECa) approach, 13th International Conference on Chemical & Process Engineering (ICheaP-13), *Book of Abstracts*, Med-Mo 11:20\2, Milan (Italy), 28-31 May 2017

13. **F. Tavella**, C. Ampelli, S. Perathoner, G. Centi. Au/TiO_2-based nanostructured electrodes for the production of H_2 by water photo-electrolysis, XIX Congresso Nazionale di Catalisi (GIC 2016), *Book of abstracts*, O 8, p. 40, Bressanone (BZ, Italy), 11-14 September 2016

14. T. Saboo, C. Ampelli, **F. Tavella**, L, Veyre, S. Perathoner, G. Centi, E.A. Quadrelli. Generation of solar hydrogen by water photo-electrolysis on TiO_2 nanotubes/Ti gauze, Gordon Research Conference: Commercial Successes and Remaining Challenges after a Twenty Year Investment in Green Chemistry Principles, *Book of Abstracts*, Stowe (VT, United States), 31 July-5 August 2016.

15. C. Ampelli, C. Genovese, **F. Tavella**, S. Perathoner, G. Centi. Solar fuel production by reducing CO_2: prospects and open problems in the design of photo-electrocatalytic (PEC) cells and related nanostructured electrodes, 10° Encontro Nacional de Catálise e Materiais Porosos (X ENCMP), *Abstracts Book*, IL3, p. 7, ISBN: 978-989-8124-13-5, Lisbon (Portugal), 19-20 May 2016.

16. T. Saboo, C. Ampelli, **F. Tavella**, L, Veyre, S. Perathoner, G. Centi, E.A. Quadrelli. Titania nanotubes on microstructured Titanium for solar water splitting, French-Chinese Conference on Green Chemistry (FC2GChem), *Book of Abstracts*, Lyon (France), 9-13 May 2016.

Attendance in national and international conferences

1. **F. Tavella**, *Water Photo-Electrolysis onto Highly Ordered Nanotube Arrays Based on TiO_2 and Ta-oxy-N*, XX Congresso Nazionale di Catalisi XX Congresso Nazionale della Divisione di Chimica Industriale Milan, Italy, 2-5 september 2018 *ORAL PRESENTATION*
2. **F. Tavella**, *Development of 2d-array on ordered oxide nanotubes as advanced electrodes and photocatalysts*, 7th Czech-Italian-Spanish Symposium on Catalysis (CIS7), 13-17 June 2017, Trest (Czech Republic) *POSTER PRESENTATION*
3. **F. Tavella**, *Au/TiO_2-based nanostructured electrodes for the production of H_2 by water photo-electrolysis*, XIX CongressoNazionale di Catalisi (GIC 2016), Book of abstracts, O 8, p. 40, Bressanone (BZ, Italy), 11-14 September 2016 *ORAL PRESENTATION*